Abstract

This dissertation presents several novel robust tracking control schemes of rotorcraft unmanned aerial vehicles under realistic atmospheric turbulence.

To achieve fast converging and stable performance of the rotorcraft control scheme, a new Hölder-continuous differentiator, similar to the super-twisting algorithm used in the second-order sliding model control scheme, is proposed with guaranteed fast finite-time stability. Unlike the super-twisting algorithm, which uses a sliding-mode structure to achieve finite-time stability, the proposed differentiator maintains its fast finite-time stability with Hölder continuity, theoretically eliminating the harmful chattering phenomenon in practical control applications. Perturbation and noise robustness analyses are conducted for the proposed differentiator.

The dissertation formulates the rotorcraft tracking control and disturbance estimation problems separately. The rotorcraft aerial vehicle is modeled as a rigid body with control inputs that actuate all degrees of freedom of rotational motion and only one degree of freedom of translational motion. The motion of the aircraft is globally represented on $\mathrm{TSE}(3)$, which is the tangent bundle of the special Euclidean group $\mathrm{SE}(3)$. The translational and attitude control schemes track the desired position and attitude on $\mathrm{SE}(3)$. The disturbance estimation problem is formulated as an extended state observer on $\mathrm{TSE}(3)$.

Next, two rotorcraft control schemes on $\mathrm{SE}(3)$ with disturbance rejection mechanisms are presented. The proposed disturbance rejection control systems comprise two parts: an extended state observer for disturbance estimation and a tracking control scheme containing the disturbance rejection term to track the trajectory. The first disturbance rejection control scheme comprises an exponentially stable extended state observer and an asymptotically stable tracking control scheme.

The second system comprises a fast finite-time stable extended state observer and a fast finite-time stable tracking control scheme. The fast finite-time stable extended state observer uses the Hölder-continuous differentiator to estimate the resultant external disturbance force and disturbance torque acting on the vehicle. It ensures stable convergence of disturbance estimation errors in finite time when the disturbances are constant. Software-in-the-loop simulation is carried out for the active disturbance rejection control scheme with an open-source autopilot and a physics-based simulation tool. The simulation utilizes simulated wind gusts, propeller aerodynamics, actuator limitation, and measurement noise to validate the disturbance rejection control systems in a simulated environment with high fidelity.

Two sets of flight experiments are conducted to investigate the autonomous rotorcraft flight control performance under turbulent income flows. A wind tunnel composed of fan arrays is involved in both experiments to provide different turbulent incoming flows by adjusting the duty of individual fans. The first set of experiments conducts income flow measurements for wind tunnel calibration. For the turbulent flows generated by different fan configurations, their steady velocity field and unsteady turbulence characteristics are measured by a pressure scanner and hot-wire anemometer. The second set of experiments involves flight tests of a rotorcraft within the turbulent environment measured and calibrated in the first experiment set. The proposed extended state observer is implemented onto a rotorcraft by customizing an open-source autopilot software. With this implementation, the flight control performance of the proposed disturbance rejection control schemes is presented and compared with the autopilot without customization. The experimental results show that the proposed disturbance rejection control scheme enhanced by the disturbance estimation scheme.

Geometric Active Disturbance Rejection Control for Autonomous Rotorcraft in Complex Atmospheric Environment

by

Ningshan Wang

B.S., Shanghai Jiao Tong University, 2017

M.S., Syracuse University, 2019

Dissertation

Submitted in partial fulfillment of the requirements for the degree of

Doctor of Philosophy in Mechanical & Aerospace Engineering

Syracuse University

August 2023

To my family

Acknowledgements

Above all, I would like to thank my advisors, Dr. Amit K. Sanyal and Dr. Mark N. Glauser. Thank you for admiring my potential back in 2018 and for inspiring it over the past five years. Thank you for your endless support, guidance, and encouragement. I want to thank Dr. Sanyal for his precious time and efforts in teaching me to do technical writing professionally. I would also like to thank Dr. Glauser for his attempt to help me build the outdoor flow lab in 2020. It is a precious experience for a young man to get help from a senior professor to finish a heavy-duty hands-on job. At the end of my doctoral program, I want to let my advisors know I enjoy working with you every minute.

I am grateful to my defense committee members, Dr. Qinru Qiu, Dr. Victor H. Duenas, and Dr. Yiyang Sun. I used to learn and study with every single one of you. Thank you for your knowledge and mentorship during my time at Syracuse. Thank you for your help and advice in perfecting this dissertation.

I am also thankful to the fantastic fellows in Skytop Turbulence Lab during my doctoral study: Mr. Tyler Vartabedian, Dominic C. DiDominic III, Dr. Emma D. Gist, Mr. Seth Kelly, and Mr. Jean-Eric van der Elst. I would like to thank Mr. Peter LePorin, Mr. Aleksandar Dzodic, and Mr. Carl (Chip) W. Kjellberg. I appreciate your support with the hot-wire measurement and the fan-array wind tunnel. Moreover, thank you for your company and support during my hard time.

I would like to thank my Autonomous Unmanned Systems Lab friends: Dr. Sasi Prabhakaran, Dr. Reza Hamrah, and Mr. Abhijit Ulhas Dongare. Thank you for your company on my journey towards geometric mechanics and control.

I would like to thank my parents, Prof. Deyu Wang and Mrs. Hong Wei. Thank you for your endless, unconditional love and support during this period. I have been

away from my family for more than four years. As the single child of the family, I cannot have come so far without the deepest love and support from my family. I would also like to thank my partner, Jingxue, who has personally supported me through my most challenging times.

I would like to thank the funding support from the National Science Foundation award 2132799. I also thank Mr. Nicolas Bosson and Mr. Guillaume Catry from Wind-Shape *Corp.* for collaborating on this project. I would also like to thank Syracuse University for tuition support during much of my time as a graduate student.

Contents

List of Figures

List of Tables

List of Abbreviations

UAV	**U**nmanned **A**erial **V**ehicle
GNSS	**G**lobal **N**avigation **S**atellite **S**ystem
AHRS	**A**ttitude and **H**eading **R**eference **S**ystem
ANN	**A**rtificial **N**eural **N**etwork
AS	**A**symptotically **S**table
ES	**E**xponentially **S**table
FTS	**F**inite-**T**ime **S**table
FFTS	**F**ast **F**inite-**T**ime **S**table
PFTS	**P**ractical **F**inite-**T**ime **S**table
FxTS	**Fi**xite-**T**ime **S**table
ESO	**E**xtended **S**tates **O**bserver
LESO	**L**inear **E**xtended **S**tates **O**bserver
ES-ESO	**E**xponentially **S**table **E**xtended **S**tates **O**bserver
FFTS-ESO	**F**ast **F**inite-**T**ime **S**table **E**xtended **S**tates **O**bserver
RESO	**R**otational **E**xtended **S**tates **O**bserver
TESO	**T**ranslational **E**xtended **S**tates **O**bserver
DO	**D**isturbance **O**bserver
FxTSDO	**Fi**xite-**T**ime **S**table **D**isturbance **O**bserver
ADRC	**A**ctive **D**isturbance **R**ejection **C**ontrol

AS-ADRC	**A**symptotically **S**table **A**ctive **D**isturbance **R**ejection **C**ontrol
FFTS-ADRC	**F**ast **F**inite-**T**ime **S**table **A**ctive **D**isturbance **R**ejection **C**ontrol
INDI	**I**ncremental **N**onlinear **D**ynamics **I**nversion
MPC	**M**odel **P**redictive **C**ontrol
PID	**P**roportional-**I**ntegral-**D**erivative
SMC	**S**liding **M**ode **C**ontrol
SMO	**S**liding **M**ode **O**bserver
UIO	**U**nknown **I**nput **O**bserver
HCD	**H**ölder-**C**ontinuous **D**ifferentiator
HC-FTSD	**H**ölder-**C**ontinuous **F**inite-**T**ime **S**table **D**ifferentiator
HC-FFTSD	**H**ölder-**C**ontinuous **F**ast **F**inite-**T**ime **S**table **D**ifferentiator
SITL	**S**oftware-**I**n-**T**he-**L**oop
LGVI	**L**ie **G**roup **V**ariational **I**ntegrator
FAWT	**F**an **A**rray **W**ind **T**unnel
TI	**T**urbulence **I**ntensity
Re	**Re**ynolds Number
FFT	**F**ast **F**ourier **T**ransform
PSD	**P**ower **S**pectral **D**ensity
SE(3)	**3**-dimension **S**pecial **E**uclidean group
SO(3)	**3**-dimension **S**pecial **O**rthogonal group
TSO(3)	**T**angent bundle of **3**-dimension **S**pecial **O**rthogonal group
TSE(3)	**T**angent bundle of **3**-dimension **S**pecial **E**uclidean group

Chapter 1

Introduction

Small-scale rotorcraft unmanned aerial vehicles (UAVs) have become increasingly popular in a various applications, such as security and monitoring, infrastructure inspection, agriculture, wildland management, package delivery, and remote sensing. However, these UAVs are frequently exposed to dynamic uncertainties and disturbances caused by turbulence induced by airflow around structures or regions. For example, during the flight of a UAV over a wildfire, the vehicle experiences unsteady and turbulent airflow, variable air temperature, and air density, which harm its flight performance. Therefore, it is crucial to ensure robust flight control performance in such challenging environments, with guaranteed stability margins even in the presence of dynamic disturbances and uncertainties. To this end, this dissertation describes robust tracking control schemes for a rotorcraft UAV under disturbances and uncertainties.

Recent research articles on rotorcraft the UAV tracking control schemes use different methods to tackle the adverse effects from disturbances and uncertainties during the flight. (Torrente et al., 2021) use Gaussian processes to complement the nominal dynamics of the multi-rotor in a model predictive control (MPC) pipeline. (Hanover et al., 2021)

use an explicit scheme to discretize the dynamics for the nonlinear MPC solved by optimization. (Faessler, Franchi, and Scaramuzza, 2017) model the multi-rotor aerodynamic drag as a term depending on the attitude R and airspeed v and then utilize it in the tracking control schemes with properties on differential flatness. (Bangura and Mahony, 2017; Bangura et al., 2017) use the propeller aerodynamics as a direct feedforward term on the desired thrust to re-regulate the thrust command of the rotors. (Craig, Yeo, and Paley, 2020) implement a set of pitot tubes onto the multi-rotor aircraft to directly sense the aircraft's airspeed. With the knowledge of propeller aerodynamic characteristics, the airspeed is then utilized to obtain the disturbance forces and torques as feedforward terms to enhance control performance. (Bisheban and Lee, 2018, 2020) use artificial neural networks (ANN) to obtain disturbance forces and torques with the kinematics information of the aircraft and then use the baseline control scheme based on the work by (Lee, Leok, and McClamroch, 2010) in their tracking control scheme design. Among the fore-mentioned research articles, they either need high computation efforts (Bisheban and Lee, 2018, 2020; Hanover et al., 2021; Torrente et al., 2021), or have precise modeling on the aerodynamic characteristics of the rotorcraft propellers (Bangura and Mahony, 2017; Craig, Yeo, and Paley, 2020) to obtain satisfactory control performance against disturbances.

A promising control technique to maintain the control performance against disturbances and uncertainties is the active disturbance rejection control (ADRC), which can be traced back in (Hartlieb, 1956). In an ADRC scheme, one first obtains an estimation of the unknown disturbance from disturbance estimation and then utilizes it in the control design to reject such disturbance. ADRC and extended states observer (ESO) are formally introduced together by (Huang et al., 2001), which use ESO to obtain disturbance estimation and rejection. Other than ESO, disturbance observer (DO) (Chen, 2003), and

unknown input observer (UIO) (Basile and Marro, 1969) can also give disturbance estimation in a disturbance rejection control scheme.

ADRC schemes are widely used for rotorcraft UAV control. In the research articles by (Shao et al., 2018a,b), the disturbance estimation from asymptotically stable (AS) ESOs are employed to enhance surface trajectory tracking control scheme for a multi-rotor UAV in the presence of parametric uncertainties and external disturbances. (Liu et al., 2022) propose fixed-time stable (FxTS) disturbance observers and fault-tolerance mechanisms and utilize them in their translation and attitude control scheme. (Mechali et al., 2021) present FxTS ESOs for the same purpose. (Wang et al., 2019) implement incremental nonlinear dynamics inversion (INDI) control combing with sliding-mode observer (SMO) for disturbance estimation and rejection. (Jia et al., 2022a) employ the disturbance model obtained by (Faessler, Franchi, and Scaramuzza, 2017), and then estimate the drag coefficient as a parameter. This disturbance model is also employed by (Moeini, Lynch, and Zhao, 2021b). (Cui et al., 2021) use an adaptive super-twisting ESO for the disturbance estimation. (Bhale, Kumar, and Sanyal, 2022) give the disturbance estimation with the discrete-time FTS disturbance observer (Sanyal, 2022). Among the fore-mentioned research articles, experimental results are presented by (Mechali et al., 2021), (Jia et al., 2022a), and (Wang et al., 2019).

For the fore-mentioned ESO/DO designs used for rotorcraft tracking control, there are several methods to ensure their stability. The linear ESO by (Shao et al., 2018a,b) is asymptotically stable. (Mechali et al., 2021) use the geometric homogeneity (Levant, 2003; Rosier, 1992) to obtain FxTS ESO. A similar method is proposed in ESO design by (Guo and Zhao, 2011). The Lyapunov functions/candidates used in the ESO stability analysis by (Mechali et al., 2021) and (Guo and Zhao, 2011) are initially from (Rosier, 1992) and

are presented implicitly. (Jia et al., 2022a,b), (Moeini, Lynch, and Zhao, 2021b) and (Liu et al., 2022) use variants of the DO proposed in (Chen, 2003). Another method is to use the super-twisting algorithm (STA) (Moreno and Osorio, 2012) to obtain ESO design. (Xia et al., 2010) use this method in ESO design for spacecraft attitude control, and (Cui et al., 2021) design an adaptive super-twisting ESO using a similar method in a multi-rotor ADRC scheme.

In much of the prior literature for rotorcraft UAV attitude control with ESO/DOs for disturbance torque estimation and rejection in rotational dynamics, the attitude kinematics of the ESOs/DOs are either based on local linearization or represented using local coordinates (like Euler angles) or quaternions. Local coordinate representations can have singularity issues (e.g., gimbal lock with Euler angles), while quaternion representations may cause instability due to unwinding (Bhat and Bernstein, 2000a; Chaturvedi, Sanyal, and McClamroch, 2011). In situations where the UAVs have to carry out aggressive maneuvers, as in rapid collision avoidance for example, disturbance estimation and rejection from such schemes may not be reliable or accurate enough for precise control of the UAV.

To implement and validate the ESO/DO-based control scheme design for rotorcrafts, the external disturbance from atmospheric turbulence is usually difficult to generate in a lab environment. To generate repeatable gusts to imitate atmospheric turbulence, a common method is placing a box fan set with constant flow speed in the test section. This method is utilized by (Bangura and Mahony, 2017; Bisheban and Lee, 2018, 2020; Jeon et al., 2020; Jia et al., 2022a,b; Moeini, Lynch, and Zhao, 2021a; Wang et al., 2019). It is an efficient and valid setup. However, the windy area generated by a single box fan is too small for the flight of a real-sized multi-rotor to let it be exposed to constant excitation from turbulent incoming flows since the disturbance from turbulent incoming flows has

the strength to push the UAV away from the windy area. Moreover, with only one box fan as the wind source, the characteristics of the generated turbulent flows in the test section cannot be adjusted because of the limited input choice, which is the duty of the box fan. The experiment setup by (Craig, Yeo, and Paley, 2020) largely overcomes this problem. In (Craig, Yeo, and Paley, 2020), the wind is from a gust generation system consisting of eight Dyson fans behind remotely operated blinds. This gust generation system enlarges the windy test area compared with the gust/turbulence generated by a single box fan and enriches the input choice of the wind. For the same purpose, fan array wind tunnel (FAWT) is an optimal solution to generate such turbulent flows. The FAWT comprises arrays of individual fans that initialize velocity distributions discretely-individually or in-concert to produce appropriate mean and fluctuating velocities through an ample open-air test envelope that enables full-scale conventional statically-mounted aerodynamic-characterizations up through free-flight autonomous vehicle testing (Dougherty, 2022). The characteristics of the incoming flow from FAWT, especially the turbulence characteristics, are detailed by (Dougherty, 2022). Moreover, in prior research by (Olejnik et al., 2022a,b; O'Connell et al., 2022; Veismann et al., 2021; Wang et al., 2022), flight experiments of different kinds of autonomous aerial vehicles are conducted in the turbulent flows generated.

This dissertation presents two ADRC schemes enhanced by ESOs on $\mathrm{SE}(3)$ for rotorcraft UAVs under complex and challenging aerodynamic environments. The ESOs on $\mathrm{SE}(3)$ estimate the disturbance forces and torques during the flight of a rotorcraft UAV in both translation and rotation. The ADRC schemes on $\mathrm{SE}(3)$ then incorporate the disturbance estimation from the ESOs and the feedback from tracking control schemes to drive

the UAV to the desired trajectory. The first scheme is asymptotically stable active disturbance rejection control (AS-ADRC) scheme, with exponentially stable ESO (ES-ESO) for disturbance estimation and Asymptotically Stable (AS) tracking control, based on (Sanyal, Nordkvist, and Chyba, 2010). The second ADRC scheme is FFTS active disturbance rejection control (FFTS-ADRC), with fast finite-time stable ESO (FFTS-ESO) for disturbances estimation and FFTS tracking control scheme, based on the research article by (Viswanathan, Sanyal, and Samiei, 2018). The FFTS-ESO design is based on a novel Hölder-continuous fast finite-time stable differentiator (HC-FFTSD). We carried out several sets of numerical simulations to show the validity of the proposed ESO and ADRC designs. To evaluate the flight control performance of the proposed ADRC schemes, we implement the proposed ADRC schemes onto a real multi-rotor UAV for flight tests. In the flight test, we hover the UAV in front of the turbulent flows generated by a set of FAWT. We obtain the statistical and spectral information from pressure tube and hot-wire measurements on the turbulent incoming flows. We observe the translational and rotational motion of the UAV to evaluate its flight control performance using a motion capture system.

We highlight some unique contributions of this dissertation.

- The two proposed ESOs are the major contributions of this dissertation. In the proposed ESOs, which are the cores of the proposed ADRC schemes, the pose of the rotorcraft is represented directly on the Lie group of rigid body transformations, the special Euclidean group $\mathrm{SE}(3)$. Unlike the ESO and DO designs reported by (Mechali et al., 2021), (Shao et al., 2018b), and (Cui et al., 2021), which use Euler angles or quaternions for attitude representation or do not include attitude kinematics, like (Bhale, Kumar, and Sanyal, 2022) in disturbance torque estimation, the pose of

the aircraft in this dissertation is represented on $\mathrm{SE}(3)$ to avoid kinematic singularities. We do not use local coordinates (like Euler angles) or (dual) quaternions for pose representation so that we avoid singularities due to local coordinate representations or quaternion unwinding, as reported by (Bhat and Bernstein, 2000a; Chaturvedi, Sanyal, and McClamroch, 2011). To the best of the author's knowledge, there is no existing publication on aircraft ADRC using ESO with pose representation on $\mathrm{SE}(3)$.

- In the FFTS-ADRC scheme, the FFTS-ESO design is based on HC-FFTSD. The commonly used geometric homogeneity method by (Guo and Zhao, 2011; Levant, 2003), cannot provide a straightforward (or explicit) Lyapunov function to prove the finite-time stability of the scheme. The (implicit) form of their Lyapunov functions is by (Rosier, 1992). This implicit Lyapunov function complicates the robustness analysis under measurement noise and time-varying disturbances when that analysis is essential for an ESO designed for disturbance estimation in ADRC schemes. We propose HC-FFTSD as an approach inspired by the Super-Twisting Algorithm (STA) (Moreno and Osorio, 2012; Vidal, Nunes, and Hsu, 2016) of Sliding-Mode Control (SMC). This approach gives a straightforward design of a strict Lyapunov function, which is explicit, and therefore avoids the weakness mentioned above.

- Based on HC-FFTSD, the proposed FFTS-ESO schemes are both FFTS and Hölder-continuous, unlike the common STA and other FTS schemes that use discontinuous methods like terminal sliding-mode. Therefore, the proposed FFTS-ESO avoids the potentially harmful chattering phenomenon (Sanyal and Bohn, 2015), while maintaining FTS convergence.

- With explicit Lyapunov function in the stability analysis, we present the proof of robustness of the proposed FFTS-ESO under time-varying disturbing forces, torques, and measurement noise. To the best of the authors' knowledge, there is no prior research on the noise robustness of ESO using Lyapunov analysis.

- We use the FAWT to generate turbulent incoming flows and run the rotorcraft UAV flight test with the proposed ADRC within the flows. Compared with the flight experiment conducted by (O'Connell et al., 2022), we initialize different velocity distributions of the FAWT by changing the duty of individual fans. After that, we obtain the turbulent flows with different mean velocities and turbulence characteristics. The rotorcraft and its various flight control schemes, including the proposed ADRC scheme, are exposed to these turbulent flows so that we can comprehensively evaluate their performances under the disturbances from turbulent flows.

The remainder of this dissertation is structured as follows. Chapter 2 gives a detailed description of the Hölder-continuous differentiator. We present two HCD designs which are FTS and FFTS, respectively. The stability analysis of the proposed HC-FFTSD, is presented with its perturbation analysis and measurement noise robustness analysis. Chapter 3 formulates the tracking control problem, the ESO problem on $\mathrm{SE}(3)$, and gives the corresponding mathematical preliminaries. The tracking control scheme is based on the HCD described in Chapter 2. In Chapter 4 and Chapter 5, two ADRC schemes on $\mathrm{SE}(3)$ are presented. Chapter 4 presents the AS-ADRC scheme, which comprises ES-ESO and AS tracking control scheme on $\mathrm{SE}(3)$. Chapter 5 presents FFTS-ESO and FFTS-ADRC. The FFTS-ESO is based on the HC-FFTSD described in Chapter 2. The FFTS-ESO is compared with the DO and ESO from other publications on their disturbance estimation performance. Chapter 6 presents the simulated flight control performance of the proposed

ADRC schemes from software-in-the-loop (SITL) simulation with a physics engine and an open-source autopilot. Chapter 7 and 8 present experimental result. Chapter 7 presents the turbulence measurement from the FAWT in different working conditions. Chapter 8 describes the multi-rotor flight experiment under the turbulent incoming flows generated by the FAWT described in Chapter 7. Finally, Chapter 9 concludes the dissertation and outlines potential future directions.

Chapter 2

Hölder-Continuous Differentiator (HCD)

This chapter presents the HCD, which is among the major contributions of this dissertation. In Section 2.1, we reference and present some preliminaries for the stability proof and the robustness analysis of the proposed HCD. We present Hölder-continuous finite time stable differentiator (HC-FTSD) in Section 2.2 and Hölder- continuous fast finite time stable differentiator (HC-FFTSD) in Section 2.3, respectively. In Section 2.3, we analyze the stability and robustness of the proposed HC-FFTSD to support the development of ESO presented in Chapter 5. Theorem 2.3.1 gives the proposed HC-FFTSD with its stability properties. Corollary 2.3.1 describes the convergence performance of the differentiator under external disturbances. Corollary 2.3.2 describes the convergence performance of the differentiator under measurement noise. We present a brief summary for this chapter in Section 2.4. In the analysis that follows, $e_1 \in \mathbb{R}^n$ stands for the measurement estimation error and $e_2 \in \mathbb{R}^n$ stands for the disturbance estimation error in the ESO error dynamics, respectively. In this chapter and the remainder of this dissertation, we denote the minimum and maximum eigenvalues of a matrix by $\lambda_{\min}(\cdot)$ and $\lambda_{\max}(\cdot)$, respectively.

2.1 Preliminaries on stability

Consider the system of differential equations

$$\dot{x}(t) = f(x(t)), f(0) = 0, x(0) = x_0, \tag{2.1}$$

where $f : \mathcal{D} \to \mathbb{R}^n$ is continuous on an open neighbourhood $\mathcal{D} \subset \mathbb{R}^n$ of the origin.

Lemma 2.1.1 (Finite-time stable)**.** (Bhat and Bernstein, 2000b) *Let $V(x(t))$ be a continuous and differentiable function that is positive definite and satisfies the following inequality:*

$$\dot{V} \leq -\lambda V^{\alpha}, \tag{2.2}$$

with $x(t) \in \mathcal{D} \backslash \{0\}$, $\lambda > 0$, $\alpha \in]0, 1[$. Then the origin is finite-time stable (FTS), i.e., $\forall x_0 \in \mathcal{D}$, $x(t)$ converges to the origin in finite-time. The settling-time satisfies,

$$T \leq \frac{V^{1-\alpha}(x(0))}{\lambda(1-\alpha)} \tag{2.3}$$

Lemma 2.1.2 (Fast finite-time stable)**.** (Yu et al., 2005) *Consider the system* (2.1) *and let there exist a continuous and differentiable function $V(x(t))$, which is positive definite. With $V(x)$, fulfilling the following inequality,*

$$\dot{V} \leq -\lambda_1 V - \lambda_2 V^{\alpha}, \tag{2.4}$$

with $x(t) \in \mathcal{D}\backslash\{0\}$, $\lambda_1, \lambda_2 > 0$, $\alpha \in]0,1[$. *Then the origin is fast finite-time stable (FFTS). The settling time* T *satisfies*

$$T \leq \frac{1}{\lambda_1(1-\alpha)} \ln \frac{\lambda_1 V^{1-\alpha}(x(0)) + \lambda_2}{\lambda_2}. \tag{2.5}$$

Lemma 2.1.3 (Practical finite-time stable)**.** (Zhu, Xia, and Fu, 2011), (Yu, Shi, and Zhao, 2018) *Consider the system* (2.1) *and let there exist a continuous function* $V(x)$*, which is positive definite. With* $V(x(t))$*, fulfilling the following inequality,*

$$\dot{V} \leq -\lambda_1 V - \lambda_2 V^{\alpha} + \eta, \tag{2.6}$$

with $x(t) \in \mathcal{D}\backslash\{0\}$, $\lambda > 0$, $\alpha \in]0,1[$. *Then the origin is practical finite-time stable (PFTS), which means that the solution of* (2.1) *converges to the following set in finite time*

$$\left\{ x \middle| V(x) \leq \min \left\{ \frac{\eta}{(1-\theta_0)\lambda_1}, \left(\frac{\eta}{(1-\theta_0)\lambda_2} \right)^{\frac{1}{\alpha}} \right\} \right\}, \tag{2.7}$$

where $0 < \theta_0 < 1$. *The settling time is bounded as*

$$\begin{aligned} T \leq \max \Bigg\{ & t_0 + \frac{1}{\theta_0 \lambda_1 (1-\alpha)} \ln \frac{\theta_0 \lambda_1 V^{1-\alpha}(x(0)) + \lambda_2}{\lambda_2}, \\ & t_0 + \frac{1}{\lambda_1(1-\alpha)} \ln \frac{\lambda_1 V^{1-\alpha}(x(0)) + \theta_0 \lambda_2}{\theta_0 \lambda_2} \Bigg\}. \end{aligned} \tag{2.8}$$

Lemma 2.1.4. (Hardy et al., 1952)*Let* x *and* y *be non-negative real numbers and let* $p \in]1,2[$. *Then*

$$x^{\frac{1}{p}} + y^{\frac{1}{p}} \geq (x+y)^{\frac{1}{p}}. \tag{2.9}$$

Moreover, the above inequality is a strict inequality if both x and y are non-zero.

Definition 2.1.1. *Define $H : \mathbb{R}^3 \times \mathbb{R} \to \mathrm{Sym}(3)$, the space of symmetric 3×3 matrices, as follows:*

$$H(x,k) = I - \frac{2k}{x^{\mathrm{T}}x} x x^{\mathrm{T}}. \tag{2.10}$$

Lemma 2.1.5. *Define $\mu \in \mathbb{R}^n / \{0\}$, $\alpha \in]0, \frac{1}{2}[$. Consider $\mathcal{D} : \mathbb{R}^n \setminus \{0, -\mu\}$ and $\phi(x) : \mathcal{D} \to \mathbb{R}^+$*

$$\phi(x) = Y^{\mathrm{T}}Y = \left[\|x\|^{-2\alpha}x - \|x+\mu\|^{-2\alpha}(x+\mu)\right]^{\mathrm{T}} \left[\|x\|^{-2\alpha}x - \|x+\mu\|^{-2\alpha}(x+\mu)\right] \tag{2.11}$$

The global maximum of $\phi(x)$ is at $x = -\mu/2$.

2.2 Hölder-continuous finite-time stable differentiator (HC-FTSD)

Theorem 2.2.1 (HC-FTSD)**.** *Define $e_1, e_2 \in \mathbb{R}^n$ as the state variables. Consider the following differentiator design:*

$$\begin{aligned} \dot{e}_1 &= -k_1\phi_1(e_1) + e_2, \\ \dot{e}_2 &= -k_2\phi_2(e_1), \end{aligned} \tag{2.12}$$

where $p \in]1, 2[$, and $k_1, k_2 > 0$. Define $\phi_1(\cdot) : \mathbb{R}^n \to \mathbb{R}^n$ and $\phi_2(\cdot) : \mathbb{R}^n \to \mathbb{R}^n$ by:

$$\begin{aligned} \phi_1(e_1) &= (e_1^{\mathrm{T}}e_1)^{\frac{1-p}{3p-2}} e_1, \\ \phi_2(e_1) &= \frac{p}{3p-2}(e_1^{\mathrm{T}}e_1)^{\frac{2(1-p)}{3p-2}} e_1. \end{aligned} \tag{2.13}$$

Define $\mathcal{A}^* \in \mathbb{R}^{2\times 2}$ by:

$$\mathcal{A}^* = \begin{bmatrix} -k_1 & 1 \\ -k_2 & 0 \end{bmatrix}, \tag{2.14}$$

where k_1 and k_2 make $\mathcal{A}^*$ a Hurwitz matrix. (2.12) *ensures that the state $(e_1^{\mathrm{T}}, e_2^{\mathrm{T}})$ converges to the origin in an FTS manner.*

Proof. The proof of Theorem 2.3.1 is based on Theorem 1 by (Vidal, Nunes, and Hsu, 2016), and Theorem 1 by (Moreno and Osorio, 2012). Two properties of ϕ_1 and ϕ_2 are provided as follows.

Property 1 (P1): The Jacobian of $\phi_1(e_1)$, denoted $\phi_1'(e_1)$, is given as follows:

$$\phi_1'(e_1) = \frac{\mathrm{d}\phi_1(e_1)}{\mathrm{d}e_1} = (e_1^{\mathrm{T}} e_1)^{\frac{1-p}{3p-2}} \left[I - \frac{2(p-1)}{3p-2} \frac{e_1 e_1^{\mathrm{T}}}{e_1^{\mathrm{T}} e_1} \right], \tag{2.15}$$

so that the following identity holds:

$$\phi_2(e_1) = \phi_1'(e_1)\phi_1(e_1) \tag{2.16}$$

Property 2 (P2): ϕ_1' is a positive definite matrix, which means $\forall w \in \mathbb{R}^{2n}, e_1 \in \mathbb{R}^n$,

$$\lambda_{\min}\{\phi_1'(e_1)\}||w||^2 \leq w^{\mathrm{T}} \phi_1'(e_1) w \leq \lambda_{\max}\{\phi_1'(e_1)\}||w||^2. \tag{2.17}$$

The maximum and minimum eigenvalues of $\phi_1'(e_1)$ employed in (2.17) *are given by:*

$$\lambda_{\max}\{\phi_1'(e_1)\} = (e_1^{\mathrm{T}} e_1)^{\frac{1-p}{3p-2}}, \tag{2.18}$$

$$\lambda_{\min}\{\phi_1'(e_1)\} = (e_1^{\mathrm{T}} e_1)^{\frac{1-p}{3p-2}} \frac{p}{3p-2}. \tag{2.19}$$

From Theorem 5.5 by (Chen, 1984), we know that for a Hurwitz matrix $\mathcal{A}^*$ as defined by (2.14), $\forall\, \mathcal{Q}^* \in \mathbb{R}^{2\times 2}$ where $\mathcal{Q}^* \succ 0$, the Lyapunov equation

$$(\mathcal{A}^*)^{\mathrm{T}} \mathcal{P}^* + \mathcal{P}^* \mathcal{A}^* = -\mathcal{Q}^*, \tag{2.20}$$

has a unique solution $\mathcal{P}^* \succ 0$. We express the positive definite matrices $\mathcal{P}^*$ and $\mathcal{Q}^*$ in components as follows:

$$\mathcal{P}^* = \begin{bmatrix} p_{11} & p_{12} \\ p_{12} & p_{22} \end{bmatrix}, \ \mathcal{Q}^* = \begin{bmatrix} q_{11} & q_{12} \\ q_{12} & q_{22} \end{bmatrix}. \tag{2.21}$$

As $\mathcal{P}^*$ is the solution to (2.20), we augment $\mathcal{A}^*$, $\mathcal{P}^*$ and $\mathcal{Q}^*$ to $\mathcal{A}, \mathcal{P}, \mathcal{Q} \in \mathbb{R}^{2n\times 2n}$ as follows:

$$\mathcal{A} = \begin{bmatrix} -k_1 I & I \\ -k_2 I & 0 \end{bmatrix}, \mathcal{P} = \begin{bmatrix} p_{11} I & p_{12} I \\ p_{12} I & p_{22} I \end{bmatrix}, \mathcal{Q} = \begin{bmatrix} q_{11} I & q_{12} I \\ q_{12} I & q_{22} I \end{bmatrix}. \tag{2.22}$$

The augmented matrices $\mathcal{A}, \mathcal{P}, \mathcal{Q}$ defined above also satisfy the Lyapunov equation as given below:

$$\mathcal{A}^{\mathrm{T}} \mathcal{P} + \mathcal{P} \mathcal{A} = -\mathcal{Q}. \tag{2.23}$$

Further, the eigenvalues of $\mathcal{P}$ and $\mathcal{P}^*$ are related such that $\lambda_{\min}\{\mathcal{P}^*\} = \lambda_{\min}\{\mathcal{P}\}$, and $\lambda_{\max}\{\mathcal{P}^*\} = \lambda_{\max}\{\mathcal{P}\}$. Similar relations hold for $\mathcal{Q}$ and $\mathcal{Q}^*$. Therefore, as $\mathcal{P}$ is the solution to (2.23), we consider the following Lyapunov candidate:

$$V(e_1, e_2) = \zeta^{\mathrm{T}} \mathcal{P} \zeta, \tag{2.24}$$

where $\zeta \in \mathbb{R}^{2n}$ is defined as $\zeta := [\phi_1^{\mathrm{T}}(e_1), e_2^{\mathrm{T}}]^{\mathrm{T}}$ and $\mathcal{P}$ is the augmented $\mathcal{P}^*$, which is the unique solution of (2.20) for a given $\mathcal{Q}^* \succ 0$. The upper and lower bounds of the Lyapunov candidate V in (2.24) are given by:

$$\lambda_{\min}\{\mathcal{P}\} \|\zeta\|^2 \leq V(e_1, e_2) \leq \lambda_{\max}\{\mathcal{P}\} \|\zeta\|^2. \tag{2.25}$$

From (2.25), we obtain the following two inequalities:

$$\lambda_{\min}\{\mathcal{P}\} (e_1^{\mathrm{T}} e_1)^{\frac{p}{3p-2}} \leq \lambda_{\min}\{\mathcal{P}\} \|\zeta\|^2 \leq V(e_1, e_2), \tag{2.26}$$

$$k_3^2 \lambda_{\min}\{\mathcal{P}\} e_1^{\mathrm{T}} e_1 \leq \lambda_{\min}\{\mathcal{P}\} \|\zeta\|^2 \leq V(e_1, e_2). \tag{2.27}$$

$V(e_1, e_2)$ is differentiable everywhere except the subspace $\mathcal{S} = \{(e_1, e_2) \in \mathbb{R}^{2n} | e_1 = 0\}$. From (2.12) and Property (P1), we obtain the time derivative of ζ as follows:

$$\begin{aligned} \dot{\zeta} &= \begin{bmatrix} \phi_1'(e_1)\dot{e}_1 \\ \dot{e}_2 \end{bmatrix} = \begin{bmatrix} \phi_1'(e_1)(-k_1\phi_1(e_1) + e_2) \\ -k_2\phi_1'(e_1)\phi_1(e_1) \end{bmatrix} \\ &= \mathcal{D}(e_1)\mathcal{A}\zeta, \end{aligned} \tag{2.28}$$

where,

$$\begin{aligned}
&\mathcal{D}(e_1) = \mathrm{diag}[\phi_1'(e_1), \phi_1'(e_1)] \in \mathbb{R}^{2n\times 2n}, \\
&\lambda_{\min}\left\{\mathcal{D}(e_1)\right\} = \lambda_{\min}\left\{\phi_1'(e_1)\right\}.
\end{aligned} \tag{2.29}$$

Given the expression of $\dot{\zeta}$ in (2.28), we obtain the time derivative of $V(e_1, e_2)$ as follows:

$$\begin{aligned}
\dot{V} &= \dot{\zeta}^{\mathrm{T}}\mathcal{P}\zeta + \zeta^{\mathrm{T}}\mathcal{P}\dot{\zeta} \\
&= \zeta^{\mathrm{T}}((\mathcal{D}(e_1)\mathcal{A})^{\mathrm{T}}\mathcal{P} + \mathcal{P}\mathcal{D}(e_1)\mathcal{A})\zeta \\
&= -\zeta^{\mathrm{T}}\overline{\mathcal{Q}}(e_1)\zeta.
\end{aligned} \tag{2.30}$$

where $\overline{\mathcal{Q}}(e_1)$ is given by:

$$\begin{aligned}
&\overline{\mathcal{Q}}(e_1) = (\mathcal{D}(e_1)\mathcal{A})^{\mathrm{T}}\mathcal{P} + \mathcal{P}\mathcal{D}(e_1)\mathcal{A} = \begin{bmatrix} \overline{\mathcal{Q}}_{11}(e_1) & \overline{\mathcal{Q}}_{12}(e_1) \\ \overline{\mathcal{Q}}_{12}(e_1) & \overline{\mathcal{Q}}_{22}(e_1) \end{bmatrix}, \\
&\overline{\mathcal{Q}}_{11}(e_1) = 2(k_1 p_{11} + k_2 p_{12})\phi_1'(e_1), \\
&\overline{\mathcal{Q}}_{12}(e_1) = (k_1 p_{12} + k_2 p_{22} - p_{11})\phi_1'(e_1), \\
&\overline{\mathcal{Q}}_{22}(e_1) = -2p_{12}\phi_1'(e_1).
\end{aligned} \tag{2.31}$$

From (2.31) and (2.23), we obtain $\overline{\mathcal{Q}} = \mathcal{Q}\mathcal{D}(e_1)$. Thereafter, if $\mathcal{Q}$ and $\mathcal{D}(e_1)$ as defined in (2.23) and (2.29), respectively, are positive definite, then we obtain the following inequality on their eigenvalues

$$\lambda_{\min}\left\{\mathcal{Q}\mathcal{D}(e_1)\right\} \geq \lambda_{\min}\left\{\mathcal{Q}\right\}\lambda_{\min}\left\{\mathcal{D}(e_1)\right\} > 0. \tag{2.32}$$

After substituting (2.32) into (2.30) and applying Property 2, we obtain

$$\begin{aligned}\dot{V} &= -\zeta^{\mathrm{T}}(\mathcal{Q}\mathcal{D}(e_1))\zeta \\ &\leq -\lambda_{\min}\left\{\mathcal{Q}\mathcal{D}(e_1)\right\}\zeta^{\mathrm{T}}\zeta \\ &\leq -\lambda_{\min}\left\{\mathcal{D}(e_1)\right\}\lambda_{\min}\left\{\mathcal{Q}\right\}\zeta^{\mathrm{T}}\zeta.\end{aligned} \tag{2.33}$$

As $\lambda_{\min}\left\{\mathcal{D}(e_1)\right\} = \lambda_{\min}\left\{\phi_1'(e_1)\right\}$, substituting (2.19) and (2.26) into (2.33), we obtain

$$\begin{aligned}\dot{V} &\leq -(e_1^{\mathrm{T}}e_1)^{\frac{1-p}{3p-2}}\frac{p}{3p-2}\lambda_{\min}\left\{\mathcal{Q}\right\}\zeta^{\mathrm{T}}\zeta \\ &\leq -\frac{\lambda_{\min}\left\{\mathcal{Q}\right\}}{\lambda_{\max}\left\{\mathcal{P}\right\}}\left(\frac{V}{\lambda_{\min}\left\{\mathcal{P}\right\}}\right)^{\frac{1-p}{p}}\frac{p}{3p-2}V \\ &\leq -\gamma V^{\frac{1}{p}},\end{aligned} \tag{2.34}$$

where γ is a positive constant defined by:

$$\gamma = \frac{\lambda_{\min}\left\{\mathcal{Q}\right\}\lambda_{\min}\left\{\mathcal{P}\right\}^{\frac{p-1}{p}}}{\lambda_{\max}\left\{\mathcal{P}\right\}}\frac{p}{3p-2} = \frac{\lambda_{\min}\left\{\mathcal{Q}^*\right\}\lambda_{\min}\left\{\mathcal{P}^*\right\}^{\frac{p-1}{p}}}{\lambda_{\max}\left\{\mathcal{P}^*\right\}}\frac{p}{3p-2}. \tag{2.35}$$

Therefore, based on the inequality (2.34) and Lemma 2.1.1, we conclude that the origin of the error dynamics (2.12) is finite-time stable at the origin $(e_1 = 0, e_2 = 0)$. □

2.3 Hölder-continuous fast finite-time stable differentiator (HC-FFTSD)

Theorem 2.3.1 (HC-FFTSD)**.** Consider the following differentiator design:

$$\begin{aligned} \dot{e}_1 &= -k_1\phi_1(e_1) + e_2, \\ \dot{e}_2 &= -k_2\phi_2(e_1), \end{aligned} \tag{2.36}$$

where $p \in]1,2[$ and $k_1, k_2, k_3 > 0$. Define $\phi_1(\cdot) : \mathbb{R}^n \to \mathbb{R}^n$ and $\phi_2(\cdot) : \mathbb{R}^n \to \mathbb{R}^n$ by:

$$\begin{aligned} \phi_1(e_1) &= k_3 e_1 + (e_1^{\mathrm{T}} e_1)^{\frac{1-p}{3p-2}} e_1, \\ \phi_2(e_1) &= k_3^2 e_1 + \frac{2k_3(2p-1)}{3p-2}(e_1^{\mathrm{T}} e_1)^{\frac{1-p}{3p-2}} e_1 + \frac{p}{3p-2}(e_1^{\mathrm{T}} e_1)^{\frac{2(1-p)}{3p-2}} e_1. \end{aligned} \tag{2.37}$$

Define $\mathcal{A}^* \in \mathbb{R}^{2\times 2}$ by:

$$\mathcal{A}^* = \begin{bmatrix} -k_1 & 1 \\ -k_2 & 0 \end{bmatrix}, \tag{2.38}$$

where k_1 and k_2 make $\mathcal{A}^*$ a Hurwitz matrix. (2.36) ensures the state $(e_1^{\mathrm{T}}, e_2^{\mathrm{T}})$ converges to the origin in an FFTS manner.

Proof. The proof of Theorem 2.3.1 is similar to Theorem 2.2.1. We provide two properties on ϕ_1 and ϕ_2 in (2.37) as follows:

Property 1 (P1): The Jacobian of $\phi_1(e_1)$, denoted $\phi_1'(e_1)$, is given as follows:

$$\phi_1'(e_1) = \frac{\mathrm{d}\phi_1(e_1)}{\mathrm{d}e_1} = k_3 I + (e_1^{\mathrm{T}} e_1)^{\frac{1-p}{3p-2}} \left[I - \frac{2(p-1)}{3p-2} \frac{e_1 e_1^{\mathrm{T}}}{e_1^{\mathrm{T}} e_1} \right], \tag{2.39}$$

so that the following identity holds:

$$\phi_2(e_1) = \phi_1'(e_1)\phi_1(e_1). \tag{2.40}$$

Property 2 (P2): ϕ_1' is a positive definite matrix, which means $\forall w \in \mathbb{R}^{2n}, e_1 \in \mathbb{R}^n$,

$$0 < \lambda_{\min}\{\phi_1'(e_1)\}||w||^2 \leq w^{\mathrm{T}}\phi_1'(e_1)w \leq \lambda_{\max}\{\phi_1'(e_1)\}||w||^2. \tag{2.41}$$

The maximum and minimum eigenvalues of $\phi_1'(e_1)$ employed in (2.41) *are as given below:*

$$\lambda_{\max}\{\phi_1'(e_1)\} = k_3 + (e_1^{\mathrm{T}}e_1)^{\frac{1-p}{3p-2}}, \tag{2.42}$$

$$\lambda_{\min}\{\phi_1'(e_1)\} = k_3 + (e_1^{\mathrm{T}}e_1)^{\frac{1-p}{3p-2}}\frac{p}{3p-2}. \tag{2.43}$$

According to Theorem 5.5 in (Chen, 1984), for $\mathcal{A}^*$ in (2.38) as a Hurwitz matrix, $\forall \mathcal{Q}^* \in \mathbb{R}^{2\times 2}$, where $\mathcal{Q}^* \succ 0$, the Lyapunov equation,

$$(\mathcal{A}^*)^{\mathrm{T}}\mathcal{P}^* + \mathcal{P}^*\mathcal{A}^* = -\mathcal{Q}^*, \tag{2.44}$$

has the unique solution $\mathcal{P}^* \succ 0$. In (2.44), the positive definite matrices $\mathcal{P}^*$ and $\mathcal{Q}^*$ are in the same form as (2.21) in the proof of Theorem 2.2.1. Afterwards, with the $\mathcal{P}^*$ as the solution in (2.44), we augment $\mathcal{A}^*$, $\mathcal{P}^*$ and $\mathcal{Q}^*$ to $\mathcal{A}, \mathcal{P}, \mathcal{Q} \in \mathbb{R}^{2n\times 2n}$, like (2.23). The augmented matrices $\mathcal{A}, \mathcal{P}, \mathcal{Q}$ defined above also satisfy a Lyapunov equation as given below:

$$\mathcal{A}^{\mathrm{T}}\mathcal{P} + \mathcal{P}\mathcal{A} = -\mathcal{Q}. \tag{2.45}$$

Further, the eigenvalues of $\mathcal{P}$ and $\mathcal{P}^*$, are related such that $\lambda_{\min}\{\mathcal{P}^*\} = \lambda_{\min}\{\mathcal{P}\}$, and $\lambda_{\max}\{\mathcal{P}^*\} = \lambda_{\max}\{\mathcal{P}\}$. Similar relations hold for $\mathcal{Q}$ and $\mathcal{Q}^*$. Thus, with $\mathcal{P}$ as the solution to (2.45), we consider the following Lyapunov candidate:

$$V(e_1, e_2) = \zeta^{\mathrm{T}} \mathcal{P} \zeta, \tag{2.46}$$

where $\zeta \in \mathbb{R}^{2n}$ is defined as $\zeta := [\phi_1^{\mathrm{T}}(e_1), e_2^{\mathrm{T}}]^{\mathrm{T}}$ and $\mathcal{P}$ is the augmented $\mathcal{P}^*$, which is the unique solution of (2.45) for a given $\mathcal{Q}^* \succ 0$. The upper and lower bounds of the Lyapunov candidate V in (2.46) are as given below:

$$\lambda_{\min}\{\mathcal{P}\}\, \zeta^{\mathrm{T}} \zeta \leq V(e_1, e_2) \leq \lambda_{\max}\{\mathcal{P}\}\, \zeta^{\mathrm{T}} \zeta. \tag{2.47}$$

By applying (2.47), we obtain the following two inequalities:

$$\begin{gathered} \lambda_{\min}\{\mathcal{P}\}\, (e_1^{\mathrm{T}} e_1)^{\frac{p}{3p-2}} \leq \lambda_{\min}\{\mathcal{P}\}\, [\phi_1^{\mathrm{T}}(e_1)\phi_1(e_1) + e_2^{\mathrm{T}} e_2] \leq V(e_1, e_2) \\ V(e_1, e_2) \leq \lambda_{\max}\{\mathcal{P}\}\, [\phi_1^{\mathrm{T}}(e_1)\phi_1(e_1) + e_2^{\mathrm{T}} e_2], \end{gathered} \tag{2.48}$$

$$k_3^2 \lambda_{\min}\{\mathcal{P}\}\, e_1^{\mathrm{T}} e_1 \leq \lambda_{\min}\{\mathcal{P}\}\, [\phi_1^{\mathrm{T}}(e_1)\phi_1(e_1) + e_2^{\mathrm{T}} e_2] \leq V(e_1, e_2). \tag{2.49}$$

$V(e_1, e_2)$ is differentiable everywhere except the subspace $\mathcal{S} = \{(e_1, e_2) \in \mathbb{R}^{2n} | e_1 = 0\}$. By applying (2.36) and Property (P1), we obtain the time derivative of ζ as follows:

$$\begin{aligned} \dot{\zeta} &= \begin{bmatrix} \phi_1'(e_1)\dot{e}_1 \\ \dot{e}_2 \end{bmatrix} = \begin{bmatrix} \phi_1'(e_1)(-k_1\phi_1(e_1) + e_2) \\ -k_2\phi_1'(e_1)\phi_1(e_1) \end{bmatrix} \\ &= \mathcal{D}(e_1)\mathcal{A}\zeta, \end{aligned} \tag{2.50}$$

where,

$$\begin{aligned} &\mathcal{D}(e_1) \in \mathbb{R}^{2n}, \mathcal{D}(e_1) = \mathrm{diag}[\phi_1'(e_1), \phi_1'(e_1)], \\ &\lambda_{\min}\{\mathcal{D}(e_1)\} = \lambda_{\min}\{\phi_1'(e_1)\}. \end{aligned} \tag{2.51}$$

With the expression of $\dot{\zeta}$ in (2.50), we obtain the time derivative of $V(e_1, e_2)$ given by:

$$\dot{V} = -\zeta^{\mathrm{T}}\overline{\mathcal{Q}}(e_1)\zeta, \tag{2.52}$$

where $\overline{\mathcal{Q}}(e_1)$ is in the same form of (2.31) in the proof of Theorem 2.2.1.

Afterwards, we obtain $\overline{\mathcal{Q}} = \mathcal{Q}\mathcal{D}(e_1)$. With $\mathcal{Q}$, $\mathcal{D}(e_1) \succ 0$, as defined by (2.45) and (2.51), following inequality on their eigenvalues holds,

$$\lambda_{\min}\{\mathcal{Q}\mathcal{D}(e_1)\} \geq \lambda_{\min}\{\mathcal{Q}\}\lambda_{\min}\{\mathcal{D}(e_1)\} > 0. \tag{2.53}$$

By applying Property 2, substituting (2.53) into (2.52), we obtain

$$\begin{aligned} \dot{V} &= -\zeta^{\mathrm{T}}(\mathcal{Q}\mathcal{D}(e_1))\zeta \\ &\leq -\lambda_{\min}\{\mathcal{D}(e_1)\}\lambda_{\min}\{\mathcal{Q}\}\zeta^{\mathrm{T}}\zeta \end{aligned} \tag{2.54}$$

By applying $\lambda_{\min}\{\mathcal{D}(e_1)\} = \lambda_{\min}\{\phi_1'(e_1)\}$, substituting (2.43) and (2.48) into (2.54), we obtain

$$\begin{aligned}\dot{V} &\leq -\left[k_3 + (e_1^{\mathrm{T}} e_1)^{\frac{1-p}{3p-2}} \frac{p}{3p-2}\right] \lambda_{\min}\{\mathcal{Q}\} \zeta^{\mathrm{T}} \zeta \\ &\leq -\frac{\lambda_{\min}\{\mathcal{Q}\}}{\lambda_{\max}\{\mathcal{P}\}} \left[k_3 + \left(\frac{V}{\lambda_{\min}\{\mathcal{P}\}}\right)^{\frac{1-p}{p}} \frac{p}{3p-2}\right] V \\ &\leq -\gamma_1 V - \gamma_2 V^{\frac{1}{p}},\end{aligned} \tag{2.55}$$

where γ_1 and γ_2 are positive constants given by:

$$\begin{aligned}\gamma_1 &= k_3 \frac{\lambda_{\min}\{\mathcal{Q}\}}{\lambda_{\max}\{\mathcal{P}\}} = k_3 \frac{\lambda_{\min}\{\mathcal{Q}^*\}}{\lambda_{\max}\{\mathcal{P}^*\}}; \\ \gamma_2 &= \frac{\lambda_{\min}\{\mathcal{Q}\} \lambda_{\min}\{\mathcal{P}\}^{\frac{p-1}{p}}}{\lambda_{\max}\{\mathcal{P}\}} \frac{p}{3p-2} = \frac{\lambda_{\min}\{\mathcal{Q}^*\} \lambda_{\min}\{\mathcal{P}^*\}^{\frac{p-1}{p}}}{\lambda_{\max}\{\mathcal{P}^*\}} \frac{p}{3p-2}.\end{aligned} \tag{2.56}$$

Therefore, based on the inequality (2.55), Lemma 2.1.1 and Lemma 2.1.2, we conclude that the origin of the error dynamics (2.36) is FFTS. □

Corollary 2.3.1 (Disturbance/Perturbation robustness)**.** *Consider the proposed HC-FFTSD* (2.36) *in Theorem 2.3.1 under perturbation, Define* $\delta = (\delta_1^{\mathrm{T}}, \delta_2^{\mathrm{T}})^{\mathrm{T}}$, $\delta_1, \delta_2 \in \mathbb{R}^n$, *and* δ *is bounded as* $||\delta|| \leq \overline{\delta}$. *Thereafter, the differentiator under perturbation is given by:*

$$\begin{aligned}\dot{e}_1 &= -k_1 \phi_1(e_1) + e_2 + \delta_1, \\ \dot{e}_2 &= -k_2 \phi_2(e_1) + \delta_2.\end{aligned} \tag{2.57}$$

When γ_1 *in* (2.56) *satisfies* $\gamma_1 \geq \lambda_{\max}\{\mathcal{P}\}/\lambda_{\min}\{\mathcal{P}\}$, (2.57) *is PFTS.*

Proof. The proof of this corollary is based on the Lyapunov analysis in the proof of Theorem 2.3.1. With the Lyapunov candidate defined by (2.46) and expression of the differentiator under perturbation given by (2.57), we obtain the time derivative of (2.46) based on (2.55)

$$\dot{V} \leq -\gamma_1 V - \gamma_2 V^{\frac{1}{p}} + 2\lambda_{\max}\{\mathcal{P}\}\,\overline{\delta}||\zeta||, \tag{2.58}$$

By applying Cauchy-Schwarz inequality and substituting (2.47) to (2.58), we obtain

$$\begin{aligned} \dot{V} &\leq -\gamma_1 V - \gamma_2 V^{\frac{1}{p}} + \lambda_{\max}\{\mathcal{P}\}\,||\zeta||^2 + \lambda_{\max}\{\mathcal{P}\}\,\overline{\delta}^2 \\ &\leq -\left(\gamma_1 - \frac{\lambda_{\max}\{\mathcal{P}\}}{\lambda_{\min}\{\mathcal{P}\}}\right) V - \gamma_2 V^{\frac{1}{p}} + \lambda_{\max}\{\mathcal{P}\}\,\overline{\delta}^2. \end{aligned} \tag{2.59}$$

Therefore, from the inequality (2.59), we conclude that the origin of the error dynamics (2.57) is PFTS. □

Corollary 2.3.2 (Noise robustness)**.** *Consider the proposed HC-FFTSD* (2.36) *in Theorem 2.3.1 under measurement noise μ, so that $\phi_1(e_1)$ and $\phi_2(e_1)$ in* (2.37) *are replaced by $\phi_1(e_1+\mu)$ and $\phi_2(e_1+\mu)$ in the differentiator, as follows:*

$$\begin{aligned} \dot{e}_1 &= -k_1\phi_1(e_1+\mu) + e_2 \\ \dot{e}_2 &= -k_2\phi_2(e_1+\mu), \end{aligned} \tag{2.60}$$

where μ is bounded as $\|\mu\| \leq \overline{\mu}$. When γ_1 in (2.56) *satisfies $\gamma_1 \geq \lambda_{\max}\{\mathcal{P}\}/\lambda_{\min}\{\mathcal{P}\}$,* (2.60) *is PFTS.*

Proof. The proof of this corollary is based on the Lyapunov analysis in the proof of Theorem 2.3.1 and Corollary 2.3.1. We re-write (2.60) as follows:

$$\begin{aligned}
\dot{e}_1 &= -k_1\phi_1(e_1) + e_2 + k_1\phi_1^*(e_1,\mu), \phi_1^*(e_1,\mu) = -\phi_1(e_1+\mu) + \phi_1(e_1), \\
\dot{e}_2 &= -k_2\phi_2(e_1) + k_2\phi_2^*(e_1,\mu), \phi_2^*(e_1,\mu) = -\phi_2(e_1+\mu) + \phi_2(e_1).
\end{aligned} \tag{2.61}$$

By applying (2.37), we obtain,

$$\begin{aligned}
&\phi_1^*(e_1,\mu) = -\phi_1(e_1+\mu) + \phi_1(e_1) \\
&= -k_3\mu - \left[(e_1+\mu)^{\mathrm{T}}(e_1+\mu)\right]^{\frac{1-p}{3p-2}}(e_1+\mu) + (e_1^{\mathrm{T}}e_1)^{\frac{1-p}{3p-2}}e_1 \\
&\phi_2^*(e_1,\mu) = -\phi_2(e_1+\mu) + \phi_2(e_1) \\
&= -k_3^2\mu - \frac{2k_3(2p-1)}{3p-2}\left[(e_1+\mu)^{\mathrm{T}}(e_1+\mu)\right]^{\frac{1-p}{3p-2}}(e_1+\mu) + \frac{2k_3(2p-1)}{3p-2}(e_1^{\mathrm{T}}e_1)^{\frac{1-p}{3p-2}}e_1 \\
&- \frac{p}{3p-2}\left[(e_1+\mu)^{\mathrm{T}}(e_1+\mu)\right]^{\frac{2(1-p)}{3p-2}}(e_1+\mu) + \frac{p}{3p-2}(e_1^{\mathrm{T}}e_1)^{\frac{2(1-p)}{3p-2}}e_1.
\end{aligned}$$

Therefore, according to Lemma 2.1.5, the upper bounds of $\|\phi_1^*(e_1,\mu)\|$ and $\|\phi_2^*(e_1,\mu)\|$ are given by:

$$\begin{aligned}
&\|\phi_1^*(e_1,\mu)\| \le k_3\overline{\mu} + 2^{\frac{2(p-1)}{3p-2}}(\overline{\mu})^{1-\frac{2(p-1)}{3p-2}} \\
&\|\phi_2^*(e_1,\mu)\| \le k_3^2\overline{\mu} + \frac{2k_3(2p-1)}{3p-2}2^{\frac{2(p-1)}{3p-2}}(\overline{\mu})^{1-\frac{2(p-1)}{3p-2}} + \frac{p}{3p-2}2^{\frac{4(p-1)}{3p-2}}(\overline{\mu})^{1-\frac{4(p-1)}{3p-2}}
\end{aligned}$$

Thus, with the upper bounded $\|\phi_1^*(e_1,\mu)\|$ and $\|\phi_1^*(e_1,\mu)\|$, by applying Corallary 2.3.1, we conclude that the origin of the error dynamics (2.61) is PFTS. □

2.4 Summary

In this chapter, we present two HCD schemes with finite-time stability and fast finite-time stability, as HC-FTSD and HC-FFTSD, respectively. The FFTS-ESO presented in Chapter 5 is based on the HCD proposed in this chapter. The stability analysis of HCD is inspired by the strict Lyapunov function for the super-twisting algorithm by (Moreno and Osorio, 2012; Vidal, Nunes, and Hsu, 2016). We present the Lyapunov analyses of HC-FFTSD under perturbation and measurement noise, respectively.

Chapter 3

Problem Formulation

We formulate the extended state observer (ESO) and the disturbance rejection control problem on $\mathrm{SE}(3)$ with the corresponding mathematical preliminaries in this chapter. Section 3.1 describes the coordinate frame definition for the motion of the unmanned aerial vehicle (UAV) in this dissertation. Section 3.2 describes the system kinematics and dynamics. The preliminary on Morse function is covered in Section 3.3. We formulate the disturbance estimation problem within the ESO design, and define the ESO estimation error on $\mathrm{SE}(3)$ and its tangent space in Section 3.4. We pose the tracking control problem of the rotorcraft with the definition of tracking control error and the accordingly obtained tracking error kinematics and dynamics equation in Section 3.5. Afterwards, we formulate two active disturbance rejection control (ADRC) architectures on $\mathrm{SE}(3)$ in Section 3.5. We finalize this Chapter by a summary in Section 3.6.

3.1 Coordinate frame definition

We model a maneuverable autonomous rotorcraft UAV as a rigid body. We assume the geometric center of the UAV and the center of gravity are almost coincident. The configuration space is the special Euclidean group, which is the semi-direct product $\mathrm{SE}(3) =$

$\mathbb{R}^3 \rtimes \mathrm{SO}(3)$. We compactly represent the pose of the rigid body by

$$(b, R) \in \mathrm{SE}(3) \tag{3.1}$$

, where $b \in \mathbb{R}^3$ denotes the position vector in inertial coordinate frame $\mathcal{E}$ and $R \in \mathrm{SO}(3)$ denotes the rotation matrix from body-fixed coordinate frame $\mathcal{B}$ to frame $\mathcal{E}$. We define $\mathbf{e}_1 = [1, 0, 0]^{\mathrm{T}}$, $\mathbf{e}_2 = [0, 1, 0]^{\mathrm{T}}$, and $\mathbf{e}_3 = [0, 0, 1]^{\mathrm{T}}$. In Figure 3.1, we present the inertial frame and a body-fixed frame, which are spanned by unit vectors $\{\mathbf{e}_1, \mathbf{e}_2, \mathbf{e}_3\}$ and $\{\mathbf{b}_1, \mathbf{b}_2, \mathbf{b}_3\}$ in north-east-down (NED) directions, respectively.

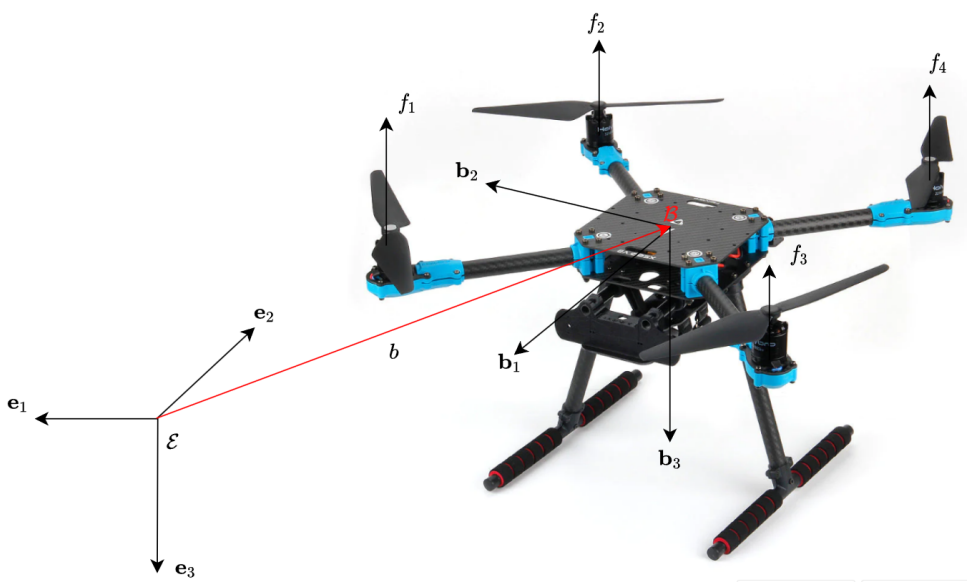

FIGURE 3.1: The UAV and coordinate frames

In Figure 3.1, we observe that the the actuations f_1 to f_4 are perpendicular to the $b_1 - b_2$ plane of $\mathcal{B}$. The control inputs actuate all degrees of freedom of rotational motion but only one degree of freedom of translational motion.

3.2 System kinematics and dynamics

With the pose of the UAV defined in Section 3.1, the kinematic equations for the UAV are then given by:

$$\dot{b} = v, \dot{R} = R\Omega^{\times}, \tag{3.2}$$

where $v \in \mathbb{R}^3$ denotes the translational velocity in frame $\mathcal{E}$, and $\Omega \in \mathbb{R}^3$ denotes the angular velocity in body-fixed frame $\mathcal{B}$. $(\cdot)^{\times} : \mathbb{R}^3 \to \mathfrak{so}(3) \subset \mathbb{R}^{3\times 3}$ is the skew-symmetric cross-product operator defined by:

$$x^{\times} = \begin{bmatrix} x1 \\ x2 \\ x3 \end{bmatrix}^{\times} = \begin{bmatrix} 0 & -x_3 & x_2 \\ x_3 & 0 & -x_1 \\ -x_2 & x_1 & 0 \end{bmatrix}. \tag{3.3}$$

The overall system kinematics and dynamics of a rotorcraft with a body-fixed plane of rotors are given by:

$$\begin{aligned} &\dot{b} = v \\ &m\dot{v} = mg\mathbf{e}_3 - fR\mathbf{e}_3 + \varphi_D, \\ &\dot{R} = R\Omega^{\times}, \\ &J\dot{\Omega} = J\Omega \times \Omega + \tau + \tau_D, \end{aligned} \tag{3.4}$$

where $f \in \mathbb{R}$ is the scalar thrust force, and $\tau \in \mathbb{R}^3$ is the control torque created by the rotors. g denotes the acceleration due to gravity, and $m \in \mathbb{R}^+$, $J = J^{\mathrm{T}} \in \mathbb{R}^{3\times 3}$ denote the mass and inertia matrix of the UAV, respectively. φ_D denotes the force disturbances in

frame $\mathcal{E}$. τ_D denotes the torque disturbances in frame $\mathcal{B}$. These disturbances are mainly due to unsteady aerodynamics.

The measurements of a typical multi-rotor UAV are from the real-time kinematic global navigation satellite system (RTK-GNSS), and inertial navigation system (INS). The INS gives the attitude and angular velocity measurements, denoted as R^m and Ω^m, respectively. The RTK-GNSS gives the position and translational velocity measurements, denoted as b^m and v^m, respectively. With the presence of measurement uncertainties, these measurements are modeled as:

$$b^m = b + \nu_b, v^m = v + \nu_v, R^m = R\exp(\nu_R^\times), \Omega^m = \Omega + \nu_\Omega, \tag{3.5}$$

where $\nu_b, \nu_v, \nu_R, \nu_\Omega \in \mathbb{R}^3$ are uncertain terms of position, velocity, attitude, and angular velocity measurements. In the numerical simulations covered in Chapters 4 and 5, a realistic RTK-GNSS/INS model is provided with quantified measurement uncertainties.

3.3 Morse function on $\mathrm{SO}(3)$

As described in Section 3.1, the attitude of the UAV is represented on the configuration space $\mathrm{SO}(3)$, which is non-trivial. Unlike the mechanical system represented by generalized coordinates in $\mathbb{R}^n$, $\mathrm{SO}(3)$ is a non-contractible manifold. With the presence of multiple equilibria existing for continuous autonomous systems evolving on non-contractible manifolds, the tracking control schemes need to ensure that only the desired attitude is tracked (Bohn and Sanyal, 2016). Similarly, the ESO need to ensure that only the real attitude of the UAV is estimated. To this end, we introduce the Morse function as part of the

Lyapunov function in the stability analysis of rotational ESO and attitude tracking control scheme.

Lemma 3.3.1. (Bohn and Sanyal, 2016), (Bullo and Lewis, 2019) *Consider attitude kinematics*

$$\dot{R} = R\Omega^{\times}, R \in \mathrm{SO}(3), \Omega^{\times} \in \mathfrak{so}(3). \tag{3.6}$$

Let $K = \mathrm{diag}(K_1, K_2, K_3)$*, where* $K_1 > K_2 > K_3 \geq 1$*. Define*

$$s_K(R) = \sum_{i=1}^{3} K_i (R^{\mathrm{T}} \mathbf{e}_i) \times \mathbf{e}_i, \tag{3.7}$$

such that $\frac{\mathrm{d}}{\mathrm{d}t}\langle K, I - R\rangle = \Omega^{\mathrm{T}} s_K(R)$*. Here* $\langle A, B\rangle = \mathrm{tr}(A^{\mathrm{T}}B)$*, which makes* $\langle K, I - R\rangle$ *a Morse function defined on* $\mathrm{SO}(3)$*. Let* $\mathcal{S} \subset \mathrm{SO}(3)$ *be a closed subset containing the identity in its interior, defined by*

$$\mathcal{S} = \left\{R \in \mathrm{SO}(3) \,:\, R_{ii} \geq 0 \text{ and } R_{ij}R_{ji} \leq 0, \forall i,\ j \in \{1,2,3\},\ i \neq j\right\}. \tag{3.8}$$

Then for $\forall R \in \mathcal{S}$*, we have*

$$s_K(R)^{\mathrm{T}} s_K(R) \geq \langle K, I - R\rangle. \tag{3.9}$$

Definition 3.3.1. *Define the time derivative of* $s_K(R)$ *as* $w(R, \Omega)$*, given by:*

$$w(R, \Omega) = \frac{\mathrm{d}}{\mathrm{d}t} s_K(R) = \sum_{i=1}^{3} K_i \mathbf{e}_i \times (\Omega \times R^{\mathrm{T}} \mathbf{e}_i), \tag{3.10}$$

where $s_K(R)$ *is defined by* (3.7)*,* R *and* Ω *are defined by* (3.6)*.*

Remark 3.3.1 (Almost global domain of attraction)**.** (Sanyal, Nordkvist, and Chyba, 2010), (Sanyal and Chaturvedi, 2008) We know that the subset of $\mathrm{SO}(3)$ where $s_K(R) = 0, R \in \mathrm{SO}(3)$, which is also the set of critical points for $\langle I - R, K \rangle$, is

$$C \triangleq \{I, \mathrm{diag}(1, -1, -1), \mathrm{diag}(-1, 1, -1), \mathrm{diag}(-1, -1, 1)\} \subset \mathrm{SO}(3). \tag{3.11}$$

In addition, the global minimum of Morse-Function is $R = I$.

3.4 ESO estimations and errors

The ESO design on $\mathrm{SE}(3)$ is split into translational ESO (TESO) design on vector space $\mathbb{R}^3$ and rotational ESO (RESO) design on $\mathrm{SO}(3)$.

Let $(\widehat{b}, \widehat{v}, \widehat{\varphi}_D) \in \mathbb{R}^3 \times \mathbb{R}^3 \times \mathbb{R}^3$ denote the estimated translational position, velocity, and disturbance forces as the states of TESO. We define the estimation errors of TESO by:

$$e_b = b^m - \widehat{b}, e_v = v^m - \widehat{v}, e_\varphi = \varphi_D - \widehat{\varphi}_D, \tag{3.12}$$

which are the estimation errors of translational position, velocity, and total disturbance force, respectively. The input-output diagram of the TESO is presented in Figure 3.2.

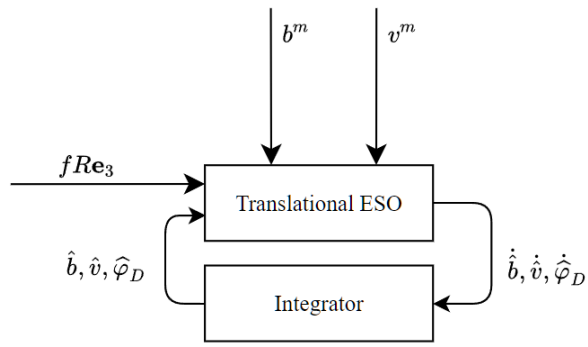

FIGURE 3.2: The block diagram of TESO

Let $(\widehat{R}, \widehat{\Omega}, \widehat{\tau}_D) \in \mathrm{SO}(3) \times \mathbb{R}^3 \times \mathbb{R}^3$ denote the estimated attitude, angular velocity, and disturbance torque as the states of RESO. We define the attitude estimation error by:

$$E_R = \widehat{R}^{\mathrm{T}} R^m, \tag{3.13}$$

on $\mathrm{SO}(3)$. We define the angular velocity and torque disturbance estimation errors by:

$$e_\Omega = \Omega^m - E_R^{\mathrm{T}} \widehat{\Omega},\ e_\tau = \tau_D - \widehat{\tau}_D, \tag{3.14}$$

which are expressed on the vector space $\mathbb{R}^3$. The input-output diagram of the rotational ESO is presented in Figure 3.3.

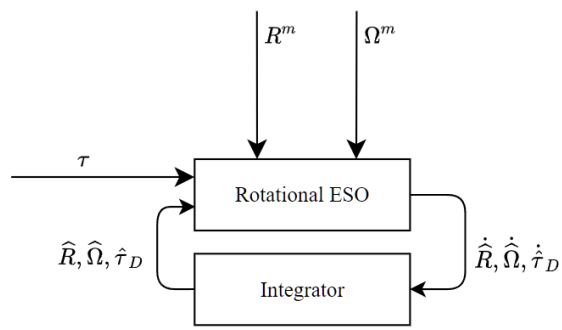

FIGURE 3.3: The block diagram of RESO

A properly designed ESO on SE(3)is expected to stabilize the error state e_b, e_v, e_φ, E_R, e_Ω, e_τ at the origin $e_b = 0$, $e_v = 0$, $e_\varphi = 0$, $E_R = I$, $e_\Omega = 0$, $e_\tau = 0$, when there are no measurement uncertainties, such that ν_b, ν_v, ν_R, $\nu_\Omega = 0$. Moreover, when the measurement uncertainties are non-negligible, the ESO is expected to drive the error state to a small neighbourhood around the origin.

3.5 Tracking error kinematics and dynamics

Let $g^d(t) \in \mathrm{SE}(3)$ denote the desired pose generated by a guidance scheme (Sanyal, Nordkvist, and Chyba, 2010). Let v^d denote the desired translational velocity in the inertial frame $\mathcal{E}$, and Ω^d denote the body's reference angular velocity in the body frame $\mathcal{B}$. Then, the tracking error is given by

$$(\widetilde{b}, Q) \in \mathrm{SE}(3), \tag{3.15}$$

where $Q = (R^d)^{\mathrm{T}} R$ is the attitude tracking error in the frame $\mathcal{B}$, and $b = b - b^d$ is the position tracking error in the frame $\mathcal{E}$. The translational velocity tracking error is given

by:

$$\widetilde{v} = v - v^d. \tag{3.16}$$

The angular velocity tracking error is given by:

$$\omega = \Omega - Q^{\mathrm{T}}\Omega^d. \tag{3.17}$$

Thus, in the inertial frame $\mathcal{E}$, the translational tracking error kinematics and dynamics can be summarized as

$$\begin{aligned} \dot{\widetilde{b}} &= \widetilde{v}, \\ m\dot{\widetilde{v}} &= mg\mathbf{e}_3 - fR\mathbf{e}_3 + \varphi_D - m\dot{v}^d, \end{aligned} \tag{3.18}$$

in the body-fixed frame $\mathcal{B}$, the rotational tracking error kinematics and dynamics can be summarized as

$$\begin{aligned} \dot{Q} &= Q\omega^{\times}, \\ J\dot{\omega} &= \tau + \tau_D + J(\omega^{\times}Q^{\mathrm{T}}\Omega^d - Q^{\mathrm{T}}\dot{\Omega}^d) + (J\Omega) \times \Omega. \end{aligned} \tag{3.19}$$

Since the translational error dynamics is expressed in the inertial frame, the rotational error dynamics is decoupled from the translational error dynamics such that the translation control force, f, is obtained in the inertial frame followed by the appropriate attitude control, τ, in body frame to track the desired trajectory, b^d.

With the tracking error and corresponding dynamics of the UAV, we formulate two

ADRC architectures, named as measured and estimated feedback architecture, respectively. These two control architectures are adopted in the rest part of the dissertation. In the measured feedback architecture, the motion feedback is from the direct measurements b^m, v^m, R^m, Ω^m. With direct measurements, we denote the feedback tracking error in measured feedback architecture as $\widetilde{b}^m, \widetilde{v}^m, Q^m, \omega^m$, defined by,

$$\widetilde{b}^m = b^m - b^d, \widetilde{v}^m = v^m - v^d, Q^m = (R^d)^{\mathrm{T}} R^m, \omega^m = \Omega^m - (Q^m)^{\mathrm{T}} \Omega^d. \tag{3.20}$$

They are corresponding with $\widetilde{b}, \widetilde{v}, Q, \omega$ defined by (3.15), (3.16), and (3.17), respectively. The ESO provides $\widehat{\varphi}_D$ and $\widehat{\tau}_D$ for disturbance rejection. The control diagram of the measured feedback architecture is presented in Figure 3.4.

Similarly, in the estimated feedback architecture, the ESO provides $\widehat{b}, \widehat{v}, \widehat{R}, \widehat{\Omega}, \widehat{\varphi}_D, \widehat{\tau}_D$ for both state feedback and disturbance rejection. We denote the feedback tracking error in estimated feedback architecture as $\widetilde{b}^e, \widetilde{v}^e, Q^e, \omega^e$, defined by

$$\widetilde{b}^e = \widehat{b} - b^d, \widetilde{v}^e = \widehat{v} - v^d, Q^e = (R^d)^{\mathrm{T}} \widehat{R}, \omega^e = \widehat{\Omega} - (Q^e)^{\mathrm{T}} \Omega^d. \tag{3.21}$$

The control diagram of the estimated feedback architecture is presented in Figure 3.5.

Theoretically, since the ESO can estimate the state and the disturbance simultaneously with stability assurance, we assume that the estimated state is closer to the ground truth state than the measured one. This assumption implies that estimated feedback architecture have better control performance than the measured feedback one in identical conditions. The discussion on this comparison is posed in the numerical simulations covered in Chapters 4 and 5. We assume perfect measurement or estimation in the control designs to

establish a fair comparison. In the control designs and stability proofs covered in Propositions 4.2.2, 4.2.1, 5.2.2, 5.2.1, and Theorems 5.2.1, 5.2.2, the tracking control laws and the corresponding error dynamics are expressed by the ground truth motion states expressed by (3.4) and ground truth tracking errors expressed by (3.15), (3.16), (3.17), so that these control designs can be expressed with both architectures by replacing the ground truth motion states and tracking errors with the estimated or measured ones.

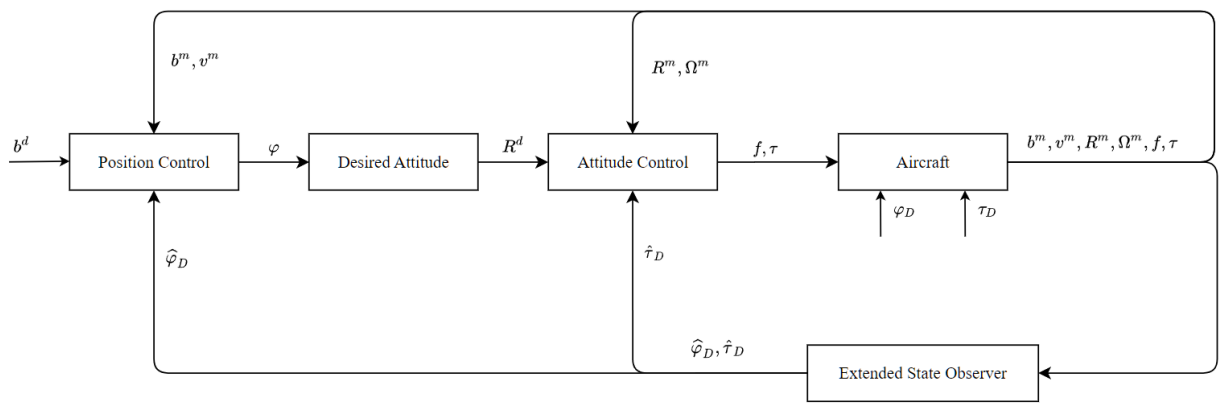

FIGURE 3.4: The block diagram of ADRC scheme with measured feedback

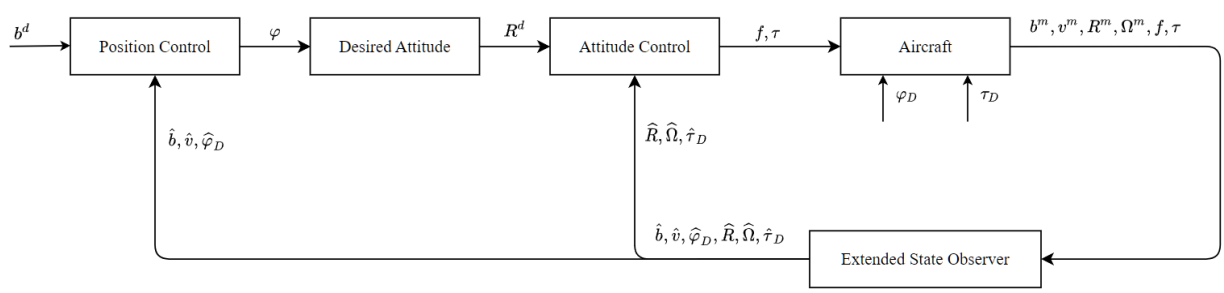

FIGURE 3.5: The block diagram of ADRC scheme with estimated feedback

3.6 Summary

This chapter formulates the ESO and ADRC problems on $\mathrm{SE}(3)$, and covers the corresponding mathematical preliminaries. With the formulated ESO and tracking control errors, we present two ADRC architectures on $\mathrm{SE}(3)$ in Figures 3.4 and 3.5. The architectures covered in this chapter are adopted in the rest part of the dissertation.

Chapter 4

Asymptotically Stable Active Disturbance Rejection Control (AS-ADRC)

Based on the tracking control and extended state observer (ESO) problems addressed in Chapter 3, this chapter describes the AS-ADRC scheme in detail. We organize the chapter as follows. Section 4.1 describes the exponentially stable extended states observer (ES-ESO) design on $\mathrm{SE}(3)$ with its stability analysis in detail. Section 4.2 obtains the asymptotically stable position and attitude tracking control law for stable tracking control with disturbance rejection from the estimated disturbances by ES-ESO described in Section 4.1. Two sets of numerical simulation results are presented in this chapter. In Section 4.4, the first set of results present the disturbance estimation performance of the proposed ES-ESO. In Section 4.5, we present the second set of numerical simulations to investigate the flight control performance of the proposed AS-ADRC scheme. In the simulation, the desired flight trajectory of the aircraft is designed to let the unmanned aerial vehicle (UAV) flight control scheme experience the singularity point of the pose representation. Lie group variational integrator (LGVI) discretizes the simulations in Section 4.4 and 4.5. We conclude this chapter in Section 4.6 by summarizing the results and highlighting directions for forthcoming research.

4.1 Exponentially stable extended states observer (ES-ESO)

4.1.1 ES-ESO: Translational motion

Proposition 4.1.1 (ES-ESO: Translational motion)**.** *Define the positive scalar gains k_{t1} and k_{t2}, which make the matrix $\mathcal{A}_t \in \mathbb{R}^{2\times 2}$ defined by:*

$$\mathcal{A}_t = \begin{bmatrix} -k_{t1} & 1 \\ -k_{t2} & 0 \end{bmatrix}, \tag{4.1}$$

a Hurwitz matrix. Define the positive scalar gain $\kappa_t > 1/2$. Consider the following ESO design:

$$\begin{aligned} \dot{\widehat{b}} &= \widehat{v} \\ m\dot{\widehat{v}} &= mg\mathbf{e}_3 - fR^m\mathbf{e}_3 + mk_{t1}\psi_t + m\kappa_t e_v + \widehat{\varphi}_D \\ \dot{\widehat{\varphi}}_D &= mk_{T2}\psi_t, \end{aligned} \tag{4.2}$$

where ψ_t is defined by:

$$\psi_t = e_v + \kappa_t e_b. \tag{4.3}$$

Theorem 4.1.1. *With the observer errors defined by* (3.12)*, the translational kinematics and dynamics given by* (3.4)*, and the translational ESO given by* (4.2)*, the error dynamics of the ESO is*

given by:

$$\begin{aligned} \dot{e}_b &= e_v, \\ m\dot{e}_v &= -mk_{t1}\psi_t - m\kappa_t e_v + e_\varphi, \\ \dot{e}_\varphi &= -mk_{t2}\psi_t + \dot{\varphi}_D. \end{aligned} \tag{4.4}$$

The error dynamics (4.4) *is exponentially stable at the origin* $(e_b = 0, e_v = 0, e_\varphi = 0)$*, when the resultant disturbance force is constant* $(\dot{\varphi}_D = 0)$ *and the measurement uncertainties are negligible* $(\nu_b = 0, \nu_v = 0)$*.*

Proof. Substituting the time derivative of (4.3) in (4.4), we obtain

$$\begin{aligned} \dot{e}_b &= e_v \\ \dot{\psi}_t &= -k_{t1}\psi_t + m^{-1}e_\varphi \\ m^{-1}\dot{e}_\varphi &= -k_{t2}\psi_t. \end{aligned} \tag{4.5}$$

Next, for $\mathcal{A}_t$ as defined in (4.1), $\forall\ \mathcal{Q}_t \in \mathbb{R}^{2\times 2}$ where $\mathcal{Q}_t \succ 0$, the Lyapunov equation,

$$\mathcal{A}_t^{\mathrm{T}}\mathcal{P}_t + \mathcal{P}_t\mathcal{A}_t = -\mathcal{Q}_t, \tag{4.6}$$

has a unique solution $\mathcal{P}_t$. Thereafter, define the Lyapunov function V_t:

$$V_t = V_{t0} + \mu_t e_b^{\mathrm{T}} e_b, \text{ where } V_{t0} = \zeta_t^{\mathrm{T}}\mathcal{P}_t\zeta_t, \tag{4.7}$$

and ζ_t is defined as:

$$\zeta_t = [\psi_t^{\mathrm{T}},\ m^{-1}e_\varphi^{\mathrm{T}}]^{\mathrm{T}}.$$

We define μ_t as a positive scalar, where μ_t is constrained by:

$$0 < \mu_t < \frac{\lambda_{\min}\{\mathcal{Q}_t\}\,\lambda_{\min}\{\mathcal{P}_t\}}{\lambda_{\max}\{\mathcal{P}_t\}}. \tag{4.8}$$

By substituting (4.5), we further obtain the time derivative of V_t as:

$$\begin{aligned}
\dot{V}_t &= \dot{\zeta}_t^{\mathrm{T}}\mathcal{P}_t\zeta_t + \zeta_t^{\mathrm{T}}\mathcal{P}_t\dot{\zeta}_t + 2\mu_t e_b^{\mathrm{T}} e_v \\
&= -\zeta_t^{\mathrm{T}}\mathcal{Q}_t\zeta_t + 2\mu_t e_b^{\mathrm{T}}(\psi_t - \kappa_t e_b) \\
&\leq -\zeta_t^{\mathrm{T}}\mathcal{Q}_t\zeta_t - (2\kappa_t - 1)\mu_t e_b^{\mathrm{T}} e_b + \mu_t\psi_t^{\mathrm{T}}\psi_t \\
&\leq -\left(\frac{\lambda_{\min}\{\mathcal{Q}_t\}}{\lambda_{\max}\{\mathcal{P}_t\}} - \frac{\mu_t}{\lambda_{\min}\{\mathcal{P}_t\}}\right) V_{t0} - (2\kappa_t - 1)\mu_t e_b^{\mathrm{T}} e_b \\
&\leq -\gamma_t V_t,
\end{aligned} \tag{4.9}$$

where γ_t is a positive constant defined by:

$$\gamma_t = \min\left\{\frac{\lambda_{\min}\{\mathcal{Q}_t\}}{\lambda_{\max}\{\mathcal{P}_t\}} - \frac{\mu_t}{\lambda_{\min}\{\mathcal{P}_t\}}, 2\kappa_t - 1\right\}.$$

Based on the inequality (4.9), we conclude that the ESO error dynamics (4.4) is exponentially stable at the origin. This concludes the proof of Theorem 4.1.1. □

4.1.2 ES-ESO: Rotational motion

Proposition 4.1.2 (ES-ESO: Rotational motion)**.** *Define $e_R = s_k(E_R)$, where $s_K(\cdot)$ is defined in Lemma 3.3.1. Define $e_w = w(E_R, e_\Omega)$ by applying* (3.10)*. Define the positive scalar gains k_{a1} and k_{a2}, which make the matrix $\mathcal{A}_a \in \mathbb{R}^{2\times 2}$ defined as:*

$$\mathcal{A}_a = \begin{bmatrix} -k_{a1} & 1 \\ -k_{a2} & 0 \end{bmatrix}, \tag{4.10}$$

a Hurwitz matrix. Define the positive scalar gain $\kappa_a > 1/2$. Consider the following ESO design,

$$\begin{aligned} \dot{\widehat{R}} &= \widehat{R}\widehat{\Omega}^{\times} \\ \dot{\widehat{\Omega}} &= E_R J^{-1}\left[J\Omega \times \Omega + \tau\right] + E_R J^{-1}\left[k_{a1} J\psi_a + \kappa_a J e_w + \widehat{\tau}_D\right] + E_R e_\Omega^{\times} E_R^{\mathrm{T}} \widehat{\Omega}, \\ \dot{\widehat{\tau}}_D &= J k_{a2} \psi_a, \end{aligned} \tag{4.11}$$

where ψ_a is defined by:

$$\psi_a = e_\Omega + \kappa_a e_R. \tag{4.12}$$

Theorem 4.1.2. *With the observer errors for the rotational ESO defined by* (3.13)*,* (3.14)*, the rotational kinematics and dynamics given by* (3.4)*, and the ESO for rotational motion given in Proposition 4.1.2, the error dynamics of the ESO is given by:*

$$\begin{aligned} \dot{E}_R &= E_R e_\Omega^{\times}, \\ J\dot{e}_\Omega &= -k_{a1} J\psi_a - \kappa_a J e_w + e_\tau, \\ \dot{e}_\tau &= -k_{a2} J\psi_A + \dot{\tau}_D. \end{aligned} \tag{4.13}$$

When the resultant disturbance torque is constant $(\dot{\tau}_D = 0)$ *and the measurement uncertainties are negligible* $(\nu_R = 0, \nu_\Omega = 0)$*, the error dynamics* (4.13) *is almost global exponentially stable to the origin* $(E_R = I, e_\Omega = 0, e_\tau = 0)$*, except for some critical points of initial conditions.*

Proof. From (4.13), by substituting the time derivative of (4.12), we obtain

$$\begin{aligned} \dot{E}_R &= E_R e_\Omega^\times \\ \dot{\psi}_a &= -k_{a1}\psi_a + J^{-1}e_\tau \\ J^{-1}\dot{e}_\tau &= -k_{a2}\psi_a. \end{aligned} \tag{4.14}$$

Next, for $\mathcal{A}_a$ as defined in (4.10), $\forall\ \mathcal{Q}_a \in \mathbb{R}^{2\times 2}$ where $\mathcal{Q}_a \succ 0$, the Lyapunov equation:

$$\mathcal{A}_a^{\mathrm{T}}\mathcal{P}_a + \mathcal{P}_a\mathcal{A}_a = -\mathcal{Q}_a, \tag{4.15}$$

has a unique solution $\mathcal{P}_a$. Thereafter, define the Lyapunov function V_a:

$$V_a = V_{a0} + \mu_a\langle K, I - E_R\rangle, \text{ where } V_{a0} = \zeta_a^{\mathrm{T}}\mathcal{P}_a\zeta_a, \tag{4.16}$$

and ζ_a is defined as:

$$\zeta_a = [\psi_a^{\mathrm{T}},\ J^{-1}e_\tau^{\mathrm{T}}]^{\mathrm{T}}.$$

We define μ_a as a positive scalar, where μ_a is constrained by:

$$0 < \mu_a < \frac{2\lambda_{\min}\{\mathcal{Q}_a\}\,\lambda_{\min}\{\mathcal{P}_a\}}{\lambda_{\max}\{\mathcal{P}_a\}}. \tag{4.17}$$

With (4.14), we obtain the time derivative of V_A as follows,

$$\begin{aligned}\dot{V}_a &= \dot{\zeta}_a^{\mathrm{T}}\mathcal{P}_a\zeta_a + \zeta_a^{\mathrm{T}}\mathcal{P}_a\dot{\zeta}_a + \mu_a e_R^{\mathrm{T}} e_\Omega \\ &= -\zeta_a^{\mathrm{T}}\mathcal{Q}_a\zeta_a + \mu_a e_R^{\mathrm{T}}(\psi_a - \kappa_a e_R) \\ &\leq -\zeta_a^{\mathrm{T}}\mathcal{Q}_a\zeta_a - \left(\kappa_a - \frac{1}{2}\right)\mu_a e_R^{\mathrm{T}} e_R + \frac{1}{2}\mu_a \psi_a^{\mathrm{T}}\psi_a\end{aligned} \tag{4.18}$$

By applying the inequality (3.9) in Lemma 3.3.1, from (4.18), we obtain

$$\begin{aligned}\dot{V}_a &\leq -\left(\frac{\lambda_{\min}\{\mathcal{Q}_a\}}{\lambda_{\max}\{\mathcal{P}_a\}} - \frac{\mu_a}{2\lambda_{\min}\{\mathcal{P}_a\}}\right)V_{a0} - \left(\kappa_a - \frac{1}{2}\right)\mu_a\langle K, I - E_R\rangle \\ &\leq -\gamma_a V_a,\end{aligned} \tag{4.19}$$

where γ_a is a positive constant, given by:

$$\gamma_a = \min\left\{\frac{\lambda_{\min}\{\mathcal{Q}_a\}}{\lambda_{\max}\{\mathcal{P}_a\}} - \frac{\mu_a}{2\lambda_{\min}\{\mathcal{P}_a\}}, \kappa_a - \frac{1}{2}\right\}. \tag{4.20}$$

Based on the inequality (4.19), we conclude that the ESO error dynamics (4.13) is almost-global exponentially stable at the origin. This concludes the proof of Theorem 4.1.2. □

Remark 4.1.1. We assume $\dot{\varphi}_D, \dot{\tau}_D$ are not negligible, such that $\dot{\varphi}_D, \dot{\tau}_D \neq 0$. According to Definition 4.8 and Theorem 4.18 in (Khalil, 2002), when the ESO gains defined by Propositions 4.1.1, 4.1.2 make the solutions of Lyapunov equations (4.6), (4.15) satisfy:

$$\begin{aligned}\frac{\lambda_{\min}\{\mathcal{Q}_t\}}{\lambda_{\max}\{\mathcal{P}_t\}} - \frac{\mu_t}{\lambda_{\min}\{\mathcal{P}_t\}} &> \frac{\lambda_{\max}\{\mathcal{P}_t\}}{\lambda_{\min}\{\mathcal{P}_t\}}, \\ \frac{\lambda_{\min}\{\mathcal{Q}_a\}}{\lambda_{\max}\{\mathcal{P}_a\}} - \frac{\mu_a}{2\lambda_{\min}\{\mathcal{P}_a\}} &> \frac{\lambda_{\max}\{\mathcal{P}_a\}}{\lambda_{\min}\{\mathcal{P}_a\}},\end{aligned} \tag{4.21}$$

the estimation errors of the proposed ES-ESO are almost globally uniformly ultimately bounded. We omit the proof for brevity.

4.2 AS-ADRC

The position and attitude tracking control schemes by (Sanyal, Nordkvist, and Chyba, 2010) are reproduced here. The AS-ADRC scheme comprises the ES-ESO design in Section 4.1 and the tracking control scheme by (Sanyal, Nordkvist, and Chyba, 2010) to obtain better flight control performance under disturbance forces and torques. We present the position and attitude tracking control law here in Proposition 4.2.1 and Proposition 4.2.2.

Proposition 4.2.1 (Position tracking control)**.** (Sanyal, Nordkvist, and Chyba, 2010) *Consider the translational tracking control law*

$$fR\mathbf{e}_3 = mg\mathbf{e}_3 + P\widetilde{b} + L\widetilde{v} - m\dot{v}_d + \widehat{\varphi}_D, \tag{4.22}$$

where $\widehat{\varphi}_D$ is obtained from the translational ESO given in Proposition 4.1.1. With the control law (4.22)*, when the disturbance estimation error of the ESO is negligible, such that $\|e_\varphi\| = 0$, the translational error dynamics given by* (3.18) *is asymptotically stable.*

Proposition 4.2.2 (Attitude tracking control)**.** (Sanyal, Nordkvist, and Chyba, 2010) *Consider the attitude tracking control law*

$$\tau = -k_P s_K(Q) - k_D\omega - \widehat{\tau}_D + J(Q^{\mathrm{T}}\dot{\Omega}^d - \omega^{\times}Q^{\mathrm{T}}\Omega^d) - J\Omega \times Q^{\mathrm{T}}\Omega^d, \tag{4.23}$$

where $s_K(\cdot)$ is defined by Lemma 3.3.1, and $\widehat{\tau}_D$ is obtained from rotational ESO given in Proposition 4.1.2. With the control law (4.23)*, when the disturbance estimation error of the ESO is*

negligible, such that $\|e_\tau\| = 0$*, the attitude error dynamics* (3.19) *is stabilized to be asymptotically stable.*

The desired attitude R^d and desired angular velocity Ω^d in Proposition 4.2.2 is generated from the desired force $fR\mathbf{e}_3$ from Proposition 4.2.1 by applying the Hopf fibration method by (Watterson and Kumar, 2019). The almost global stability proofs of the Proposition 4.2.1 and 4.2.2 are close to the Lyapunov analysis by (Sanyal, Nordkvist, and Chyba, 2010) and are omitted here for brevity.

4.3 AS-ADRC: Implementation with realistic feedback

In control practice, the perfect feedback assumption is no longer reliable. The feedback either comes from the measurement from UAV or the estimation from ESO. In this section, we adopt the feedback architectures described in Section 3.5. Based on the tracking laws given by Propositions 4.2.2 and 4.2.1, we present the implementable AS-ADRC schemes in measured feedback and estimated feedback.

Measured feedback AS-ADRC:

The tracking control law for measured feedback architecture is given by:

$$\begin{aligned} fR^m\mathbf{e}_3 &= mg\mathbf{e}_3 + P\widetilde{b}^m + L\widetilde{v}^m - m\dot{v}_d + \widehat{\varphi}_D, \\ \tau &= -k_P s_K(Q^m) - k_D\omega^m - \widehat{\tau}_D \\ &\quad + J\left[(Q^m)^{\mathrm{T}}\dot{\Omega}^d - (\omega^m)^{\times}(Q^m)^{\mathrm{T}}\Omega^d\right] - J(\Omega^m)\times(Q^m)^{\mathrm{T}}\Omega^d. \end{aligned} \tag{4.24}$$

Estimated feedback AS-ADRC:

Similarly, the tracking control law for estimated feedback architecture is given by:

$$
\begin{aligned}
fR^h\mathbf{e}_3 &= mg\mathbf{e}_3 + P\widetilde{b}^e + L\widetilde{v}^e - m\dot{v}_d + \widehat{\varphi}_D, \\
\tau &= -k_P s_K(Q^e) - k_D\omega^e - \widehat{\tau}_D \\
&\quad + J\left[(Q^e)^{\mathrm{T}}\dot{\Omega}^d - (\omega^e)^{\times}(Q^e)^{\mathrm{T}}\Omega^d\right] - J\widehat{\Omega} \times (Q^e)^{\mathrm{T}}\Omega^d.
\end{aligned}
\tag{4.25}
$$

The validity of the proposed implementable AS-ADRC schemes will be discussed in the simulations, covered in the Section 4.5.

4.4 Numerical simulation: ES-ESO

In this section, we present a set of numerical simulation results to validate the ES-ESO. The inertia information (Pounds, Mahony, and Corke, 2010) of the simulated UAV is given by:

$$
J = \mathrm{diag}([0.0820, 0.0845, 0.1377])\ \mathrm{kg}\cdot\mathrm{m}^2, \quad m = 4.34\ \mathrm{kg}. \tag{4.26}
$$

Since the target of the simulation is to validate and compare the disturbance estimation performance of ES-ESO, the realistic propeller dynamics, time-delay and actuator saturation are not included in the model in the simulation reported in this section. The tracking control scheme driving the UAV to track the desired trajectories is the asymptotically stable tracking control scheme reported in Section 4.2 without disturbance rejection terms, such that $\widehat{\tau}_D, \widehat{\varphi}_D = 0$. The control law given by 4.24 with measured feedback architecture and perfect measurement is implemented in the simulation. The LGVI (Lee, McClamroch, and Leok, 2005; Nordkvist and Sanyal, 2010) discretizes the simulation with

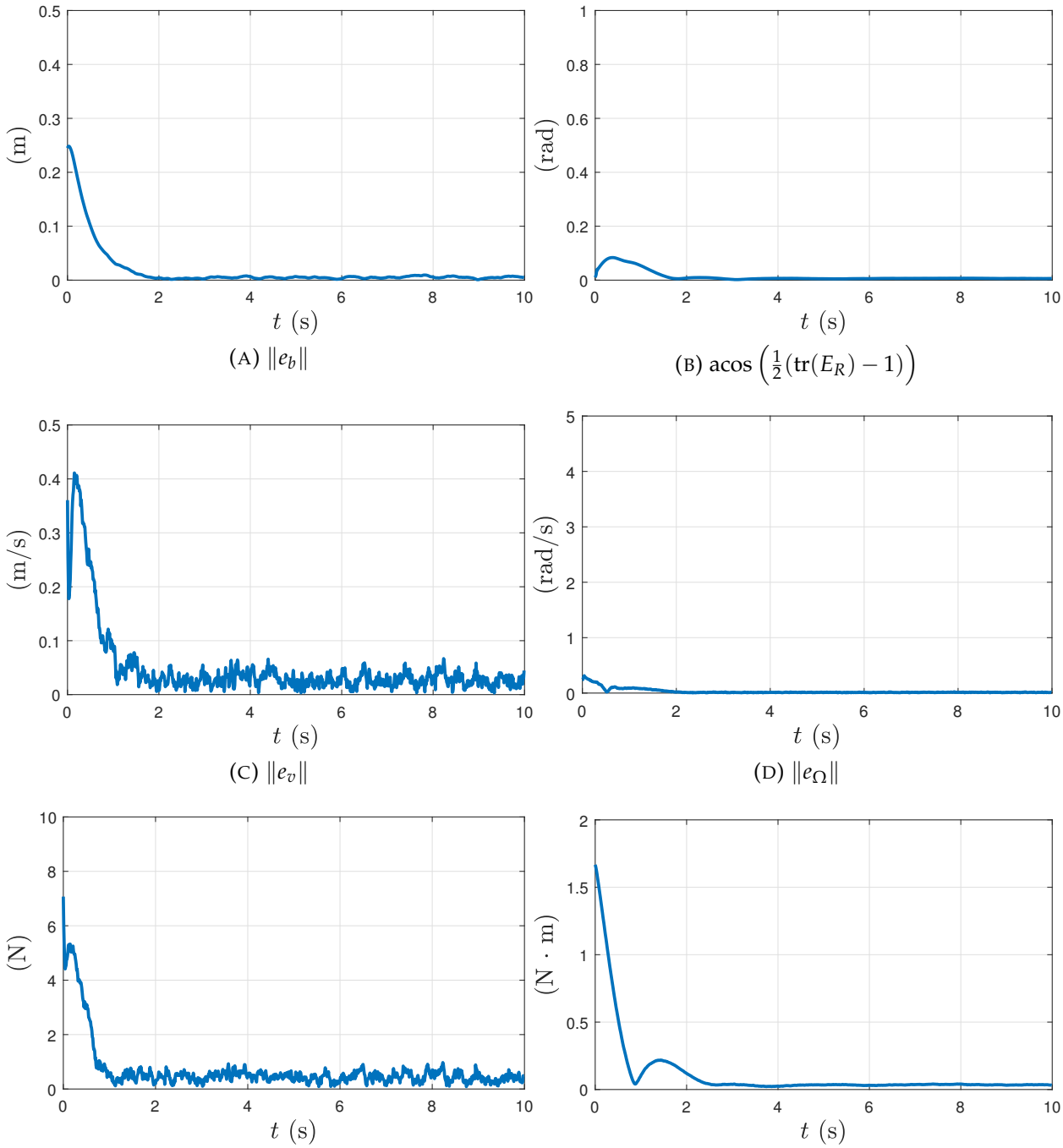

(A) $\|e_b\|$ (B) $\operatorname{acos}\left(\frac{1}{2}(\operatorname{tr}(E_R)-1)\right)$

(C) $\|e_v\|$ (D) $\|e_\Omega\|$

(E) $\|e_\varphi\|$ (F) $\|e_\tau\|$

FIGURE 4.1: Estimation error from ES-ESO in the simulated flight with 'circular' trajectory and constant disturbance

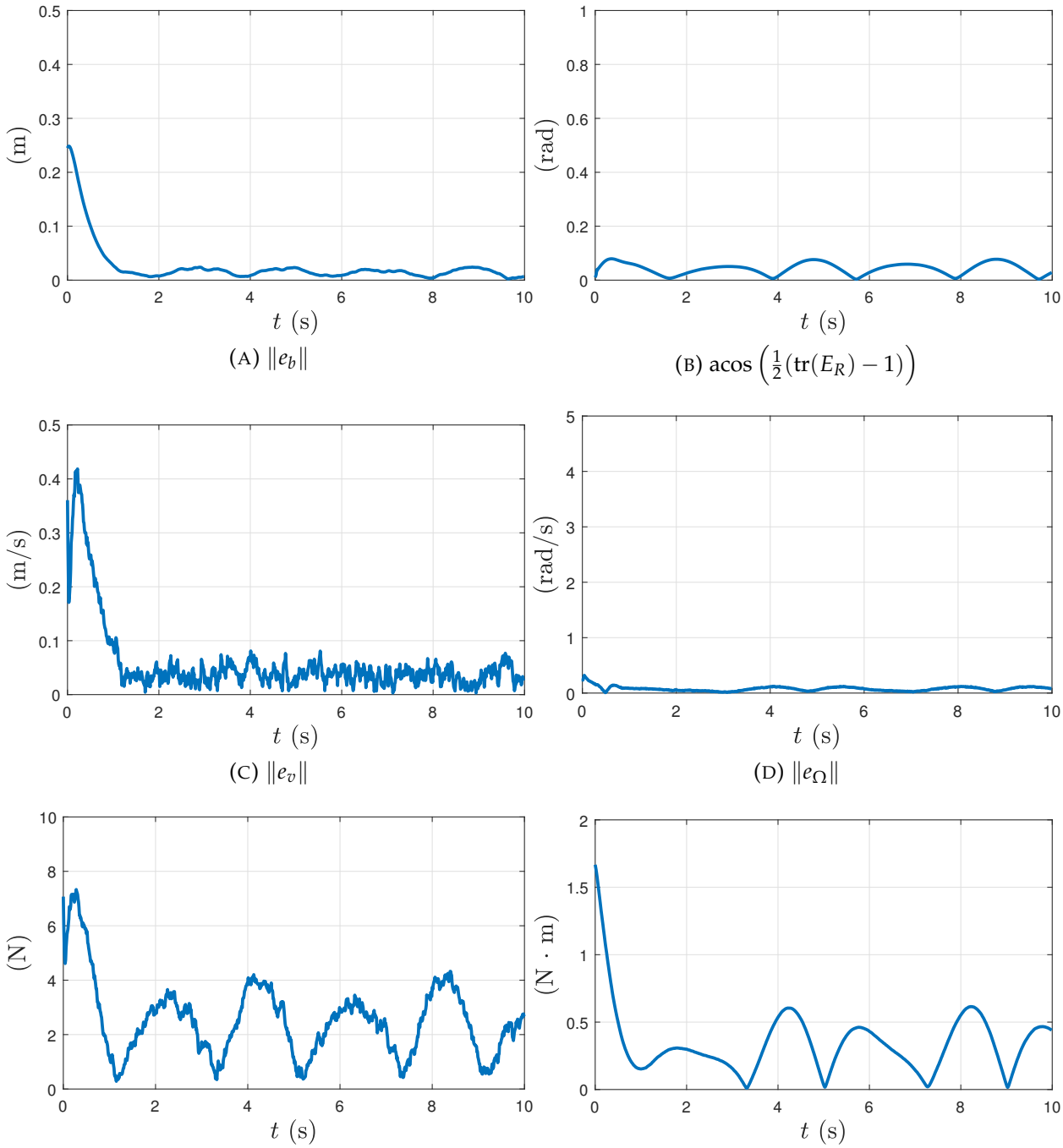

(A) $\|e_b\|$ (B) $\operatorname{acos}\left(\frac{1}{2}(\operatorname{tr}(E_R)-1)\right)$

(C) $\|e_v\|$ (D) $\|e_\Omega\|$

(E) $\|e_\varphi\|$ (F) $\|e_\tau\|$

FIGURE 4.2: Estimation error from ES-ESO in the simulated flight with 'circular' trajectory and dynamic disturbance

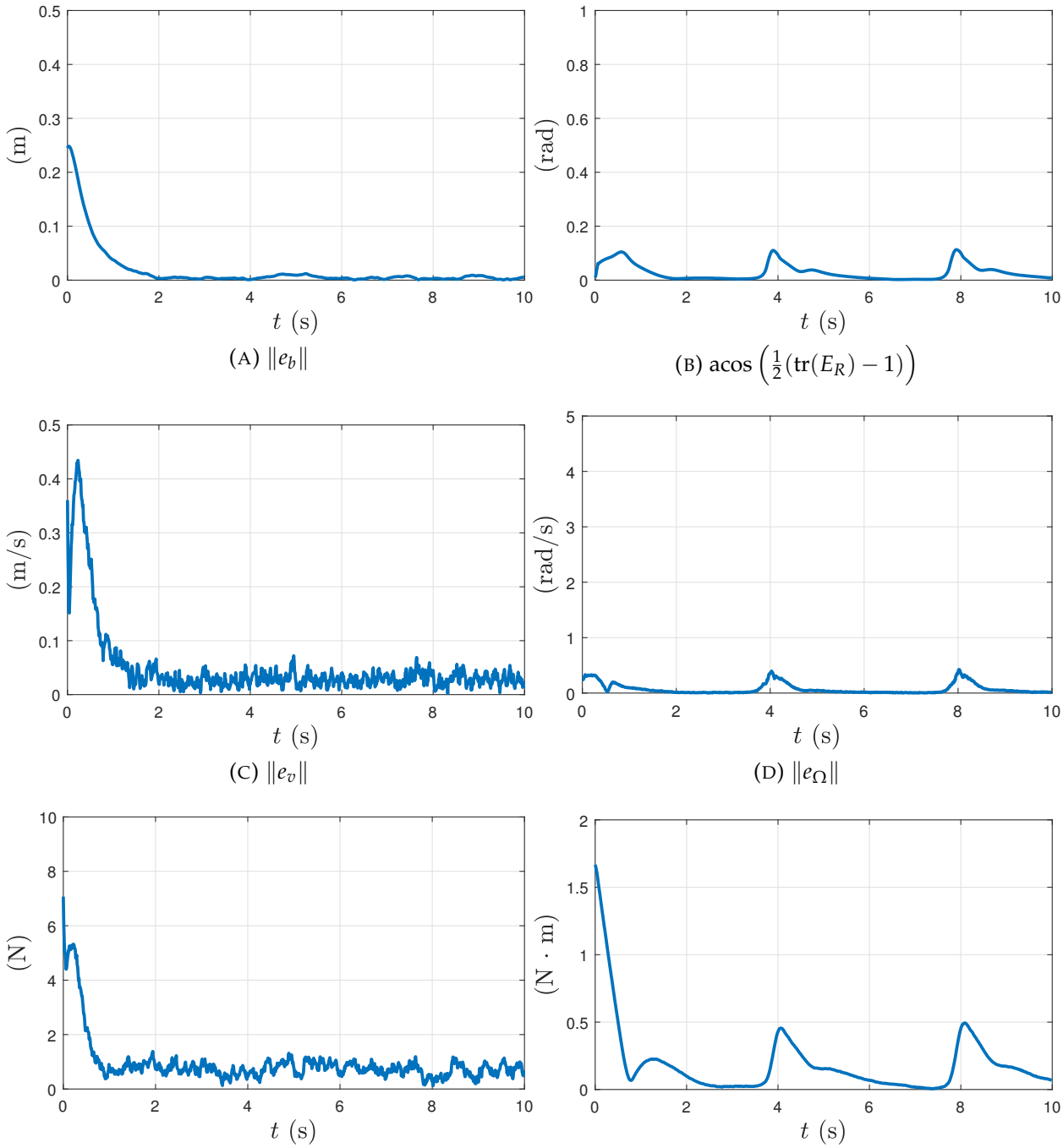

(A) $\|e_b\|$ (B) $\operatorname{acos}\left(\frac{1}{2}(\operatorname{tr}(E_R)-1)\right)$

(C) $\|e_v\|$ (D) $\|e_\Omega\|$

(E) $\|e_\varphi\|$ (F) $\|e_\tau\|$

FIGURE 4.3: Estimation error from ES-ESO in the simulated flight with 'barrel roll' trajectory and constant disturbance

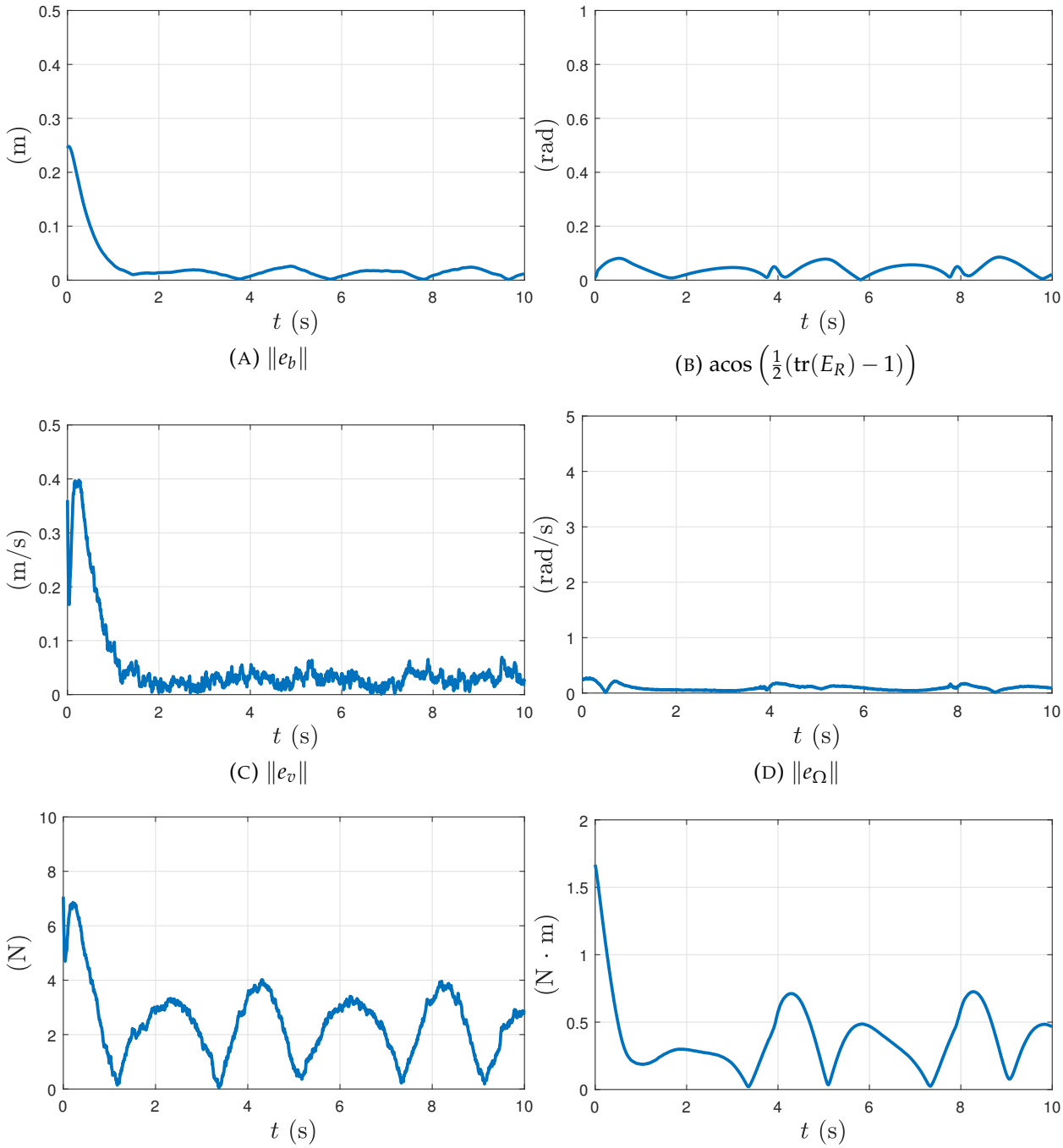

(A) $\|e_b\|$ (B) $\operatorname{acos}\left(\frac{1}{2}(\operatorname{tr}(E_R)-1)\right)$

(C) $\|e_v\|$ (D) $\|e_\Omega\|$

(E) $\|e_\varphi\|$ (F) $\|e_\tau\|$

FIGURE 4.4: Estimation error from ES-ESO in the simulated flight with 'barrel roll' trajectory and dynamic disturbance

sampling time $\Delta t = 0.01$s. The time length of the simulation is $T = 10$s. On the input of the ES-ESO $(b^m, v^m, R^m, \Omega^m)$, we model the measurements from the MTi-680G, a real-time kinematic global navigation satellite system with inertial navigation system (RTK GNSS/INS) produced by *Movella. LLC*. The measurement uncertainties are as listed in Table 4.1 in the form of normal distribution.

b^m	$b^m = b + \nu_b$	$\nu_b \sim \mathcal{N}(0, 0.0039^2)$
v^m	$v^m = v + \nu_v$	$\nu_v \sim \mathcal{N}(0, 0.05^2)$
R^m	$R^m = R\text{exp}(\nu_R^\times)$	$\nu_R \sim \mathcal{N}(0, 0.0035^2)$
Ω^m	$\Omega^m = \Omega + \nu_\Omega$	$\nu_\Omega \sim \mathcal{N}(0, 0.01^2)$

TABLE 4.1: Measurement noise level in normal distribution for the comparisons between LESO, FxTSDO, and FFTS-ESO

The gains of the proposed ES-ESO are tuned and selected as $\kappa_t = 2,\ k_{t1} = 15,\ k_{t2} = 45\ \kappa_a = 1.5;\ k_{a1} = 15;\ k_{a2} = 54$. The gains of the tracking control implementation are given by $k_P = 8, k_D = 12$ and $P = 20I, L = 40I$. Two desired trajectories with different maneuver intensities are presented here as follows. The 'circular' trajectory is expressed by:

$$b_d(t) = [2\sin(0.5\pi t),\ -2\cos(0.5\pi t),\ -3]^{\mathrm{T}}\ \mathrm{m}. \tag{4.27}$$

The 'barrel roll' trajectory is expressed by:

$$b_d(t) = [5\sin(0.5\pi t),\ -2t,\ -5\cos(0.5\pi t)]^{\mathrm{T}}\ \mathrm{m}. \tag{4.28}$$

The 'barrel roll' trajectory is with higher maneuver intensity. The norm of centripetal acceleration of the 'barrel roll' trajectory is more than one g, implying that the simulated UAV has to pitch up and flip over to track the desired trajectory. This trajectory forces the

UAV experiencing the singularity point for the pose representation, so that we validate the disturbance estimation performance under this extreme condition.

In the simulations with 'circular' trajectory, the initial conditions of the UAV motion and ESO are given by:

$$\begin{aligned}
&R(0) = I,\ \Omega(0) = [0,\ 0,\ 0]^{\mathrm{T}}\,\mathrm{rad/s},\\
&b(0) = [0,\ 0,\ -3]^{\mathrm{T}}\,\mathrm{m},\ v(0) = [2\pi,\ 0,\ 0]^{\mathrm{T}}\,\mathrm{m/s},\\
&\widehat{R}(0) = \mathrm{expmso3}([0.001,\ 0.01,\ 0.001]^{\times}),\ \widehat{\Omega}(0) = [0.1,\ 0.2,\ 0.1]^{\mathrm{T}}\,\mathrm{rad/s},\\
&\widehat{b}(0) = [0.1,\ 0.2,\ -2.9]^{\mathrm{T}}\,\mathrm{m},\ \widehat{v}(0) = [2\pi + 0.3,\ 0,\ 0.2]^{\mathrm{T}}\,\mathrm{m/s},\\
&\widehat{\tau}_D(0) = [1,\ 1,\ 1]^{\mathrm{T}}\,\mathrm{N}\cdot\mathrm{m},\ \widehat{\varphi}_D(0) = [10,\ 10,\ 10]^{\mathrm{T}}\,\mathrm{N}.
\end{aligned} \tag{4.29}$$

In the simulations with 'barrel roll' trajectory, the initial conditions of the UAV motion and ESO are given by:

$$\begin{aligned}
&R(0) = I,\ \Omega(0) = [0,\ 0,\ 0]^{\mathrm{T}}\,\mathrm{rad/s},\\
&b(0) = [0,\ 0,\ -3]^{\mathrm{T}}\,\mathrm{m},\ v(0) = [2.5\pi,\ 0,\ 0]^{\mathrm{T}}\,\mathrm{m/s},\\
&\widehat{R}(0) = \mathrm{expmso3}([0.001,\ 0.01,\ 0.001]^{\times}),\ \widehat{\Omega}(0) = [0.1,\ 0.2,\ 0.1]^{\mathrm{T}}\,\mathrm{rad/s},\\
&\widehat{b}(0) = [0.1,\ 0.2,\ -2.9]^{\mathrm{T}}\,\mathrm{m},\ \widehat{v}(0) = [2.5\pi + 0.3,\ 0,\ 0.2]^{\mathrm{T}}\,\mathrm{m/s},\\
&\widehat{\tau}_D(0) = [1,\ 1,\ 1]^{\mathrm{T}}\,\mathrm{N}\cdot\mathrm{m},\ \widehat{\varphi}_D(0) = [10,\ 10,\ 10]^{\mathrm{T}}\,\mathrm{N}.
\end{aligned} \tag{4.30}$$

The numerical simulations are conducted separately in the environment with constant and dynamic disturbances. The constant disturbance force and torque are given by:

$$\varphi_D = [10,\ 5,\ 5]^{\mathrm{T}}\,\mathrm{N}, \tau_D = [0.8,\ 0.3,\ -0.5]^{\mathrm{T}}\,\mathrm{N}\cdot\mathrm{m}. \tag{4.31}$$

The dynamic disturbance forces and torques are given by:

$$\begin{aligned} \varphi_D &= \begin{bmatrix} 10 + 6\sin(0.5\pi t) + 0.5\sin(\pi t) \\ 5 + 3\sin(0.5\pi t) + 0.2\sin(\pi t) \\ 5 \end{bmatrix} \text{N}, \\ \tau_D &= \begin{bmatrix} 0.8 + 0.5\sin(0.5\pi t) + 0.1\sin(\pi t) \\ 0.3 + 0.2\sin(0.5\pi t) + 0.05\sin(\pi t) \\ -0.5 + 0.1\sin(0.5\pi t) \end{bmatrix} \text{N} \cdot \text{m}. \end{aligned} \tag{4.32}$$

We define $\text{sat}(\cdot,\cdot) : \mathbb{R}^3 \times \mathbb{R}^+ \to \mathbb{R}^3$ to create an artificial saturation mechanism, given by:

$$\text{sat}(\tau, \overline{\tau}) = \begin{cases} \tau, \|\tau\| \leq \overline{\tau}, \\ \frac{\tau}{\|\tau\|}\overline{\tau}, \|\tau\| > \overline{\tau}. \end{cases} \tag{4.33}$$

This mechanism is adopted in the rest part of this chapter and in the numerical simulations covered in Chapter 5. By applying (4.33), we limit the magnitude of the torque actuation to be $\bar{\tau} = 10$ N·m in this section.

Figures 4.1-4.4 present the simulation results. The state estimation errors $(e_b, e_v, E_R, e_\Omega)$ and disturbance estimation errors (e_φ, e_τ) are covered in the results. Figure 4.1 presents the estimation errors from the simulated flight tracking the 'circular' trajectory given by (4.27) when exposed to the constant disturbance given by (4.31). Figure 4.1 shows that all of the estimation errors converge to a small neighborhood near the origin. However, in Figure 4.2, when the UAV tracking the identical trajectory is exposed to dynamic disturbance given by (4.32), we observe that all estimation errors experience higher fluctuation than the results in Figure 4.1. The perturbation from the dynamic disturbance causes the

fluctuation in Figure 4.2. Figure 4.3 presents the results from the flight tracking the 'barrel roll' trajectory given by (4.28) when exposed to the constant disturbance. Although the proposed tracking control scheme and ES-ESO using Lie group pose representation are singularity-free, the UAV still has to experience severe attitude maneuvers at the top of the 'barrel roll' trajectory, demanding high torque actuation. Since the numerical simulation is conducted by discretizing continuous equations with fixed time-step, severe torque actuation brings extra perturbation to the numerical schemes, and then causes the high fluctuation of the estimation errors from rotational ESO in Figure 4.3. We can relieve the impact of severe actuation by adjusting the saturation magnitude $\overline{\tau}$ in (4.33), the length of time-step δt, or applying the ESO with faster convergence speed. Figure 4.4 presents the estimation errors of the simulated flight tracking the 'barrel roll' trajectory when exposed to the dynamic disturbance. The estimation errors in Figure 4.4 have the highest fluctuation since the simulated flight experiences both challenging desired trajectory and dynamic disturbance.

To summarize, although the proposed ESO shows satisfying performance when the simulated UAV tracks the 'circular' trajectory under constant disturbance, the results from the other three simulations with more challenging flight conditions are questionable. We involve the ES-ESO in the feedback loop of AS-ADRC in the following section to evaluate its performance.

4.5 Numerical simulation: AS-ADRC

In this section, we present two sets of numerical simulation results on AS-ADRC. We command the simulated UAV to track the 'barrel roll' trajectory given by (4.28). In the

simulations presented in this section, the settings are identical to the ones given in Section 4.1, unless otherwise specified. The torque saturation in (4.33) is bounded by $\overline{\tau} = 50\,\mathrm{N{\cdot}m}$. The first set of simulations presents the performance comparison between estimated feedback architecture and measured feedback architecture. The second set uses the estimated feedback architecture and establishes the comparison between the tracking control without disturbance rejection, with only translational rejection, with only rotational rejection, and with both rejections.

4.5.1 Estimated feedback versus measured feedback

In this subsection, we present the comparison between estimated and measured feedback architectures on their tracking control performances. The control laws for estimated and measured feedback architecture are given by (4.25) and (4.24), respectively. Constant disturbance (4.31) perturbs the flights in the simulations. We activate both translational and rotational disturbance rejections to evaluate their performances comprehensively.

Figure 4.5 presents the tracking control performances of the two architectures. The position tracking error is defined as the norm of $\tilde{b}$. The attitude tracking error is defined by the principal angle, given by $\operatorname{acos}\left(\frac{1}{2}(\operatorname{tr}(Q) - 1)\right)$. Despite the questionable performance of ES-ESO presented in Section 4.1 in 'barrel roll' trajectory, we can observe that estimated AS-ADRC outperforms the measured one in Figure 4.5.

4.5.2 Partial rejection versus whole rejection

In this subsection, we present the simulation results with different configurations of disturbance rejection with estimated feedback architecture given by 3.21. The desired trajectory, the gains of tracking control scheme, and the gains of ES-ESO of AS-ADRC are all

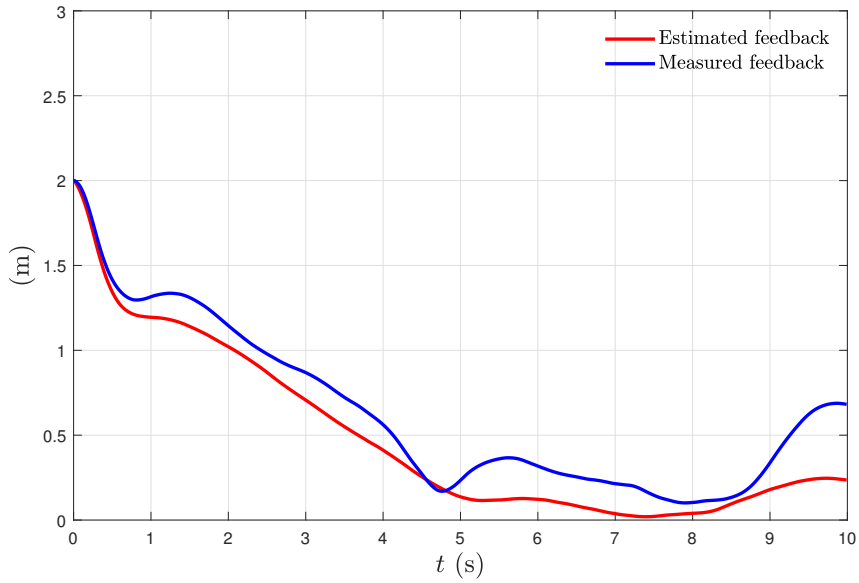

(A) $\|\tilde{b}\|$

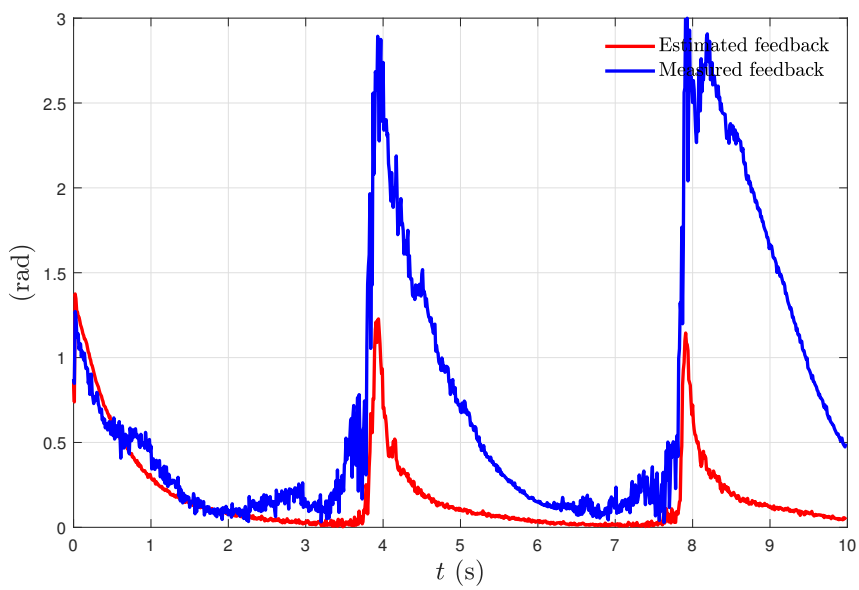

(B) $\operatorname{acos}\left(\frac{1}{2}(\operatorname{tr}(Q)-1)\right)$

FIGURE 4.5: Position and attitude tracking errors of AS-ADRC: estimated feedback versus measured feedback

identical to the ones presented in Section 4.1. In the simulation within this section, we have disturbance rejection terms in the control schemes.

Four simulation results, which are the simulations without disturbance rejection, with only translational rejection, with only rotational rejection, and with both rejection, are included in this subsection. The results are shown in Figures 4.6 and 4.7.

From Figure 4.6, we observe that all of the trajectories of the simulated flights converge to a neighborhood near the desired trajectory. Figure 4.7 compares the position and attitude tracking error during the simulated flights. From Figure 4.7, we can clearly observe the position tracking errors of 'both' and 'translational rejection' are much smaller than the other two. However, the attitude tracking errors of the four disturbance rejection configurations cannot differ from each other significantly in Figure 4.7.

To investigate the rotational disturbance rejection configuration, we enlarge the constant disturbance torque, given by:

$$\tau_D = [5,\ 0.3,\ -0.5]^{\mathrm{T}}\,\mathrm{N}\cdot\mathrm{m}, \tag{4.34}$$

and conduct the simulations again. Figure 4.8 presents the tracking control errors from the results.

Figure 4.8 indicates that the control scheme with both translational and rotational disturbance rejections has the best control performance. When the disturbance torque is considerably high, the rotational disturbance rejection can improve the attitude tracking performance. Moreover, to ensure satisfactory position tracking control performance for a UAV experiencing disturbance forces and torques, disturbance torque rejection in the attitude tracking control scheme is necessary.

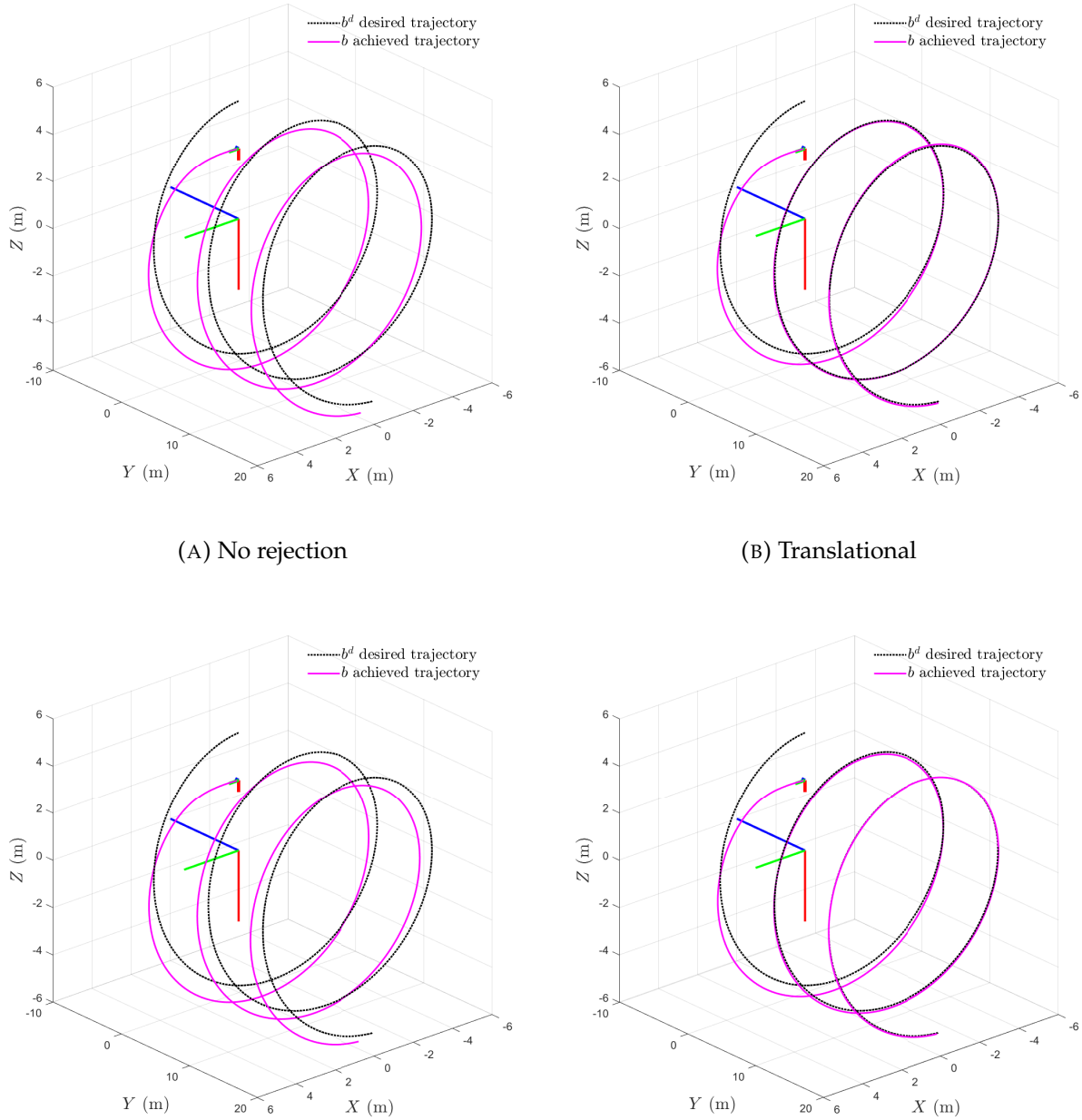

(A) No rejection

(B) Translational

(C) Rotational

(D) Whole

FIGURE 4.6: The tracked trajectories of AS-ADRC: partial rejection versus whole rejection

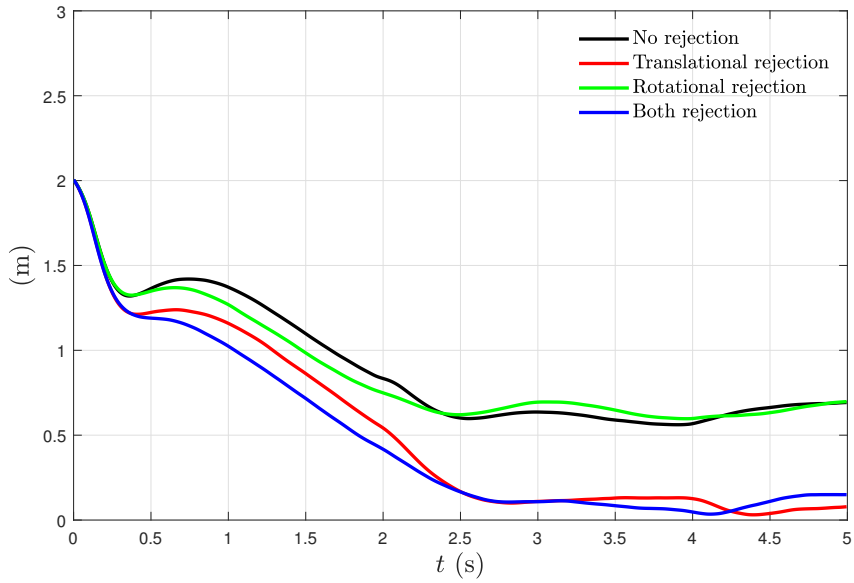

(A) $\|\tilde{b}\|$

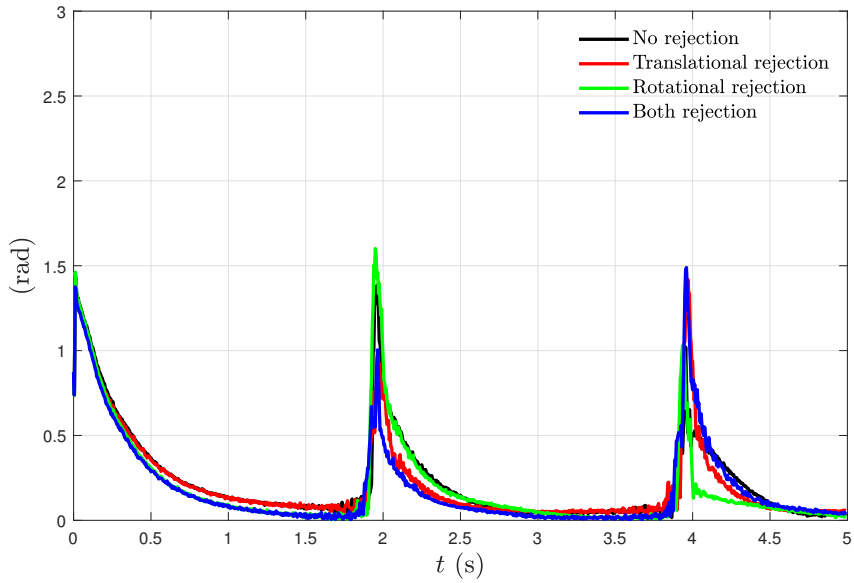

(B) $\operatorname{acos}\left(\frac{1}{2}(\operatorname{tr}(Q)-1)\right)$

FIGURE 4.7: Position and attitude tracking errors of AS-ADRC: partial rejection versus whole rejection

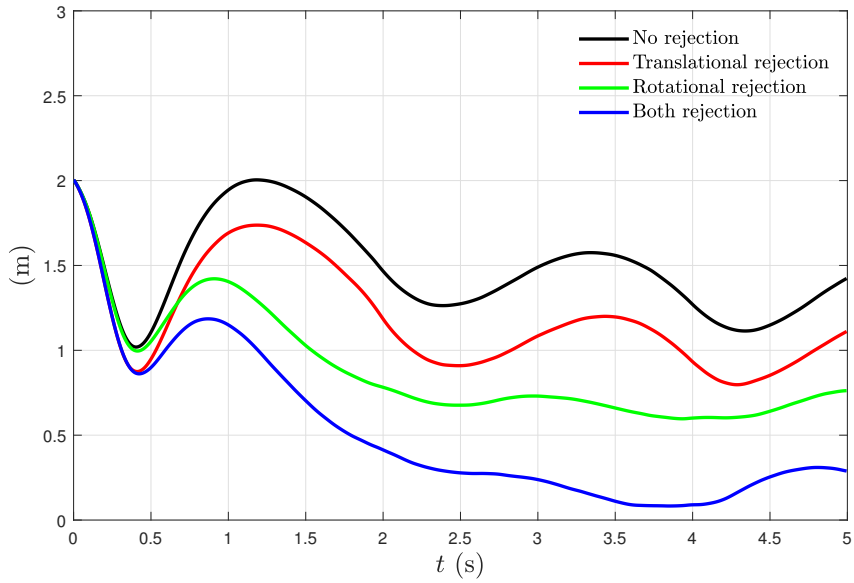

(A) $\|\tilde{b}\|$

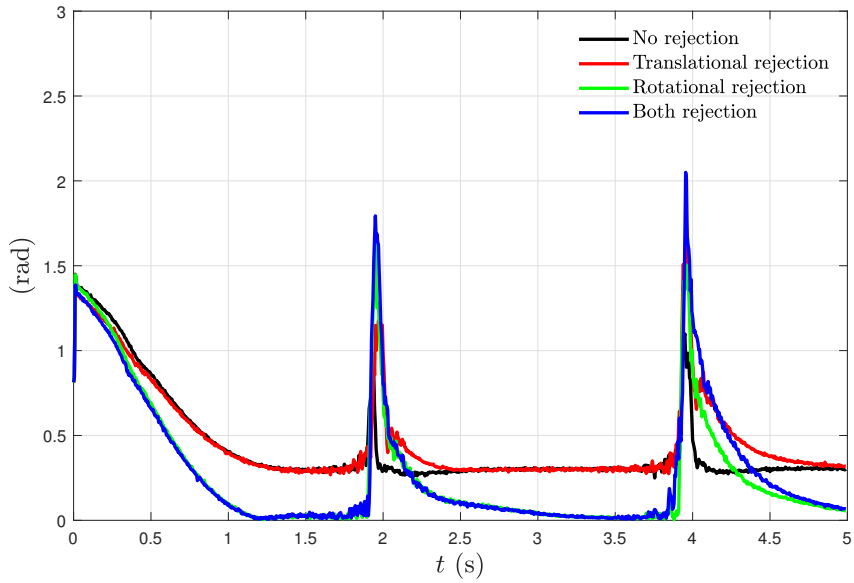

(B) $\operatorname{acos}\left(\frac{1}{2}(\operatorname{tr}(Q)-1)\right)$

FIGURE 4.8: Position and attitude tracking errors of AS-ADRC with amplified disturbance torque: partial rejection versus whole rejection

4.6 Summary

In this chapter, the AS-ADRC scheme with the ES-ESO module on $\mathrm{SE}(3)$ is presented for the rotorcraft UAV doing rapid maneuvers in the presence of aerodynamic uncertainties. The proposed ES-ESO scheme is able to give an accurate estimation of the external force and torque disturbances acting on the UAV. We provide the stability proof using Lyapunov analysis. Afterwards, we propose the AS-ADRC scheme which incorporates the disturbance estimation from ES-ESO and the AS tracking scheme on $\mathrm{SE}(3)$, by (Sanyal, Nordkvist, and Chyba, 2010). The proposed scheme is numerically implemented by LGVI for a simulated rotorcraft UAV. Two sets of numerical simulation results are presented to validate the developed ES-ESO and AS-ADRC scheme, respectively. Numerical results validate the proposed ES-ESO and AS-ADRC, and show their robustness.

Chapter 5

Fast Finite-Time Stable Active Disturbance Rejection Control (FFTS-ADRC)

As the major contribution of this dissertation, this chapter describes the FFTS-ADRC scheme in detail. The tracking control and extended state observer (ESO) problems on $SE(3)$ are formulated in Chapter 3. Section 5.1 describes the detailed fast finite-time stable extended state observer (FFTS-ESO) design based on the Hölder-continuous fast finite time stable differentiator (HC-FFTSD) reported in Chapter 2. Section 5.2 obtains the FFTS position and attitude tracking control laws for stable tracking control with the feedback on the estimated disturbances obtained from FFTS-ESO described in Section 5.1. Two sets of numerical simulation results are presented in this Chapter. In Section 5.4, the first set of results compares the proposed FFTS-ESO and other disturbance observer (DO)/ESO schemes in prior publications on their disturbance estimation performance in different scenarios. In Section 5.6, we present the second set of numerical simulations to investigate the flight control performance of the proposed FFTS-ADRC. The desired flight trajectory of the aircraft is designed to let the aircraft flight control scheme experience the singularity point of the pose representation. Lie group variational integrator (LGVI) (Lee, McClamroch, and Leok, 2005; Sanyal and Chaturvedi, 2008) discretizes the simulations

in Section 5.6 . We conclude this chapter in Section 5.7 by summarizing the results.

5.1 Fast finite-time stable extended state observer (FFTS-ESO)

5.1.1 FFTS-ESO: Translational motion

Proposition 5.1.1 (FFTS-ESO: Translational motion)**.** *Define the positive scalar gains k_{t1} and k_{t2}, which make the matrix $\mathcal{A}_t \in \mathbb{R}^{2\times 2}$ defined as:*

$$\mathcal{A}_t = \begin{bmatrix} -k_{t1} & 1 \\ -k_{t2} & 0 \end{bmatrix}, \tag{5.1}$$

a Hurwitz matrix. The ESO designed for the translational motion is given by:

$$\begin{aligned} \dot{\hat{b}} &= \hat{v}, \\ m\dot{\hat{v}} &= mg\mathbf{e}_3 - fR^m\mathbf{e}_3 + mk_{t1}\phi_1(\psi_t) + m\kappa_t\left[(e_b^{\mathrm{T}}e_b)^{\frac{1-p}{p}} H\left(e_b, \frac{p-1}{p}\right)e_v + e_v\right] + \hat{\varphi}_D, \\ \dot{\hat{\varphi}}_D &= mk_{t2}\phi_2(\psi_t), \end{aligned} \tag{5.2}$$

where ψ_t is defined as

$$\psi_t = e_v + \kappa_t\left[e_b + (e_b^{\mathrm{T}}e_b)^{\frac{1-p}{p}} e_b\right],\ \kappa_t > 1/2, \tag{5.3}$$

and $\phi_1(\cdot)$ is as defined by the expression in (2.13)*. In addition, the constant k_{t3} is defined and it occurs in the terms $\phi_1(\psi_t)$ and $\phi_2(\psi_t)$, where it takes the place of k_3 in* (2.13)*.*

Theorem 5.1.1. *Given the observer errors for the translational ESO defined by* (3.12)*, the translational kinematics and dynamics given by* (3.4)*, and the ESO for translational motion given in Proposition 5.1.1, the error dynamics of the ESO is given by:*

$$\begin{aligned}
\dot{e}_b &= e_v, \\
m\dot{e}_v &= -mk_{t1}\phi_1(\psi_t) - m\kappa_t \left[(e_b^{\mathrm{T}} e_b)^{\frac{1-p}{p}} H\left(e_b, \frac{p-1}{p}\right) e_v + e_v \right] + e_\varphi, \\
\dot{e}_\varphi &= -mk_{t2}\phi_2(\psi_t) + \dot{\varphi}_D.
\end{aligned} \tag{5.4}$$

The error dynamics (5.4) *is FFTS at the origin* $((e_b, e_v, e_\varphi) = (0,0,0))$*, when the resultant disturbance force is constant* $(\dot{\varphi}_D = 0)$ *and the measurement uncertainties are negligible* $(\nu_b = 0, \nu_v = 0)$*.*

Proof. Simplify (5.4) as:

$$\begin{aligned}
\dot{\psi}_t &= -k_{t1}\phi_1(\psi_t) + m^{-1}e_\varphi, \\
m^{-1}\dot{e}_\varphi &= -k_{t2}\phi_2(\psi_t) + m^{-1}\dot{\varphi}_D.
\end{aligned} \tag{5.5}$$

Next, for $\mathcal{A}_t$ as defined in (5.1), $\forall\, \mathcal{Q}_t \in \mathbb{R}^{2\times 2}$ where $\mathcal{Q}_t \succ 0$, the Lyapunov equation,

$$\mathcal{A}_t^{\mathrm{T}}\mathcal{P}_t + \mathcal{P}_t\mathcal{A}_t = -\mathcal{Q}_t, \tag{5.6}$$

has a unique solution $\mathcal{P}_t$. Thereafter, define the Lyapunov function:

$$V_t = V_{t0} + \mu_t e_b^{\mathrm{T}} e_b, \text{ where } V_{t0} = \zeta_t^{\mathrm{T}}\mathcal{P}_t\zeta_t \tag{5.7}$$

and ζ_t is defined as:

$$\zeta_t = [\phi_1^{\mathrm{T}}(\psi_t),\ m^{-1}e_\varphi^{\mathrm{T}}]^{\mathrm{T}}. \tag{5.8}$$

Constrain the positive scalar μ_t in (5.7) as:

$$0 < \mu_t < k_{t3}^3 \frac{\lambda_{\min}\{\mathcal{P}_t\}\,\lambda_{\min}\{\mathcal{Q}_t\}}{\lambda_{\max}\{\mathcal{P}_t\}}. \tag{5.9}$$

From Theorem 2.3.1, (5.5) and (2.27), we find that the time-derivative of V_t satisfies:

$$\dot{V}_t \leq -\gamma_{t1}V_{t0} - \gamma_{t2}V_{t0}^{\frac{1}{p}} + 2\mu_t e_b^{\mathrm{T}} e_v, \tag{5.10}$$

where γ_{t1} and γ_{t2} are defined by:

$$\gamma_{t1} = k_{t3}\frac{\lambda_{\min}\{\mathcal{Q}_t\}}{\lambda_{\max}\{\mathcal{P}_t\}},\ \gamma_{t2} = \frac{\lambda_{\min}\{\mathcal{Q}_t\}\,\lambda_{\min}\{\mathcal{P}_t\}^{\frac{p-1}{p}}\,p}{\lambda_{\max}\{\mathcal{P}_t\}\,(3p-2)}. \tag{5.11}$$

Substituting (5.3) into (5.10), we obtain:

$$\begin{aligned}
\dot{V}_t &\leq -\gamma_{t1}V_{t0} - \gamma_{t2}V_{t0}^{\frac{1}{p}} + 2\mu_t e_b^{\mathrm{T}}\left[\psi_t - \kappa_t e_b - \kappa_t (e_b^{\mathrm{T}} e_b)^{\frac{1-p}{p}} e_b\right] \\
&\leq -\gamma_{t1}V_{t0} - \gamma_{t2}V_{t0}^{\frac{1}{p}} + 2\mu_t e_b^{\mathrm{T}}\psi_t - 2\mu_t\kappa_t e_b^{\mathrm{T}} e_b - 2\mu_t\kappa_t (e_b^{\mathrm{T}} e_b)^{\frac{1}{p}} \\
&\leq -\gamma_{t1}V_{t0} - \gamma_{t2}V_{t0}^{\frac{1}{p}} - 2\mu_t\kappa_t e_b^{\mathrm{T}} e_b - 2\mu_t\kappa_t (e_b^{\mathrm{T}} e_b)^{\frac{1}{p}} + \mu_t\psi_t^{\mathrm{T}}\psi_t + \mu_t e_b^{\mathrm{T}} e_b \\
&\leq -\left(\gamma_{t1} - \frac{\mu_t}{k_{t3}^2\lambda_{\min}\{\mathcal{P}_t\}}\right)V_{t0} - \gamma_{t2}V_{t0}^{\frac{1}{p}} \\
&\quad - (2\kappa_t - 1)\mu_t e_b^{\mathrm{T}} e_b - 2\kappa_t \mu_t^{\frac{p-1}{p}}\,\mu_t^{\frac{1}{p}}(e_b^{\mathrm{T}} e_b)^{\frac{1}{p}}.
\end{aligned} \tag{5.12}$$

Therefore, we further obtain:

$$\dot{V}_t < -\Gamma_{t1} V_t - \Gamma_{t2} V_t^{\frac{1}{p}}, \tag{5.13}$$

where

$$\begin{aligned} \Gamma_{t1} &= \min \left\{ k_{t3} \frac{\lambda_{\min}\{\mathcal{Q}_t\}}{\lambda_{\max}\{\mathcal{P}_t\}} - \frac{\mu_t}{k_{t3}^2 \lambda_{\min}\{\mathcal{P}_t\}}, 2\kappa_t - 1 \right\}, \\ \Gamma_{t2} &= \min \left\{ \frac{\lambda_{\min}\{\mathcal{Q}_t\} \lambda_{\min}\{\mathcal{P}_t\}^{\frac{p-1}{p}} p}{\lambda_{\max}\{\mathcal{P}_t\}(3p-2)}, 2\kappa_t \mu_t^{\frac{p-1}{p}} \right\}. \end{aligned} \tag{5.14}$$

Based on (5.13), we conclude that when the resultant disturbance force is constant and the ESO gains satisfy the constraints in Proposition 5.1.1, the error dynamics of the ESO (5.4) is FFTS. This concludes the proof of Theorem 5.1.1. □

5.1.2 FFTS-ESO: Rotational motion

Proposition 5.1.2 (FFTS-ESO: Rotational motion)**.** *Define $e_R = s_K(E_R)$, where $s_K(\cdot)$ is as defined by Lemma 3.3.1. Define $e_w = w(E_R, e_\Omega)$ by applying* (3.10)*. Define the positive scalar gains k_{a1} and k_{a2}, which make the matrix $\mathcal{A}_a \in \mathbb{R}^{2\times 2}$ defined as:*

$$\mathcal{A}_a = \begin{bmatrix} -k_{a1} & 1 \\ -k_{a2} & 0 \end{bmatrix}, \tag{5.15}$$

a Hurwitz matrix. The ESO designed for the rotational motion is given by:

$$
\begin{aligned}
&\dot{\widehat{R}} = \widehat{R}\widehat{\Omega}^{\times}, \\
&\dot{\widehat{\Omega}} = E_R J^{-1}\left[J(\Omega^m)\times\Omega^m + \widehat{\tau}_D + \tau\right] \\
&+ E_R J^{-1}\left[k_{a1} J\phi_1(\psi_a) + \kappa_a J(e_R^{\mathrm{T}} e_R)^{\frac{1-p}{p}} H\left(e_R, \frac{p-1}{p}\right) e_w + \kappa_a J e_w\right] + E_R e_{\Omega}^{\times} E_R^{\mathrm{T}} \widehat{\Omega}, \\
&\dot{\widehat{\tau}}_D = J k_{a2}\phi_2(\psi_a),
\end{aligned}
\tag{5.16}
$$

where ψ_a is defined as follows:

$$
\psi_a = e_{\Omega} + \kappa_a\left[e_R + (e_R^{\mathrm{T}} e_R)^{\frac{1-p}{p}} e_R\right],\ \kappa_a > \frac{1}{2}. \tag{5.17}
$$

In addition, the constant k_{a3} is defined and it occurs in the terms $\phi_1(\psi_a)$ and $\phi_2(\psi_a)$, where it takes the place of k_3 in (2.37)*.*

Theorem 5.1.2. *With the observer errors for the rotational ESO defined by* (3.13)*,* (3.14)*, the rotational kinematics and dynamics given by* (3.4)*, and the ESO for rotational motion given in Proposition 5.1.2, the error dynamics of the ESO is given by:*

$$
\begin{aligned}
\dot{E}_R &= E_R e_{\Omega}^{\times}, \\
J\dot{e}_{\Omega} &= -k_{a1} J\phi_1(\psi_a) - \kappa_a J\left[(e_R^{\mathrm{T}} e_R)^{\frac{1-p}{p}} H\Big(e_R, \frac{p-1}{p}\Big) e_w + e_w\right] + e_{\tau}, \\
\dot{e}_{\tau} &= -k_{a2} J\phi_2(\psi_a) + \dot{\tau}_D.
\end{aligned}
\tag{5.18}
$$

The error dynamics (5.18) *is almost globally FFTS at the origin $((E_R, e_{\Omega}, e_{\tau}) = (I, 0, 0))$, when the resultant disturbance torque is constant $(\dot{\tau}_D = 0)$ and the measurement uncertainties are negligible $(\nu_R = 0, \nu_{\Omega} = 0)$.*

Proof. Simplify (5.18) as:

$$\begin{aligned} \dot{\psi}_a &= -k_{a1}\phi_1(\psi_a) + J^{-1}e_\tau, \\ J^{-1}\dot{e}_\tau &= -k_{a2}\phi_2(\psi_a) + J^{-1}\dot{\tau}_D. \end{aligned} \tag{5.19}$$

Next, for $\mathcal{A}_a$ as defined in (5.15), $\forall\ \mathcal{Q}_a \in \mathbb{R}^{2\times 2}$ where $\mathcal{Q}_a \succ 0$, the Lyapunov equation:

$$\mathcal{A}_a^{\mathrm{T}}\mathcal{P}_a + \mathcal{P}_a\mathcal{A}_a = -\mathcal{Q}_a, \tag{5.20}$$

has a unique solution $\mathcal{P}_a$. Thereafter, define the Morse-Lyapunov function:

$$V_a = V_{a0} + \mu_a\langle K, I - E_R\rangle, \text{ where } V_{a0} = \zeta_a^{\mathrm{T}}\mathcal{P}_a\zeta_a, \tag{5.21}$$

μ_a is a positive scalar, and ζ_a is defined as:

$$\zeta_a = [\phi_1^{\mathrm{T}}(\psi_a),\ J^{-1}e_\tau^{\mathrm{T}}]^{\mathrm{T}}.$$

We constrain the positive scalar μ_a in (5.21) as:

$$0 < \mu_a < 2k_{a3}^3\frac{\lambda_{\min}\{\mathcal{P}_a\}\,\lambda_{\min}\{\mathcal{Q}_a\}}{\lambda_{\max}\{\mathcal{P}_a\}}. \tag{5.22}$$

From Theorem 2.3.1, (5.19) and (2.27), we find that the time-derivative of V_a satisfies:

$$\dot{V}_a \leq -\gamma_{a1}V_{a0} - \gamma_{a2}V_{a0}^{\frac{1}{p}} + \mu_a e_R^{\mathrm{T}}e_\Omega, \tag{5.23}$$

where γ_{a1} and γ_{a2} are defined by:

$$\gamma_{a1} = k_{a3}\frac{\lambda_{\min}\{\mathcal{Q}_a\}}{\lambda_{\max}\{\mathcal{P}_a\}},\ \gamma_{a2} = \frac{\lambda_{\min}\{\mathcal{Q}_a\}\lambda_{\min}\{\mathcal{P}_a\}^{\frac{p-1}{p}}p}{\lambda_{\max}\{\mathcal{P}_a\}(3p-2)}. \tag{5.24}$$

Substituting (5.17) into (5.23), we obtain:

$$\begin{aligned}
\dot{V}_a &\leq -\gamma_{a1}V_{a0} - \gamma_{a2}V_{a0}^{\frac{1}{p}} + \mu_a e_R^{\mathrm{T}}\left[\psi_a - \kappa_a e_R - \kappa_a (e_R^{\mathrm{T}} e_R)^{\frac{1-p}{p}} e_R\right] \\
&\leq -\gamma_{a1}V_{a0} - \gamma_{a2}V_{a0}^{\frac{1}{p}} + \frac{1}{2}\mu_a\left(e_R^{\mathrm{T}}e_R + \psi_a^{\mathrm{T}}\psi_a\right) - \kappa_a\mu_a\left[e_R^{\mathrm{T}}e_R + (e_R^{\mathrm{T}}e_R)^{\frac{1}{p}}\right] \\
&\leq -\left(\gamma_{a1} - \frac{\mu_a}{2k_{a3}^2\lambda_{\min}\{\mathcal{P}_a\}}\right)V_{a0} - \gamma_{a2}V_{a0}^{\frac{1}{p}} \\
&- \left(\kappa_a - \frac{1}{2}\right)\mu_a e_R^{\mathrm{T}}e_R - \kappa_a\mu_a(e_R^{\mathrm{T}}e_R)^{\frac{1}{p}}.
\end{aligned} \tag{5.25}$$

By applying Lemma 3.3.1 on (5.23), we obtain:

$$\begin{aligned}
\dot{V}_a \leq &-\left(\gamma_{a1} - \frac{\mu_a}{2k_{a3}^2\lambda_{\min}\{\mathcal{P}_a\}}\right)V_{a0} - \gamma_{a2}V_{a0}^{\frac{1}{p}} \\
&- \left(\kappa_a - \frac{1}{2}\right)\mu_a\langle K, I - E_R\rangle - \kappa_a\mu_a^{\frac{p-1}{p}}\mu_a^{\frac{1}{p}}\langle K, I - E_R\rangle^{\frac{1}{p}}.
\end{aligned} \tag{5.26}$$

After some algebra, we further obtain:

$$\dot{V}_a \leq -\Gamma_{a1}V_a - \Gamma_{a2}V_a^{\frac{1}{p}}, \tag{5.27}$$

where:

$$\begin{aligned}\Gamma_{a1} &= \min\left\{k_{a3}\frac{\lambda_{\min}\{\mathcal{Q}_a\}}{\lambda_{\max}\{\mathcal{P}_a\}} - \frac{\mu_a}{2k_{a3}^2\lambda_{\min}\{\mathcal{P}_a\}}, \kappa_a - \frac{1}{2}\right\},\\ \Gamma_{a2} &= \min\left\{\frac{\lambda_{\min}\{\mathcal{Q}_a\}\lambda_{\min}\{\mathcal{P}_a\}^{\frac{p-1}{p}}p}{\lambda_{\max}\{\mathcal{P}_a\}(3p-2)}, \kappa_a\mu_a^{\frac{p-1}{p}}\right\}.\end{aligned} \tag{5.28}$$

Considering the expression given by (5.27), the set where $\dot{V}_a = 0$ is:

$$\begin{aligned}\dot{V}_a^{-1}(0) &= \{(E_R, e_\Omega, e_\tau) : s_K(E_R) = 0, \text{and } \zeta_a = 0\}\\ &= \{(E_R, e_\Omega, e_\tau) : E_R \in C, e_\Omega = 0, \text{and } e_\tau = 0\},\end{aligned} \tag{5.29}$$

where C is as defined by (3.11), which gives the set of the critical points of the Morse function used as part of the Morse-Lyapunov function in (5.21). Using Theorem 8.4 from (Khalil, 2002), we conclude that (E_R, e_Ω, e_τ) converge to the set:

$$S = \left\{(E_R, e_\Omega, e_\tau) \in \mathrm{SO}(3) \times \mathbb{R}^3 \times \mathbb{R}^3 : E_R \in C, e_\Omega = 0, \text{and } e_\tau = 0\right\}, \tag{5.30}$$

in finite time. Based on (5.27), and Lemma 2.1.2, we conclude that when the observer gains satisfy the constraints in Proposition 5.1.2, the error dynamics (5.18) converges to the set S in finite time.

In S, the only stable equilibrium is $(I, 0, 0)$, while the other three are unstable. The resulting closed-loop system with the estimation errors gives rise to a Hölder-continuous feedback with exponent less than one $(1/2 < 1/p < 1)$, while in the limiting case of $p = 1$, the feedback system is Lipschitz-continuous. Proceeding with a topological equivalence-based analysis similar to the one by (Bohn and Sanyal, 2016), we conclude

that the equilibrium and the corresponding regions of attraction of the rotational ESO with $p \in]1,2[$ are identical to those of the corresponding Lipschitz-continuous asymptotically stable ESO with $p = 1$, and the region of attraction is almost global.

To summarize, we conclude that the error dynamics (5.18) is almost globally FFTS (AG-FFTS) at the origin $((E_R, e_\Omega, e_\tau) = (I, 0, 0))$ when the resultant disturbance torque is constant ($\dot{\tau}_D = 0$) and the observer gains are constrained according to Proposition 5.1.2. This concludes the proof of Theorem 5.1.2. $\square$

5.1.3 Discussion

Remark 5.1.1 (Almost global attraction of attitude ESO)**.** (Hamrah and Sanyal, 2022) With Remark 3.3.1, we know that the Morse function $\langle I - E_R, K \rangle, E_R \in \mathrm{SO}(3)$ has the following critical point set, which makes $e_R = s_K(E_R) = 0$, such that,

$$C \triangleq \{I, \mathrm{diag}(1,-1,-1), \mathrm{diag}(-1,1,-1), \mathrm{diag}(-1,-1,1)\} \subset \mathrm{SO}(3).$$

Thus, in Theorem 5.1.2, among the four critical points in this set, the equilibrium $(E_R, e_\Omega, e_\tau) = (I, 0, 0)$ is attractive to its neighborhood as it corresponds to the global minimum point of the Morse-Lyapunov function V_a in (5.20). C/I are unstable equilibrium points. All trajectories that do not initiate on the stable manifolds of the other three equilibrium converge to the stable equilibrium $(I, 0, 0)$ A state trajectory on a stable manifold of any of these unstable equilibrium points, such as $(\mathrm{diag}(1,-1,-1), 0, 0)$, cannot approach the state outside of a closed neighborhood containing the equilibrium. Denote the union of these stable manifolds of the unstable equilibrium as $M \subset \mathrm{SO}(3) \times \mathbb{R}^3 \times \mathbb{R}^3$ and the complement of M is dense and open in $\mathrm{SO}(3) \times \mathbb{R}^3 \times \mathbb{R}^3$. All initial conditions that are in

$SO(3) \times \mathbb{R}^3 \times \mathbb{R}^3/M$ converge to the stable equilibrium $(I, 0, 0)$, which makes its domain of attraction almost global.

Remark 5.1.2 (Disturbance robustness)**.** Similar to Remark 4.1.1, consider Corollary 2.3.1 and its constraints on differentiator gains. When the disturbance forces and torques are dynamic, then $\|\dot{\varphi}_D\|, \|\dot{\tau}_D\| > 0$. Further, if the constraints on gains in Corollary 2.3.1 are satisfied, the estimation error of the proposed FFTS-ESO is PFTS.

Remark 5.1.3 (Noise robustness)**.** Consider Corollary 2.3.2 and its constraints on differentiator gains. When the ESO measurements have noise and the constraints on gains in Corollary 2.3.2 are fulfilled, the estimation error dynamics of the proposed ESO will be PFTS. Moreover, according to Lemma 2.1.3 and Corollary 2.3.2, the η in (2.6) of Lemma 2.1.3 is a function on the level of noise in information on R, Ω, b and v and is monotonically increasing with the level of noise.

Remark 5.1.4 (Comparative analysis of noise robustness: FFTS-ESO versus the DO by (Liu et al., 2022))**.** We investigate the disturbance (forces or torques) observers proposed by (Liu et al., 2022) in their Theorems 1 and 2, known as FxTSDO. The input of FxTSDO relies on the motion signals, X_2, Y_2, which represent translational and angular velocities, and $\dot{X}_2$, $\dot{Y}_2$, which represent translational and angular accelerations, respectively. However, the high-level noise associated with the translational acceleration obtained from an accelerometer restricts its direct use in a flight control scheme. Additionally, direct measurement of angular acceleration is usually not feasible. Furthermore, if $\dot{X}_2$ and $\dot{Y}_2$ are obtained from the finite difference of X_2 and Y_2, they will have higher noise levels than X_2 and Y_2, leading to inferior disturbance estimation performance. In contrast to FxTSDO, the proposed FFTS-ESO incorporates position and attitude signals, which are zero-order

derivatives of motions with lower noise levels. Consequently, FFTS-ESO outperforms FxTSDO in terms of disturbance estimation performance, despite the theoretical fixed-time stability of FxTSDO. We show this through our numerical simulations in Section 5.4.

5.2 FFTS-ADRC

Proposition 5.2.1 (Position tracking control)**.** (Viswanathan, Sanyal, and Samiei, 2018) *Consider the translational tracking control law, given by*

$$\begin{aligned}\varphi = fR\mathbf{e}_3 = mg\mathbf{e}_3 + k_{TD}L_T\left[\psi_T + (\psi_T^{\mathrm{T}}\psi_T)^{\frac{1-p}{p}}\psi_T\right] + k_{TP}L_T\tilde{b} \\ + m\kappa_T\left[\tilde{v} + (\tilde{b}^{\mathrm{T}}\tilde{b})^{\frac{1-p}{p}}H\left(\tilde{b}, \frac{p-1}{p}\right)\tilde{v}\right] - m\dot{v}_d + \widehat{\varphi}_D,\end{aligned} \tag{5.31}$$

where ψ_T is defined by:

$$\psi_T = \tilde{v} + \kappa_T\left[\tilde{b} + (\tilde{b}^{\mathrm{T}}\tilde{b})^{\frac{1-p}{p}}\tilde{b}\right]. \tag{5.32}$$

In (5.31)*, $\widehat{\varphi}_D$ is obtained from the translational ESO in Proposition 5.1.1. In addition to the ESO gains, we define positive scalar gains κ_T, k_{TD}, k_{TP}, and a diagonal matrix $L_T \in \mathbb{R}^{3\times 3}$, given by $L_T = \mathrm{diag}(L_{T1}, L_{T2}, L_{T3})$, $L_{T1}, L_{T2}, L_{T3} > 0$.*

Theorem 5.2.1. *Consider the tracking error dynamics of the proposed ADRC in Proposition 5.2.1, as follows:*

$$\begin{aligned}
\dot{\tilde{b}} &= \tilde{v} \\
m\dot{\tilde{v}} &= e_\varphi - k_{TD}L_T\left[\psi_T + (\psi_T^{\mathrm{T}}\psi_T)^{\frac{1-p}{p}}\psi_T\right] - k_{TP}L_T\tilde{b} \\
&\quad - m\kappa_T\left[\tilde{v} + (\tilde{b}^{\mathrm{T}}\tilde{b})^{\frac{1-p}{p}} H\left(\tilde{b}, \frac{p-1}{p}\right)\tilde{v}\right],
\end{aligned} \tag{5.33}$$

where e_φ is the disturbance force rejection error, whose value is identical to the disturbance force estimation error defined by (3.12)*. The tracking error dynamics is FFTS at the origin* $(\tilde{b} = 0, \tilde{v} = 0)$*, when e_φ is a zero vector* $(e_\varphi = 0)$*.*

Proof. We simplify the tracking error dynamics (5.33) as:

$$\begin{aligned}
\dot{\tilde{b}} &= \tilde{v} \\
m\dot{\psi}_T &= e_\varphi - k_{TD}L_T\left[\psi_T + (\psi_T^{\mathrm{T}}\psi_T)^{\frac{1-p}{p}}\psi_T\right] - k_{TP}L_T\tilde{b}.
\end{aligned} \tag{5.34}$$

We consider the following Lyapunov function,

$$V_T = \frac{1}{2}m\psi_T^{\mathrm{T}}\psi_T + \frac{1}{2}k_{TP}\tilde{b}^{\mathrm{T}}\tilde{b}, \tag{5.35}$$

Afterwards, we obtain the time-derivative of (5.35),

$$
\begin{aligned}
\dot{V}_T &= m\psi_T^{\mathrm{T}}\dot{\psi}_T + k_{TP}\tilde{b}^{\mathrm{T}}\dot{\tilde{b}} \\
&\leq -k_{TD}\psi_T^{\mathrm{T}}L_T\psi_T - k_{TD}(\psi_T^{\mathrm{T}}\psi_T)^{\frac{1-p}{p}}\psi_T^{\mathrm{T}}L_T\psi_T - k_{TP}\psi_T^{\mathrm{T}}\tilde{b} + k_{TP}\tilde{b}^{\mathrm{T}}\tilde{v} \\
&\leq -k_{TD}\lambda_{\min}\{L_T\}\psi_T^{\mathrm{T}}\psi_T - k_{TD}\lambda_{\min}\{L_T\}(\psi_T^{\mathrm{T}}\psi_T)^{\frac{1}{p}} \\
&- k_{TP}\psi_T^{\mathrm{T}}\tilde{b} + k_{TP}\tilde{b}^{\mathrm{T}}\left[\psi_T - \kappa_T(\tilde{b} + (\tilde{b}^{\mathrm{T}}\tilde{b})^{\frac{1}{p}-1}\tilde{b})\right] \\
&\leq -k_{TD}\lambda_{\min}\{L_T\}\psi_T^{\mathrm{T}}\psi_T - k_{TD}\lambda_{\min}\{L_T\}(\psi_T^{\mathrm{T}}\psi_T)^{\frac{1}{p}} \\
&- \kappa_T k_{TP}(\tilde{b}^{\mathrm{T}}\tilde{b}) - \kappa_T k_{TP}(\tilde{b}^{\mathrm{T}}\tilde{b})^{\frac{1}{p}} \\
&\leq -2k_{TD}\lambda_{\min}\{L_T\}m^{-1}\left(\frac{1}{2}m\psi_T^{\mathrm{T}}\psi_T\right) - 2^{\frac{1}{p}}k_{TD}\lambda_{\min}\{L_T\}m^{-\frac{1}{p}}\left(\frac{1}{2}m\psi_T^{\mathrm{T}}\psi_T\right)^{\frac{1}{p}} \\
&- 2\kappa_T\left(\frac{1}{2}k_{TP}\tilde{b}^{\mathrm{T}}\tilde{b}\right) - \kappa_T k_{TP}^{\frac{p-1}{p}}2^{\frac{1}{p}}\left(\frac{1}{2}k_{TP}\tilde{b}^{\mathrm{T}}\tilde{b}\right)^{\frac{1}{p}}.
\end{aligned}
\tag{5.36}
$$

Thus, the following inequality is obtained to give the stability proof based on (5.36), such that,

$$
\dot{V}_T \leq -\Gamma_{T1}V_T - \Gamma_{T2}V_T^{\frac{1}{p}}, \tag{5.37}
$$

where Γ_{T1} and Γ_{T2} are given by:

$$
\Gamma_{T1} = \min\left\{\frac{2k_{TD}\lambda_{\min}\{L_T\}}{m}, 2\kappa_T\right\}, \Gamma_{T2} = \min\left\{\frac{2^{\frac{1}{p}}k_{TD}\lambda_{\min}\{L_T\}}{m^{\frac{1}{p}}}, \kappa_T k_{TP}^{\frac{p-1}{p}}2^{\frac{1}{p}}\right\}. \tag{5.38}
$$

Thus, based on the inequality (5.37), we conclude (5.33) to be FFTS at the origin $(e_b = 0, e_v = 0)$. □

Proposition 5.2.2 (Attitude tracking control)**.** (Viswanathan, Sanyal, and Samiei, 2018) *Consider the attitude tracking control law*

$$
\begin{aligned}
\tau = & -k_{AD} L_A \left[\psi_A + (\psi_A^{\mathrm{T}} \psi_A)^{\frac{1-p}{p}} \psi_A \right] - k_{AP} s_K(Q) - k_{AI} \psi_{AI} \\
& - J(Q^{\mathrm{T}} \dot{\Omega}^d - \omega^{\times} Q^{\mathrm{T}} \Omega^d) - J\Omega \times \Omega - \widehat{\tau}_D \\
& - \kappa_A J \left[w(Q,\omega) + (s_K(Q)^{\mathrm{T}} s_K(Q))^{\frac{1-p}{p}} H\left(s_K(Q), \frac{p-1}{p} \right) w(Q,\omega) \right], \\
\dot{\psi}_{AI} = & -L_A \psi_{AI} - L_A (\psi_{AI}^{\mathrm{T}} \psi_{AI})^{\frac{1}{p}-1} \psi_{AI} + \psi_A,
\end{aligned}
\tag{5.39}
$$

where ψ_{AI} is defined as an integral term initialized with $\psi_{AI}(0) = 0$. ψ_A is defined by:

$$
\psi_A = \omega + \kappa_A \left[s_K(Q) + (s_K(Q)^{\mathrm{T}} s_K(Q))^{\frac{1-p}{p}} s_K(Q) \right]. \tag{5.40}
$$

In (5.40) *$s_K(Q)$ is from Lemma 3.3.1. $w(Q,\omega)$ is defined by* (3.10)*, and $\widehat{\tau}_D$ is obtained from rotation ESO in Proposition 5.1.2, κ_A and k_{AP} are positive scalar gains and $L_A \in \mathbb{R}^{3\times 3}$ is a gain as a positive definite matrix. $L_A = \mathrm{diag}(L_{A1}, L_{A2}, L_{A3})$, where $L_{A1}, L_{A2}, L_{A3} > 0$.*

The desired attitude R^d and desired angular velocity Ω^d in Proposition 5.2.2 is generated from the desired force $fR\mathbf{e}_3$ from Proposition 5.2.1 by applying the Hopf fibration method by (Watterson and Kumar, 2019).

Theorem 5.2.2. *Consider the tracking error dynamics of the proposed ADRC in Proposition 5.2.2, as follows:*

$$
\begin{aligned}
\dot{Q} &= Q\omega^{\times} \\
J\dot{\omega} &= e_\tau - k_{AD}L_A\Big[\psi_A + (\psi_A^{\mathrm{T}}\psi_A)^{\frac{1-p}{p}}\psi_A\Big] - k_{AP}s_K(Q) - k_{AI}\psi_{AI} \\
&\quad - \kappa_A\left[w(Q,\omega) + (s_K(Q)^{\mathrm{T}}s_K(Q))^{\frac{1-p}{p}}H\Big(s_K(Q), \frac{p-1}{p}\Big)w(Q,\omega)\right] \\
\dot{\psi}_{AI} &= -L_A\psi_{AI} - L_A(\psi_{AI}^{\mathrm{T}}\psi_{AI})^{\frac{1-p}{p}}\psi_{AI} + \psi_A,\ \psi_{AI}(0) = 0.
\end{aligned}
\tag{5.41}
$$

where e_τ is the disturbance torque rejection error, whose value is identical to the disturbance torque estimation error defined in (3.14)*. The tracking error dynamics is almost-global FFTS at the origin $(Q = I, \omega = 0, \psi_{AI} = 0)$, when e_τ is a zero vector $(e_\tau = 0)$.*

Proof. We rewrite (5.41) in the following expression:

$$
\begin{aligned}
\dot{Q} &= Q\omega^{\times} \\
J\dot{\psi}_A &= e_\tau - k_{AD}L_A\Big[\psi_A + (\psi_A^{\mathrm{T}}\psi_A)^{\frac{1-p}{p}}\psi_A\Big] - k_{AP}s_K(Q) - k_{AI}\psi_{AI} \\
\dot{\psi}_{AI} &= -L_A\psi_{AI} - L_A(\psi_{AI}^{\mathrm{T}}\psi_{AI})^{\frac{1-p}{p}}\psi_{AI} + \psi_A.
\end{aligned}
\tag{5.42}
$$

Consider the following Morse-Lyapunov function:

$$
V_A = \frac{1}{2}\psi_A^{\mathrm{T}}J\psi_A + k_{AP}\langle K, I - Q\rangle + \frac{1}{2}k_{AI}\psi_{AI}^{\mathrm{T}}\psi_{AI} \tag{5.43}
$$

We then obtain the time derivative of V_A:

$$
\begin{aligned}
\dot{V}_A &= \psi_A^{\mathrm{T}} J \dot{\psi}_A + k_{AP} s_K(Q)^{\mathrm{T}} \omega + k_{AI} \psi_{AI}^{\mathrm{T}} \dot{\psi}_{AI} \\
&\leq -k_{AD} \psi_A^{\mathrm{T}} L_A \left[\psi_A + (\psi_A^{\mathrm{T}} \psi_A)^{\frac{1-p}{p}} \psi_A \right] - k_{AP} \psi_A^{\mathrm{T}} s_K(Q) - k_{AI} \psi_A^{\mathrm{T}} \psi_{AI} \\
&- k_{AP} \kappa_A s_K(Q)^{\mathrm{T}} \left[s_K(Q) + (s_K(Q)^{\mathrm{T}} s_K(Q))^{\frac{1-p}{p}} s_K(Q) \right] + k_{AP} \psi_A^{\mathrm{T}} s_K(Q) \\
&- k_{AI} \psi_{AI}^{\mathrm{T}} L_A \psi_{AI} - k_{AI} (\psi_{AI}^{\mathrm{T}} \psi_{AI})^{\frac{1-p}{p}} \psi_{AI}^{\mathrm{T}} L_A \psi_{AI} + k_{AI} \psi_{AI}^{\mathrm{T}} \psi_A \\
&\leq -k_{AD} \lambda_{\min}\{L_A\} \psi_A^{\mathrm{T}} \psi_A - k_{AD} \lambda_{\min}\{L_A\} \left(\psi_A^{\mathrm{T}} \psi_A \right)^{\frac{1}{p}} \\
&- k_{AP} \kappa_A s_K(Q)^{\mathrm{T}} s_K(Q) - k_{AP} \kappa_A \left(s_K(Q)^{\mathrm{T}} s_K(Q) \right)^{\frac{1}{p}} \\
&- k_{AI} \lambda_{\min}\{L_A\} \psi_{AI}^{\mathrm{T}} \psi_{AI} - k_{AI} \lambda_{\min}\{L_A\} (\psi_{AI}^{\mathrm{T}} \psi_{AI})^{\frac{1}{p}} \\
&\leq -\kappa_A k_{AP} \langle K, I - Q \rangle - \kappa_A k_{AP}^{\frac{p-1}{p}} \left(k_{AP} \langle K, I - Q \rangle \right)^{\frac{1}{p}} \\
&- \frac{2 k_{AD} \lambda_{\min}\{L_A\}}{\lambda_{\max}\{J\}} \left(\frac{1}{2} \psi_A^{\mathrm{T}} J \psi_A \right) - \frac{2^{\frac{1}{p}} k_{AD} \lambda_{\min}\{L_A\}}{\lambda_{\max}\{J\}^{\frac{1}{p}}} \left(\frac{1}{2} \psi_A^{\mathrm{T}} J \psi_A \right)^{\frac{1}{p}} \\
&- 2 \lambda_{\min}\{L_A\} \left(\frac{1}{2} k_{AI} \psi_{AI}^{\mathrm{T}} \psi_{AI} \right) - 2^{\frac{1}{p}} k_{AP}^{\frac{p-1}{p}} \lambda_{\min}\{L_A\} \left(\frac{1}{2} k_{AI} \psi_{AI}^{\mathrm{T}} \psi_{AI} \right)^{\frac{1}{p}}
\end{aligned}
\tag{5.44}
$$

Thus, we obtain the following inequality:

$$
\dot{V}_A \leq -\Gamma_{A1} V_A - \Gamma_{A2} V_A^{\frac{1}{p}}, \tag{5.45}
$$

where Γ_{A1} and Γ_{A2} are defined by:

$$
\begin{aligned}
\Gamma_{A1} &= \min \left\{ 2 k_{AD} \lambda_{\min}\{L_A\} \lambda_{\max}\{J\}^{-1},\ \kappa_A, 2 \lambda_{\min}\{L_A\} \right\}, \\
\Gamma_{A2} &= \min \left\{ 2^{\frac{1}{p}} k_{AD} \lambda_{\min}\{L_A\} \lambda_{\max}\{J\}^{-\frac{1}{p}},\ \kappa_A k_{AP}^{\frac{p-1}{p}},\ 2^{\frac{1}{p}} k_{AP}^{\frac{p-1}{p}} \lambda_{\min}\{L_A\} \right\}.
\end{aligned}
$$

Thus, when $e_\tau = 0$, we conclude that (5.41) is almost-global FFTS at the origin $(Q = I, \omega = 0, \psi_{AI} = 0)$. $\square$

Remark 5.2.1. With Theorem 5.1.1 and 5.1.2, we conclude that with a properly tuned FFTS-ESO, when the disturbances are time-constant, the disturbance estimation errors e_φ and e_τ converges to the origin $(e_\varphi = 0, e_\tau = 0)$ with fast finite-time stability. Thus, in Theorem 5.2.1 and 5.2.2, we apply separation principle and assume $e_\varphi = 0$ and $e_\tau = 0$.

Remark 5.2.2. We still assume the time-constant disturbances. If we do not assume e_φ and e_τ as zero vectors, to carry out the Lyapunov analysis of tracking error dynamics, we have to merge the Lyapunov analysis in Theorem 5.1.1 and 5.1.2 to Theorem 5.2.1 and 5.2.2. Despite more complexity, we still can find a proper way to carry out the Lyapunov analysis to show the fast finite-time stability of the overall tracking error dynamics. The only difference is more constraint on the control gains and ESO gains. We omit the proof for brevity.

Remark 5.2.3. We assume that $\|e_\varphi\|$ and $\|e_\tau\|$ are not zero vectors, but with upper bounded norm. With properly tuned control gains, we can find a proper way to carry out the Lyapunov analysis to show that the overall tracking error dynamics is PFTS. We omit the proof for brevity.

5.3 FFTS-ADRC: Implementation with realistic feedback

In control practice, the perfect feedback assumption is no longer reliable. The feedback either comes from the measurement from UAV or the estimation from ESO. In this section, we adopt the feedback architectures described in Section 3.5. Based on the tracking laws

given by Propositions 5.2.2 and 5.2.1, we present the implementable FFTS-ADRC schemes in measured feedback architecture and estimated feedback architecture.

Measured feedback FFTS-ADRC:

The position tracking control law for measured feedback architecture is given by:

$$\begin{aligned}\varphi = fR^m\mathbf{e}_3 = mg\mathbf{e}_3 + k_{TD}L_T\left(\psi_T^m + \|\psi_T^m\|^{\frac{2(1-p)}{p}}\psi_T^m\right) + k_{TP}L_T\widetilde{b}^m \\ + m\kappa_T\left[\widetilde{v}^m + \|\widetilde{b}^m\|^{\frac{2(1-p)}{p}}H\left(\widetilde{b}^m, \frac{p-1}{p}\right)\widetilde{v}^m\right] - m\dot{v}_d + \widehat{\varphi}_D,\end{aligned} \tag{5.46}$$

where ψ_T^m is defined by:

$$\psi_T^m = \widetilde{v}^m + \kappa_T\left[\widetilde{b}^m + \|\widetilde{b}^m\|^{\frac{2(1-p)}{p}}\widetilde{b}^m\right]. \tag{5.47}$$

The attitude tracking control law for measured feedback architecture is given by:

$$\begin{aligned}\tau = &-k_{AD}L_A\left(\psi_A^m + \|\psi_A^m\|^{\frac{2(1-p)}{p}}\psi_A^m\right) - k_{AP}s_K(Q^m) - k_{AI}\psi_{AI}^m \\ &- J\left[(Q^m)^{\mathrm{T}}\dot{\Omega}^d - (\omega^m)^{\times}(Q^m)^{\mathrm{T}}\Omega^d\right] - J(\Omega^m)\times\Omega^m - \widehat{\tau}_D \\ &- \kappa_A J\left[w(Q^m,\omega^m) + \|s_K(Q^m)\|^{\frac{2(1-p)}{p}}H\left(s_K(Q^m), \frac{p-1}{p}\right)w(Q^m,\omega^m)\right], \\ \dot{\psi}_{AI}^m = &-L_A\psi_{AI}^m - L_A\|\psi_{AI}^m\|^{\frac{2(1-p)}{p}}\psi_{AI}^m + \psi_A^m,\end{aligned} \tag{5.48}$$

where ψ_{AI}^m is defined as an integral term initialized with $\psi_{AI}^m(0) = 0$. ψ_A^m is defined as:

$$\psi_A^m = \omega^m + \kappa_A\left[s_K(Q^m) + \|s_K(Q^m)\|^{\frac{2(1-p)}{p}}s_K(Q^m)\right]. \tag{5.49}$$

Estimated feedback FFTS-ADRC:

The position tracking control law for estimated feedback architecture is given by:

$$\begin{aligned}\varphi = f\widehat{R}\mathbf{e}_3 = mg\mathbf{e}_3 + k_{TD}L_T\left(\psi_T^e + \|\psi_T^e\|^{\frac{2(1-p)}{p}}\psi_T^e\right) + k_{TP}L_T\widetilde{b}^e \\ + m\kappa_T\left[\widetilde{v}^e + \|\widetilde{b}^e\|^{\frac{2(1-p)}{p}}H\left(\widetilde{b}^e, \frac{p-1}{p}\right)\widetilde{v}^e\right] - m\dot{v}_d + \widehat{\varphi}_D,\end{aligned} \tag{5.50}$$

where ψ_T^e is defined by:

$$\psi_T^e = \widetilde{v}^e + \kappa_T\left[\widetilde{b}^e + \|\widetilde{b}^e\|^{\frac{2(1-p)}{p}}\widetilde{b}^e\right]. \tag{5.51}$$

The attitude tracking control law for estimated feedback architecture is given by:

$$\begin{aligned}\tau = &-k_{AD}L_A\left(\psi_A^e + \|\psi_A^e\|^{\frac{2(1-p)}{p}}\psi_A^e\right) - k_{AP}s_K(Q^e) - k_{AI}\psi_{AI}^e \\ &- J\left[(Q^e)^{\mathrm{T}}\dot{\Omega}^d - (\omega^e)^{\times}(Q^e)^{\mathrm{T}}\Omega^d\right] - J\widehat{\Omega}\times\widehat{\Omega} - \widehat{\tau}_D \\ &- \kappa_A J\left[w(Q^e,\omega^e) + \|s_K(Q^e)\|^{\frac{2(1-p)}{p}}H\left(s_K(Q^e), \frac{p-1}{p}\right)w(Q^e,\omega^e)\right], \\ \dot{\psi}_{AI}^e = &-L_A\psi_{AI}^e - L_A\|\psi_{AI}^e\|^{\frac{2(1-p)}{p}}\psi_{AI}^e + \psi_A^e,\end{aligned} \tag{5.52}$$

where ψ_{AI}^e is defined as an integral term initialized with $\psi_{AI}^e(0) = 0$. ψ_A^e is defined as:

$$\psi_A^e = \omega^e + \kappa_A\left[s_K(Q^e) + \|s_K(Q^e)\|^{\frac{2(1-p)}{p}}s_K(Q^e)\right]. \tag{5.53}$$

5.4 Numerical simulation: FFTS-ESO versus state-of-the-art DO & ESO

In this section, we compare the proposed FFTS-ESO with existing disturbance estimation schemes, which are LESO by (Shao et al., 2018b) and FxTSDO by (Liu et al., 2022), on their disturbance estimation performance in four different simulated flight scenarios, with and without the presence of measurement noises. The four flight scenarios correspond to four desired trajectories. The inertia and mass of the simulated rotorcraft UAV are given by (4.26). The tracking control scheme to drive the UAV to track the desired trajectories is reported in Section 5.2 without disturbance rejection terms, such that $\widehat{\tau}_D$ in (5.39) and $\widehat{\varphi}_D$ in (5.31) are fixed by $\widehat{\tau}_D = 0$ and $\widehat{\varphi}_D = 0$. We use MATLAB/Simulink with its ODE2 (Heun method) solver to conduct this set of simulations. The time step size is $h = 0.001$s and the simulated duration is $T = 30$s.

Hovering	$b_d(t) = [0,\ 0,\ -3]^{\mathrm{T}}$ (m)
Slow Swing	$b_d(t) = [10\sin(0.1\pi t),\ 0,\ -3]^{\mathrm{T}}$ (m)
Fast Swing	$b_d(t) = [5\sin(0.5\pi t),\ 0,\ -3]^{\mathrm{T}}$ (m)
High Pitch	$b_d(t) = [10\sin(0.5\pi t),\ 10\cos(0.5\pi t),\ -3]^{\mathrm{T}}$ (m)

TABLE 5.1: Flight trajectory to be tracked for the comparison between FFTS-ESO, LESO and FxTSDO

In the simulated flight, the initial conditions of the UAV of all four scenarios are as,

$$R(0) = I,\ \Omega(0) = [0,\ 0,\ 0]^{\mathrm{T}}\,\mathrm{rad/s},$$
$$b(0) = [0.01,\ 0,\ 0]^{\mathrm{T}}\,\mathrm{m},\ v(0) = [5\pi,\ 0,\ 0]^{\mathrm{T}}\,\mathrm{m/s}.$$

The four flight scenarios are four desired trajectories listed in Table 5.1. 'Hovering' is the simplest flight scenario that the aircraft is ordered to stay at a fixed position during the simulation. 'High pitch' is the most complex flight scenario that the aircraft is ordered to pitch up and track a circular trajectory. Since the norm of centripetal acceleration in 'high pitch' scenario is more than a g, the aircraft has to flip over to track the desired trajectory. This desired trajectory with high centripetal acceleration forces the aircraft experiencing the singularity point of its pose representation. The measurement noises are as listed in Table 4.1 in the form of normal distribution. In this set of numerical simulation, the trajectory is tracked by the tracking control system placed in Section 5.2 without the disturbance rejection term $\hat{\varphi}_D$ and $\hat{\tau}_D$. The disturbance force and torque in all of the four scenarios in this set of simulation are identical and they are step functions presented as follows:

$$\begin{aligned} \varphi_D(t) &= \begin{cases} [5,\ 10,\ 0]^{\mathrm{T}}\ \mathrm{N} & t < 10\ \mathrm{s} \\ [9,\ 15,\ 5]^{\mathrm{T}}\ \mathrm{N} & t \geq 10\ \mathrm{s} \end{cases}, \\ \tau_D(t) &= \begin{cases} [-0.1,\ 0.1,\ 0.1]^{\mathrm{T}}\ \mathrm{N}\cdot\mathrm{m} & t < 20\ \mathrm{s} \\ [0,\ 0,\ 0.2]^{\mathrm{T}}\ \mathrm{N}\cdot\mathrm{m} & t \geq 20\ \mathrm{s} \end{cases} \end{aligned} \tag{5.54}$$

The parameters for FFTS-ESO in these simulations are $p = 1.2, k_{t1} = 3, k_{t2} = 2, k_{t3} = 6, \kappa_t = 0.8$, $k_{a1} = 3, k_{a2} = 2, k_{a3} = 4, \kappa_a = 0.6$. The parameters for the tracking control scheme in the simulations of this section are as $p = 1.2, k_{TP} = 5, k_{TD} = 16, L_P = I, \kappa_T = 2$, $k_{AP} = 12, k_{AD} = 6, k_{AI} = 2, \kappa_A = 2, L_A = I$. The gains for FxTSDO and LESO are as described by (Liu et al., 2022) and (Shao et al., 2018b). The initial conditions of FxTSDO, LESO and FFTSESO, are identical to the pose, motion and disturbance of the UAV in the

initial time frame of the simulation.

We present the simulation results into four sets of figures. Figures 5.1 and 5.2 present the disturbance force and torque estimation errors, respectively, which are from FxTSDO, LESO and FFTSESO in the flight scenario described in Table 5.1 with noise-free measurement. Figures 5.3 and 5.4 present the disturbance estimation errors from the forementioned schemes in the identical flight trajectory with the presence of identical measurement noise described in Table 4.1.

Figure 5.1 shows the disturbance force estimation errors from the three schemes with noise-free measurements. Although the disturbance force estimation error from FxTSDO shows significant initial transient, the results from Figure 5.1 indicates that with noise-free measurement, the disturbance force estimations from these three schemes converge to the origin in all four flight scenarios. The transients at $t = 15$ s are from the step-function disturbance force φ_D, whose step time is $t = 15$ s. Figure 5.2 shows the disturbance torque estimation errors from the three schemes with noise-free measurement. In Figure 5.2, we observe that when $t = 10$ s, high transients appears in the disturbance torque estimation error from FxTSDO.

Despite the initial transients, the disturbance torque estimation errors from all three schemes converge to the origin in 'hovering' and 'slow swing' scenarios. However, in 'fast swing' and 'high pitch' scenarios, the disturbance torque estimation errors from LESO and FxTSDO diverge. As is stated in Chapter 1, since the LESO uses Euler-angle to represent attitude for disturbance torque estimation, it experiences a singularity in attitude representation when the UAV tracks the 'fast swing' and 'high pitch' trajectories. Thus, in these two scenarios, the singularity in the attitude representation destabilizes the disturbance torque estimation error of LESO.

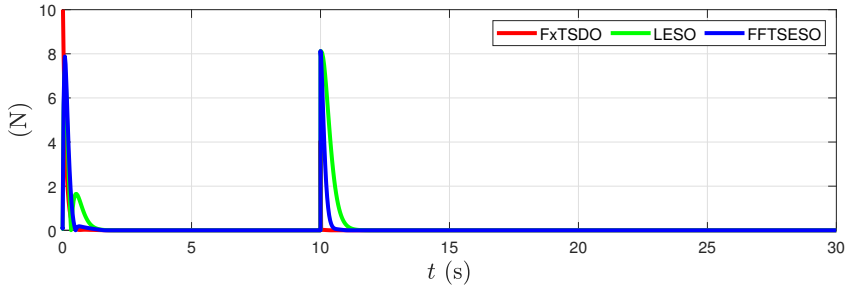

(A) Hover

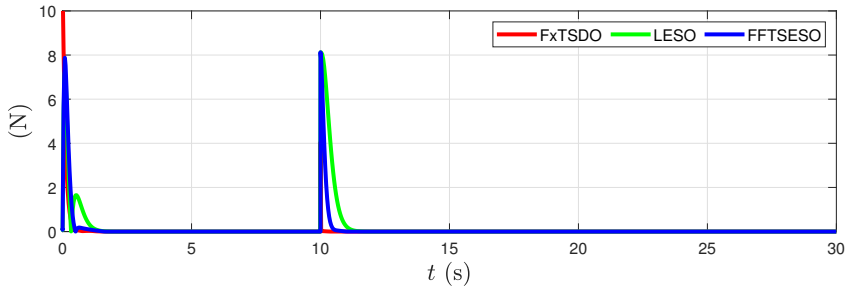

(B) Slow swing

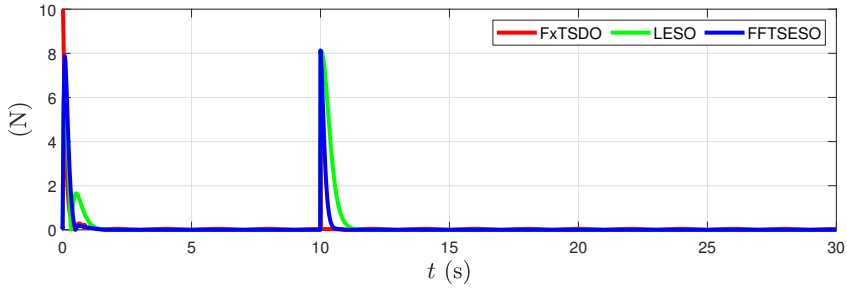

(C) Fast swing

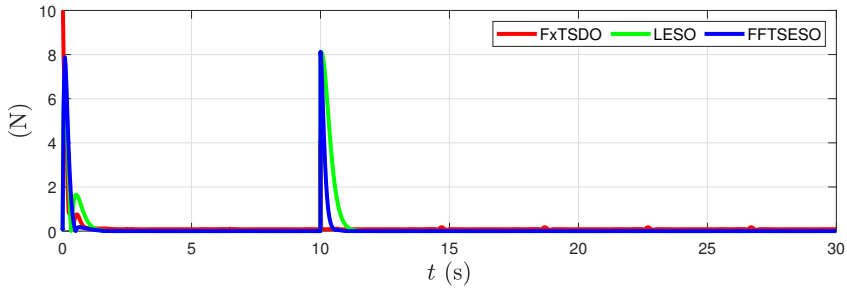

(D) High pitch

FIGURE 5.1: Disturbance force estimation errors of the multi-rotor UAV from FxTSDO, LESO, and the proposed FFTS-ESO, in different tracking control scenarios without measurement noise.

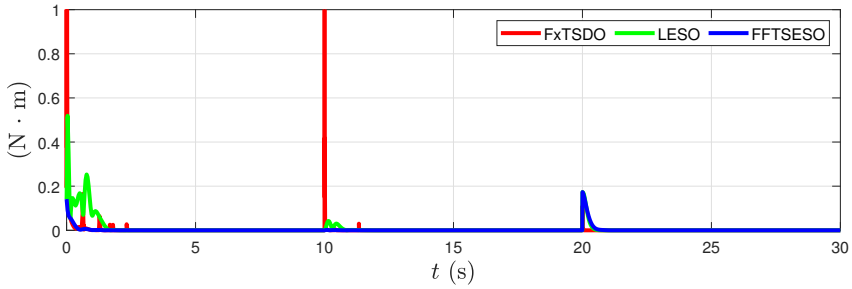

(A) Hover

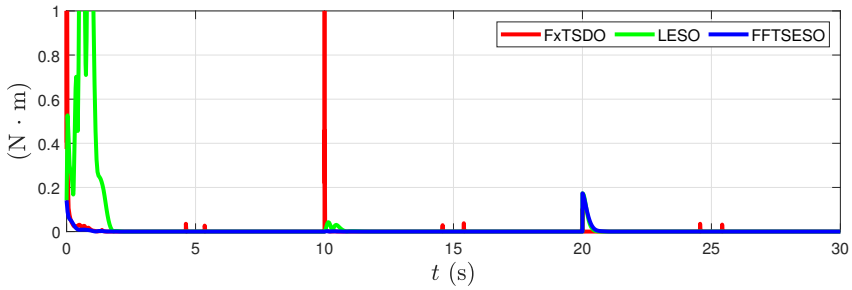

(B) Slow swing

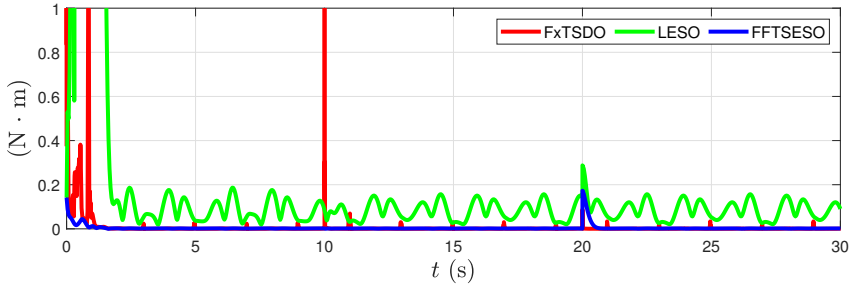

(C) Fast swing

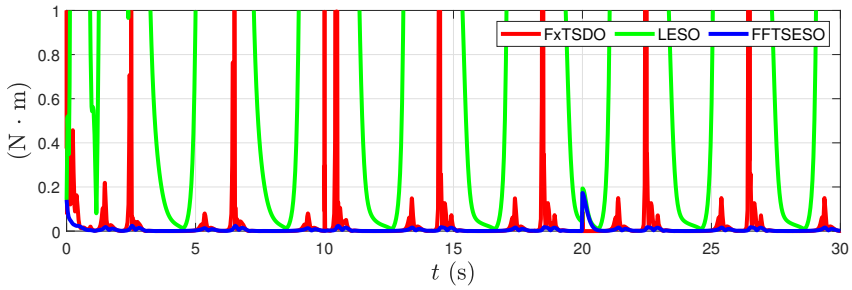

(D) High pitch

FIGURE 5.2: Disturbance torque estimation errors of the multi-rotor UAV from FxTSDO, LESO, and the proposed FFTS-ESO, in different tracking control scenario without measurement noise.

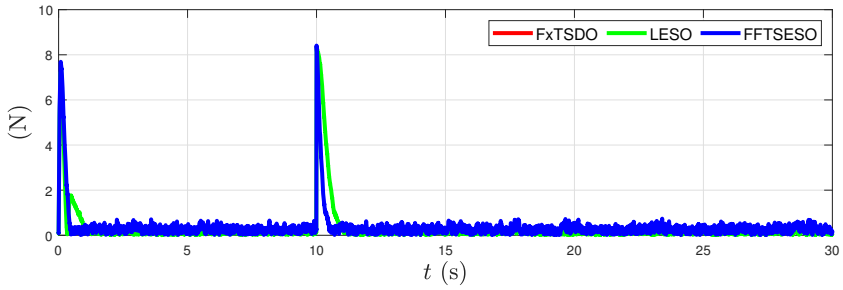

(A) Hover

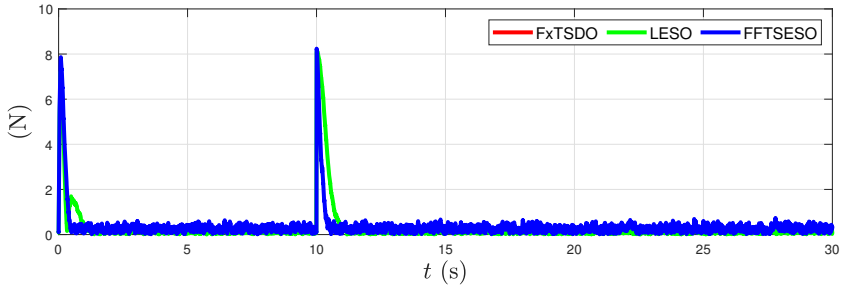

(B) Slow Swing

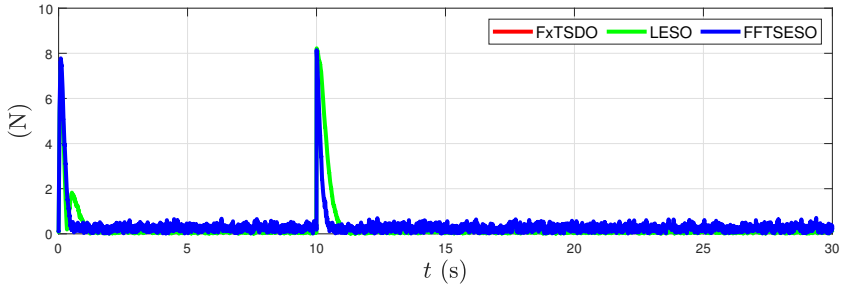

(C) Fast swing

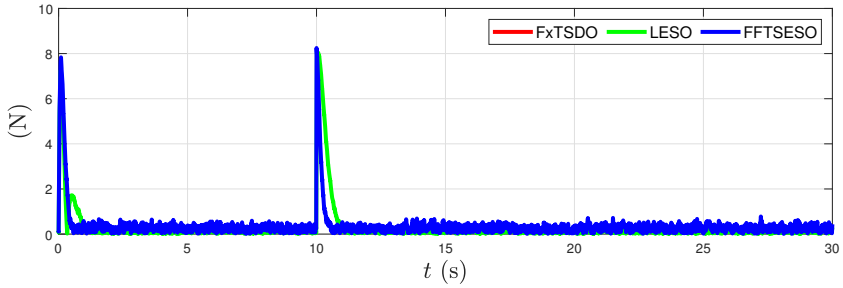

(D) High pitch

FIGURE 5.3: Disturbance force estimation error of the multi-rotor UAV from FxTSDO, LESO, and the proposed FFTS-ESO, in different tracking control scenario with measurement noise.

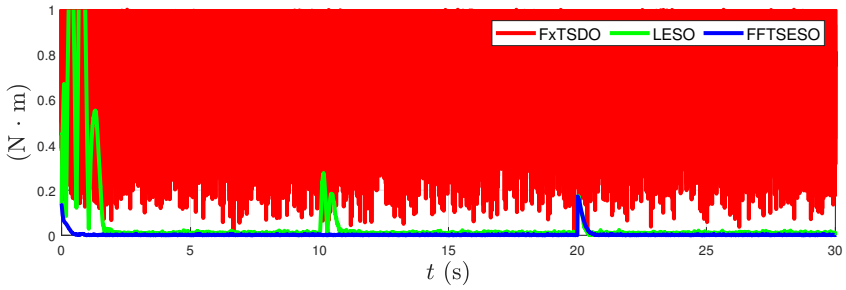

(A) Hover

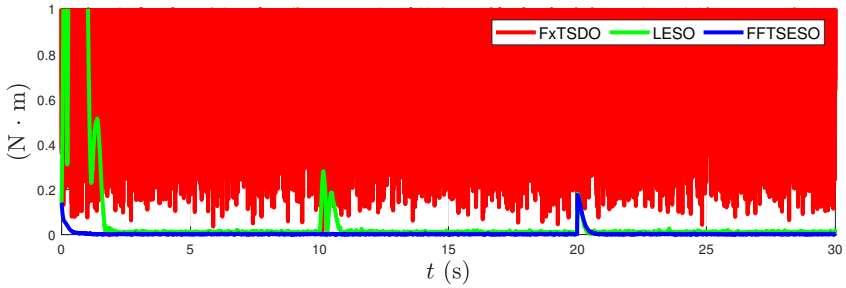

(B) Slow swing

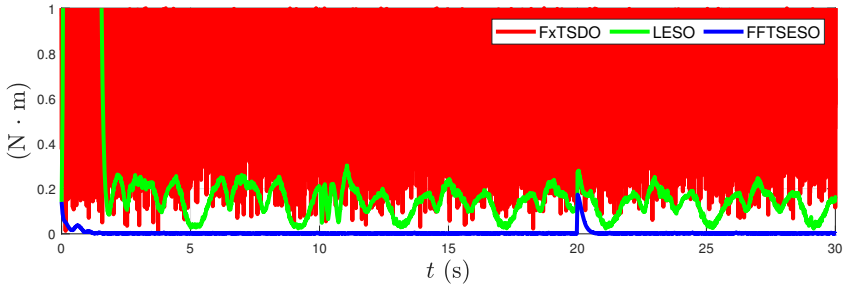

(C) Fast swing

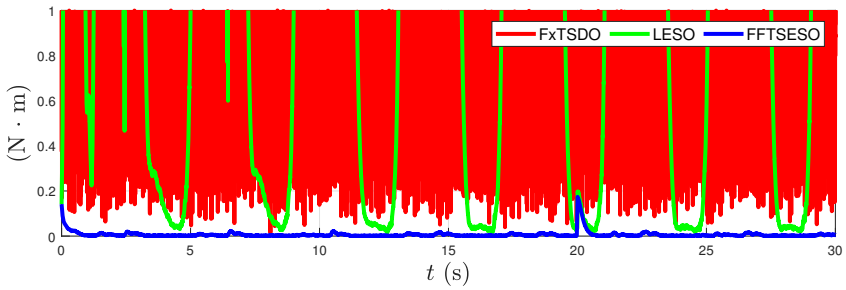

(D) High pitch

FIGURE 5.4: Disturbance torque estimation error of the multi-rotor UAV from FxTSDO, LESO, and the proposed FFTS-ESO, in different tracking control scenario with measurement noise.

Figures 5.3 and 5.4 present the disturbance force and disturbance torque estimation errors respectively, from the three schemes with identical noisy measurements as given in Table 4.1. As is stated in Remark 5.1.4, we observe that with measurement noise, FxTSDO is not capable of providing any meaningful disturbance estimation. In 'fast swing' and 'high pitch' scenarios, the disturbance torque estimation errors from LESO diverge from the origin.

To summarize, Figures 5.1, 5.2, 5.3, and 5.4 show that the FFTS-ESO has satisfactory disturbance estimation performance and outperforms the LESO and FxTSDO when the UAV experiences large pose changes and has noisy measurements.

5.5 Numerical simulation: ES-ESO versus FFTS-ESO

In this section, we present a set of numerical simulation results to validate the FFTS-ESO, and to compare with ES-ESO. In the simulations presented in this section, the settings are identical to the ones given in Section 4.4 for ES-ESO simulations, unless otherwise specified. The simulation results of ES-ESO posed in Section 4.4 are adopted here for a fair comparison. The gains of the proposed FFTS-ESO are tuned and selected as $\kappa_t = 2$, $k_{t1} = 15$, $k_{t2} = 45$ $\kappa_a = 1.5$; $k_{a1} = 15$; $k_{a2} = 54$. The gains of the exponential ESO errors e_b, e_v, $s_K(E_R)$, e_Ω are identical for both ESOs in this section, so that we can observe the effect of fraction-order ESO errors in FFTS-ESO by comparing their estimation performances.

Figures 5.5-5.8 present the simulation results. The state estimation errors e_b, e_v, E_R, e_Ω and disturbance estimation errors e_φ, e_τ are covered in the results. From the results, we observe that the FFTS-ESO outperforms ES-ESO in the comparisons of E_R, e_Ω, e_τ, e_b in every simulation. In the comparisons of e_v, e_φ, the results from FFTS-ESO have more

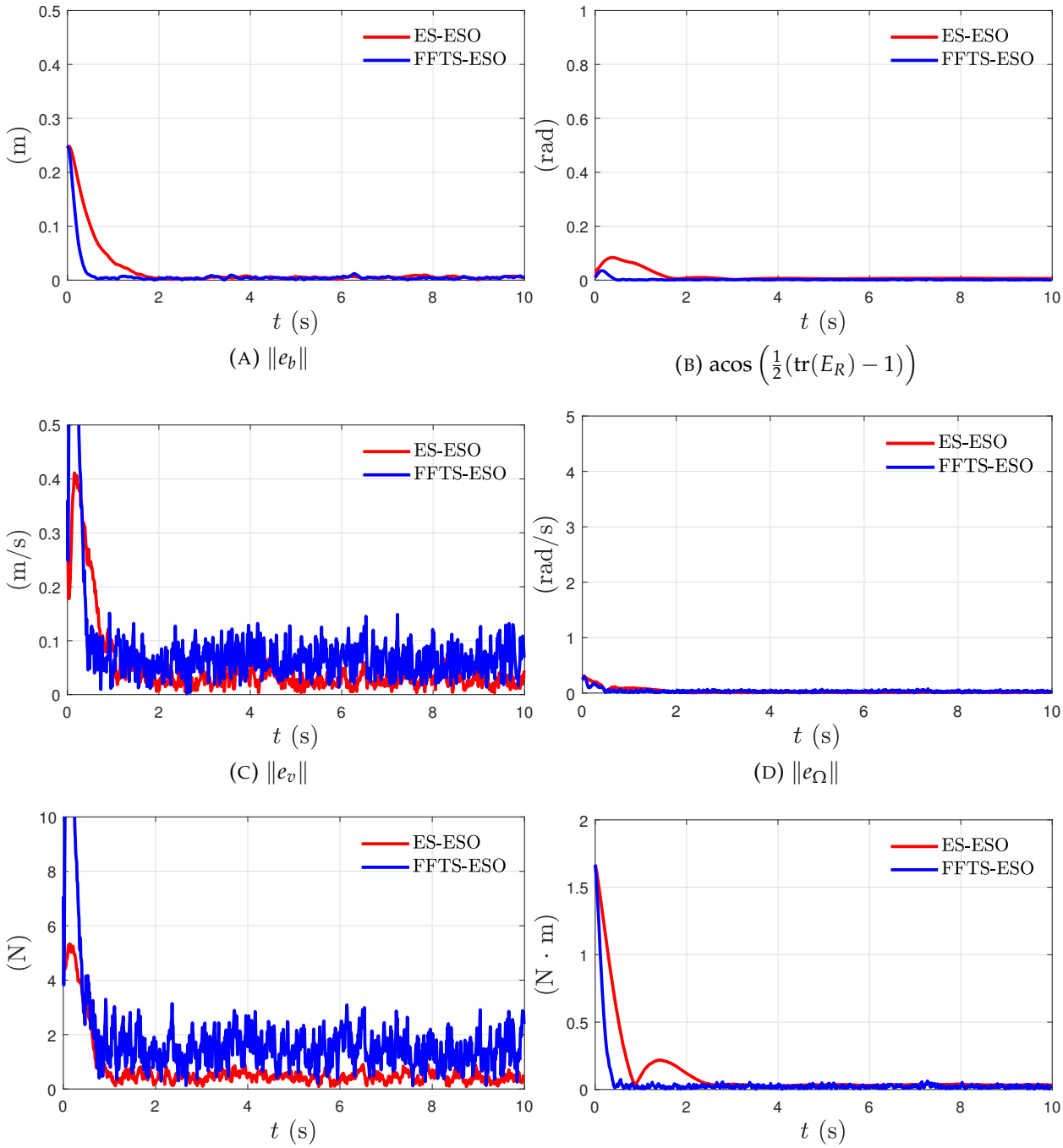

(A) $\|e_b\|$ (B) $\operatorname{acos}\left(\frac{1}{2}(\operatorname{tr}(E_R)-1)\right)$

(C) $\|e_v\|$ (D) $\|e_\Omega\|$

(E) $\|e_\varphi\|$ (F) $\|e_\tau\|$

FIGURE 5.5: ES-ESO vs FFTS-ESO: Estimation error in the simulated flight with 'circular' trajectory and constant disturbances

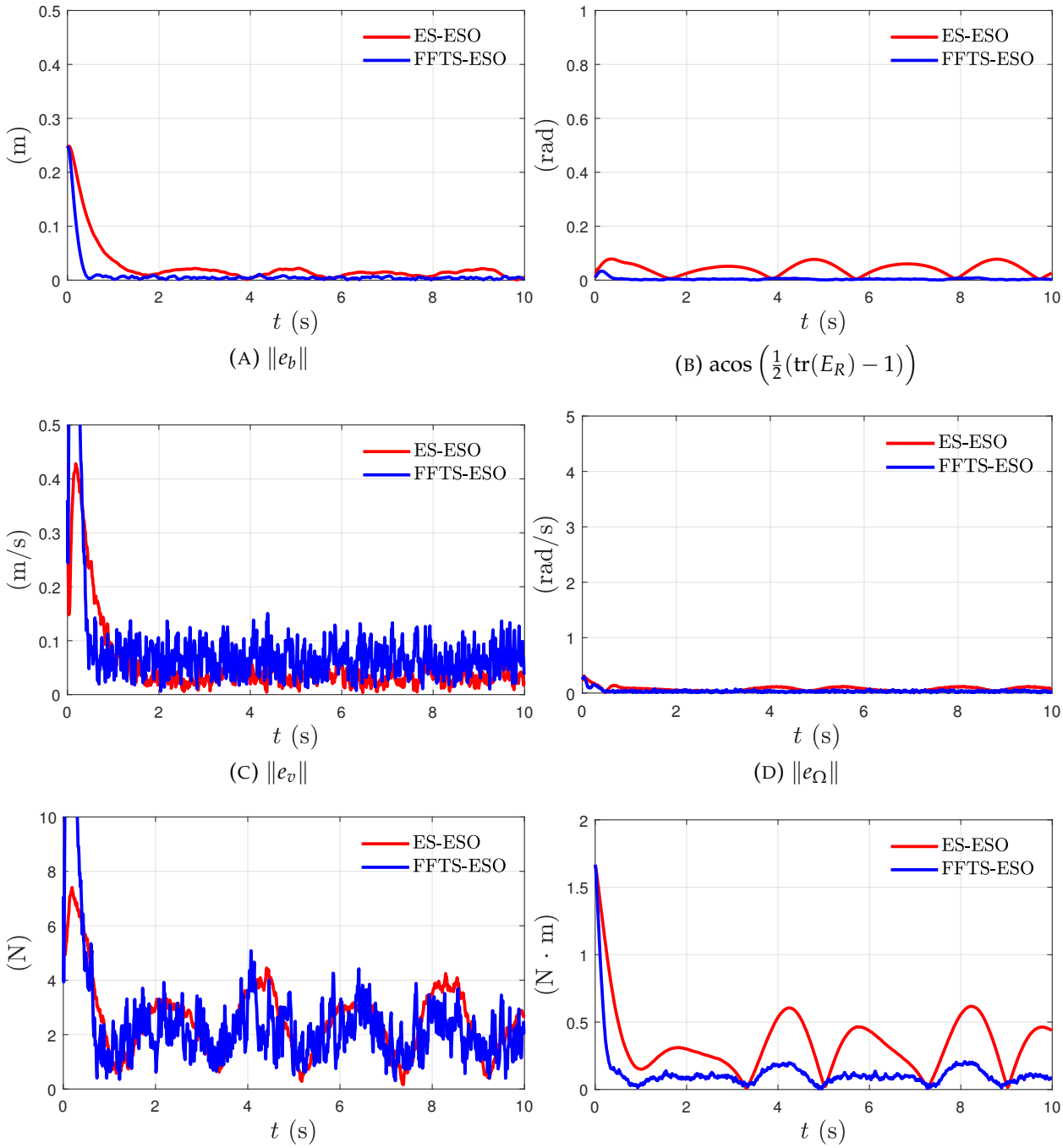

(A) $\|e_b\|$

(B) $\operatorname{acos}\left(\frac{1}{2}(\operatorname{tr}(E_R)-1)\right)$

(C) $\|e_v\|$

(D) $\|e_\Omega\|$

(E) $\|e_\varphi\|$

(F) $\|e_\tau\|$

FIGURE 5.6: ES-ESO vs FFTS-ESO: Estimation error in the simulated flight with 'circular' trajectory and dynamic disturbances

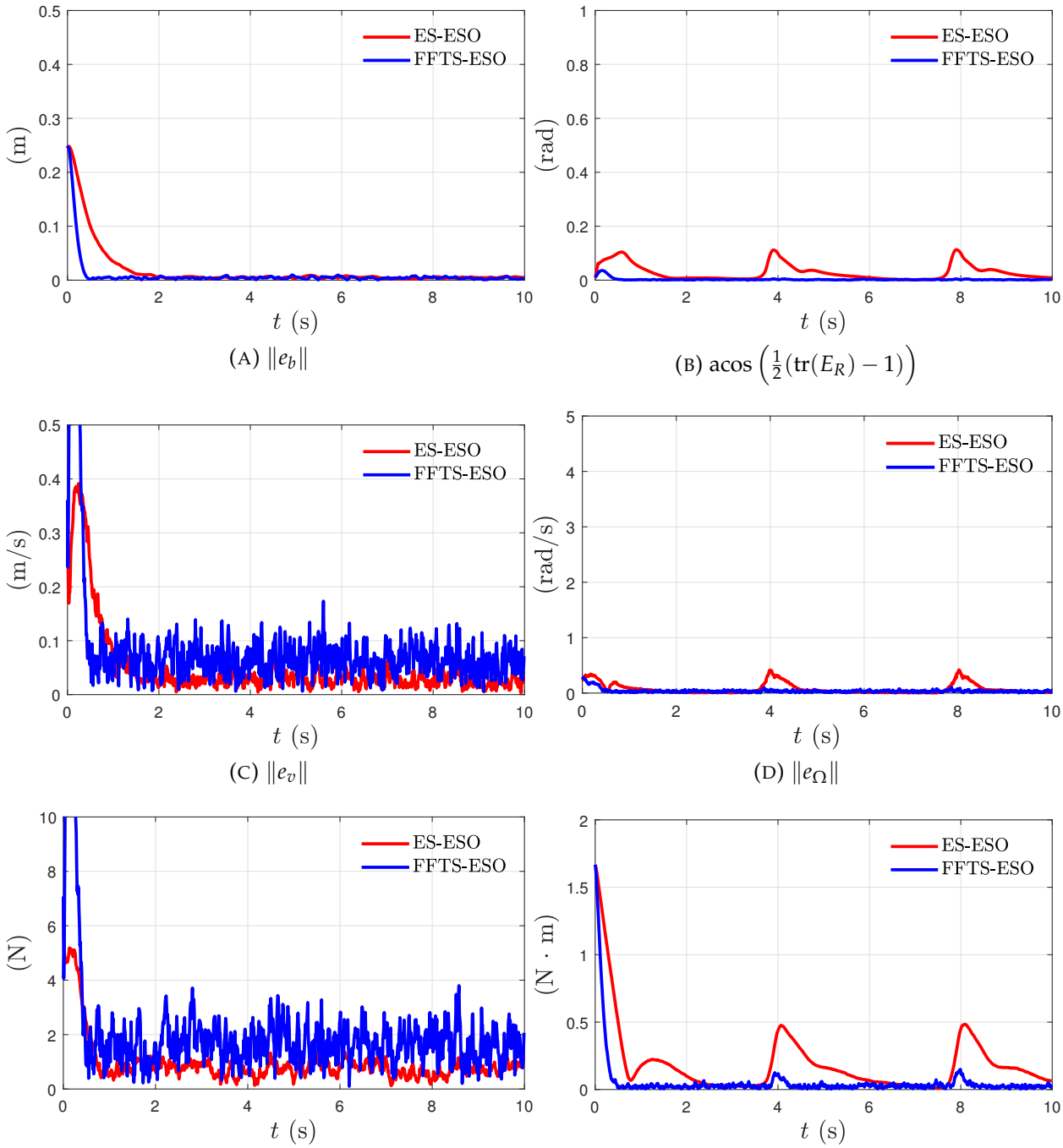

(A) $\|e_b\|$

(B) $\operatorname{acos}\left(\frac{1}{2}(\operatorname{tr}(E_R)-1)\right)$

(C) $\|e_v\|$

(D) $\|e_\Omega\|$

(E) $\|e_\varphi\|$

(F) $\|e_\tau\|$

FIGURE 5.7: ES-ESO VS FFTS-ESO: Estimation error in the simulated flight with 'barrel roll' trajectory and constant disturbances

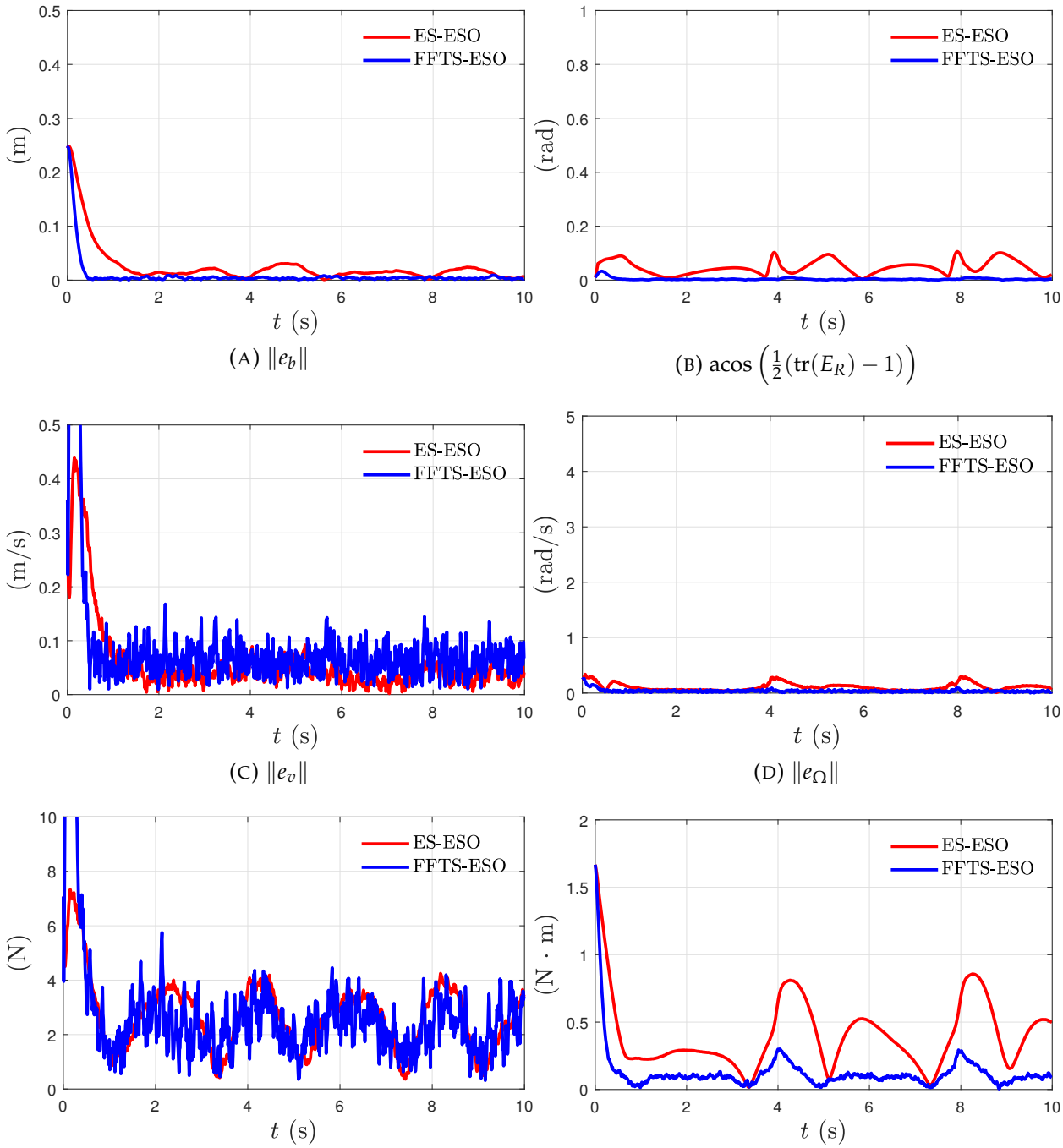

(A) $\|e_b\|$

(B) $\operatorname{acos}\left(\frac{1}{2}(\operatorname{tr}(E_R)-1)\right)$

(C) $\|e_v\|$

(D) $\|e_\Omega\|$

(E) $\|e_\varphi\|$

(F) $\|e_\tau\|$

FIGURE 5.8: ES-ESO VS FFTS-ESO: Estimation error in the simulated flight with 'barrel roll' trajectory and dynamic disturbances

fluctuations than ES-ESO in Figures 5.5-5.7, showing that the measurement noises ν_b, ν_v perturb FFTS-ESO more than ES-ESO. However, in Figure 5.8, which shows the results from the flight tracking 'barrel roll' trajectory under dynamic disturbance, we still observe that the FFTS-ESO outperforms ES-ESO in $\|e_\varphi\|$. The results posed in this section imply that the robustness against dynamic disturbances and the robustness against measurement noises are possible to be contradictory for an ESO.

To summarize, despite e_v and e_φ with higher fluctuations, FFTS-ESO shows better estimation performance than ES-ESO when the UAV experiences dynamic disturbances and complex maneuvers.

5.6 Numerical simulation: FFTS-ADRC

In this section, we present two sets of numerical simulation results on FFTS-ADRC. In the simulations presented in this section, the settings are identical to the ones given in Sections 4.2, unless otherwise specified. We command the simulated UAV to track the 'barrel roll' trajectory given by (4.28). The dynamic disturbance (4.32) perturb the simulated flight in this section The torque saturation in (4.33) is bounded by $\overline{\tau} = 100$ N·m. The first set of simulations presents the performance comparison between estimated feedback architecture and measured feedback architecture. The second set uses the estimated feedback architecture and establishes the comparison between the tracking control without disturbance rejection, with only translational rejection, with only rotational rejection, and with both rejections.

The ESO and control gains of the implemented FFTS-ADRC are selected as follows:

$$k_{t1} = 5; k_{t2} = 5; k_{t3} = 3; \kappa_t = 2; k_{TD} = 4; L_T = I; k_{TP} = 2; \kappa_T = 2,$$

$$k_{a1} = 5; k_{a2} = 6; k_{a3} = 3; \kappa_a = 1.5; k_{AD} = 3; L_A = 0.5I; k_{AP} = 3; k_{AI} = 0; \kappa_A = 2; p = 1.2.$$

5.6.1 Estimated feedback versus measured feedback

In this subsection, we present the comparison between estimated and measured feedback architectures on their tracking control performances. The control laws for measured and estimated feedback architectures are given by (5.46), (5.48), and (5.50), (5.52), respectively. Dynamic disturbance given by (4.32) perturbs the flights in the simulations. We activate both translational and rotational disturbance rejections to evaluate their performances comprehensively.

Figure 5.9 presents the tracking control performances of the two architectures. The position tracking error is defined as the norm of $\tilde{b}$. The attitude tracking error is defined by the principal angle, given by $\operatorname{acos}\left(\frac{1}{2}(\operatorname{tr}(Q) - 1)\right)$. We can clearly observe that estimated FFTS-ADRC outperforms the measured one in Figure 5.9.

Different from the comparisons between estimated feedback and measured feedback of AS-ADRC covered in Section 4.2, which is highly repeatable, the results shown in this comparison is not, due to the finite-time converging characteristics of the proposed FFTS-ADRC.

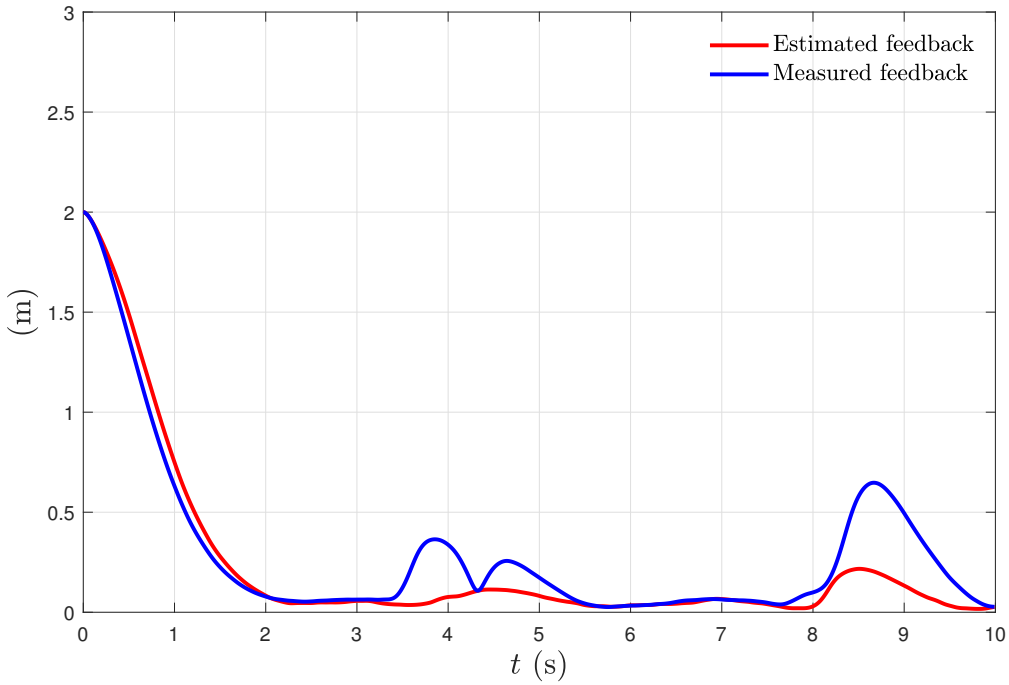

(A) $\|\tilde{b}\|$

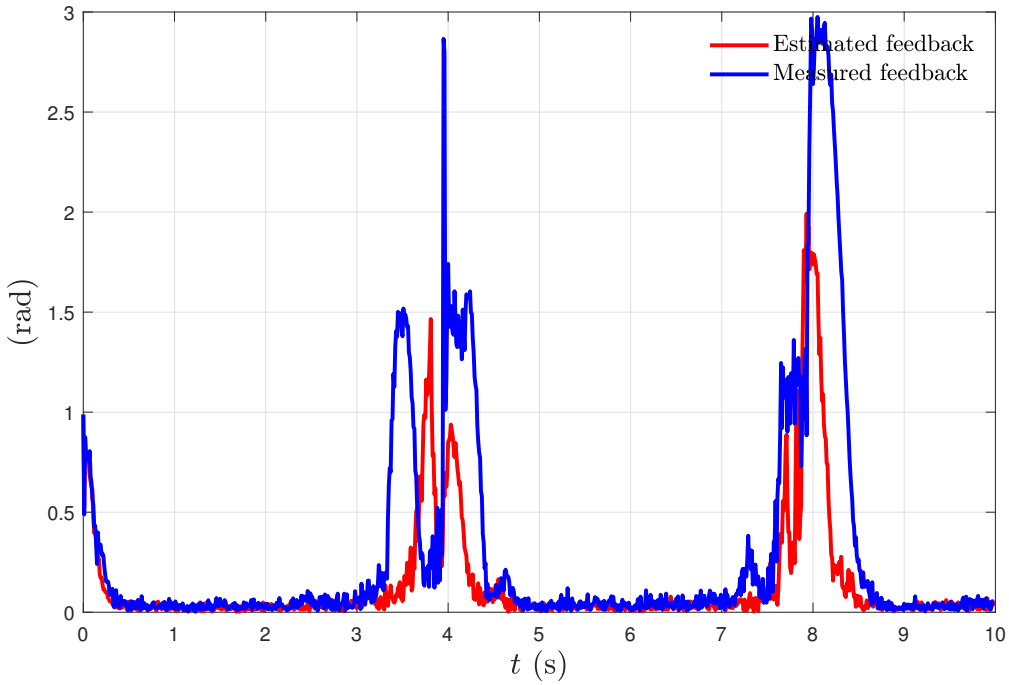

(B) acos $\left(\frac{1}{2}(\mathrm{tr}(Q)-1)\right)$

FIGURE 5.9: Estimated feedback versus measured feedback: position and attitude tracking errors of FFTS-ADRC

5.6.2 Partial rejection versus whole rejection

In this subsection, we present the simulation results with different configurations of disturbance rejection with estimated feedback architecture given by 3.21. Four simulation results, which are from the simulation without disturbance rejection, with only translational disturbance rejection, with only rotational disturbance rejection, and with both translational and rotational disturbance rejection, are included in this section to validate the control performance of the proposed FFTS-ADRC scheme. The results are presented in Figure 5.10 and Figure 5.11.

From Figure 5.10, we observe that all of the trajectories of the simulated flights converge to a neighborhood near the desired trajectory. Figure 5.11 compares the position and attitude tracking error during the simulated flights. From Figure 5.11, we can clearly observe the position tracking errors of 'both' and 'translational rejection' are much smaller than the other two. However, similar to the results posed in Section 4.5, the attitude tracking errors of the four disturbance rejection configurations cannot differ from each other significantly in Figure 5.11.

To investigate the rotational disturbance rejection configuration, we enlarge the constant disturbance torque, given by (4.34), and conduct the simulations again. Figure 5.12 presents the tracking control errors from the results.

Figure 5.12 shows the results on the attitude and position tracking error. The attitude tracking error is parameterized by the principal rotation angle of the attitude error matrix Q. The position tracking error is defined as the norm of $\tilde{b}$. Figure 5.12 indicates that the simulated flight with both translational and rotational disturbance rejection has the best control performance.

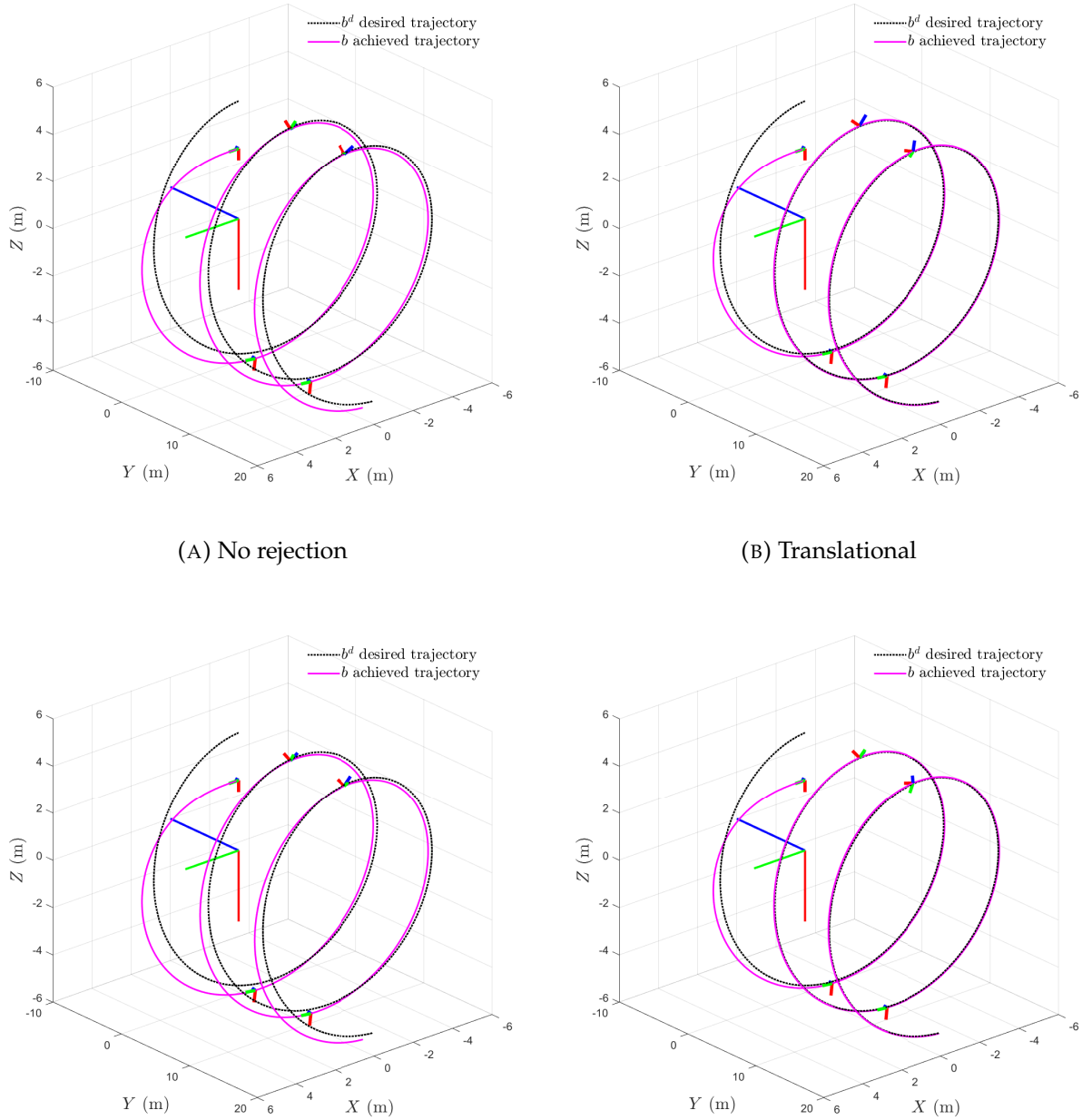

(A) No rejection

(B) Translational

(C) Rotational

(D) Both

FIGURE 5.10: The tracked trajectories of FFTS-ADRC: partial rejection versus whole rejection

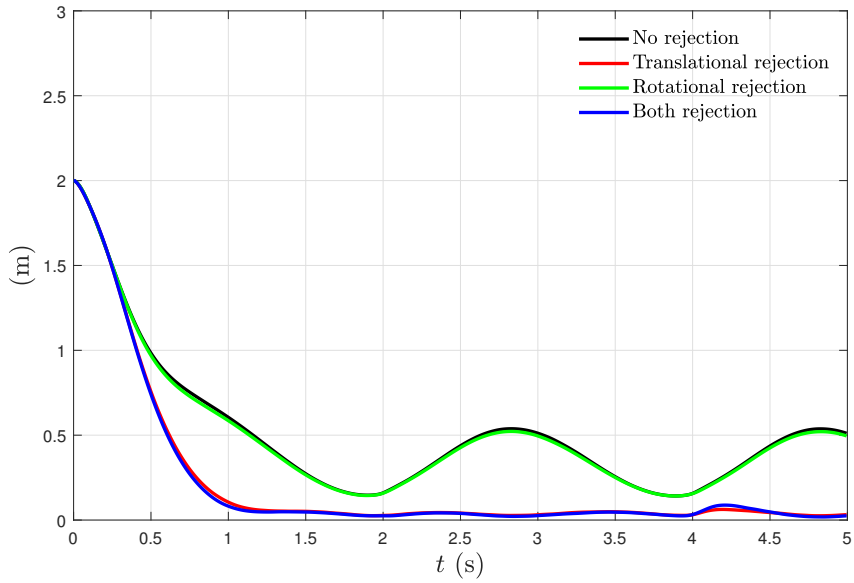

(A) $\|\tilde{b}\|$

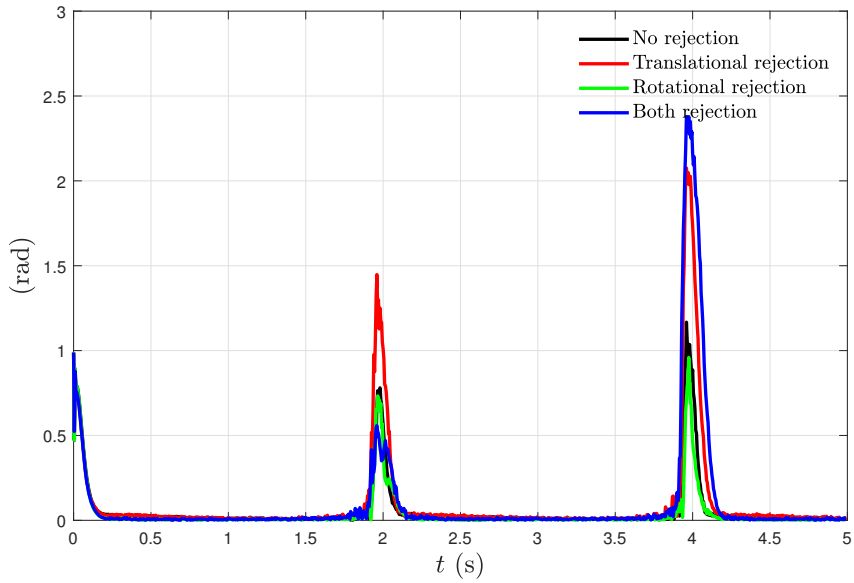

(B) $\operatorname{acos}\left(\frac{1}{2}(\operatorname{tr}(Q)-1)\right)$

FIGURE 5.11: Position and attitude tracking errors of FFTS-ADRC: partial rejection versus whole rejection

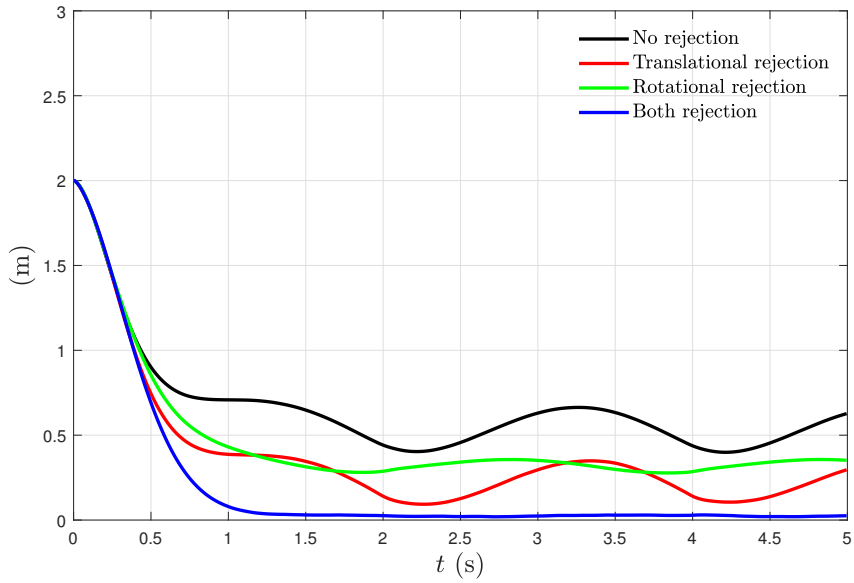

(A) $\|\tilde{b}\|$

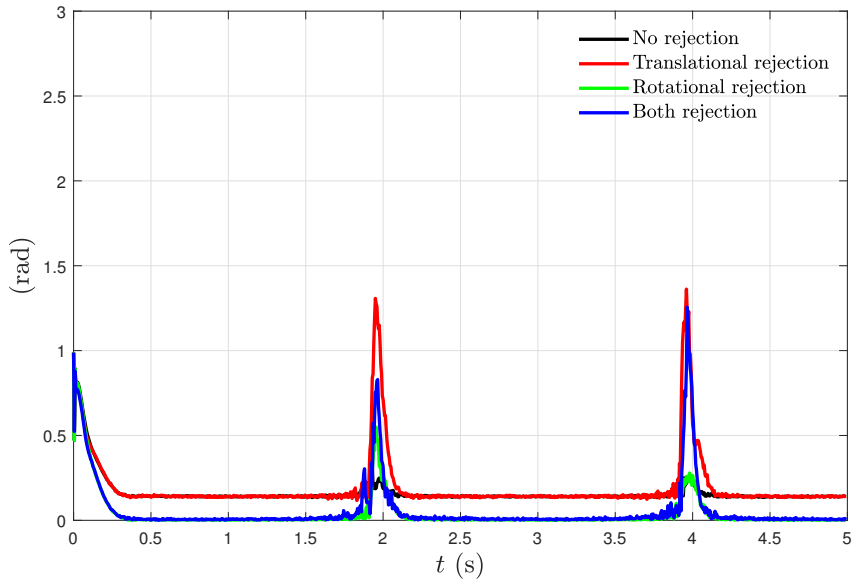

(B) $\operatorname{acos}\left(\frac{1}{2}(\operatorname{tr}(Q)-1)\right)$

FIGURE 5.12: Position and attitude tracking errors of FFTS-ADRC with amplified disturbance torque: partial rejection versus whole rejection

5.7 Summary

In this chapter, a tracking control scheme using an ESO for state feedback and disturbance rejection is designed on $\mathrm{SE}(3)$ for the rotorcraft UAV that have a body-fixed thrust direction and three-axis attitude control. The resulting ADRC scheme can enable these UAVs to perform aggressive maneuvers in the presence of aerodynamic uncertainties. The UAV system is modeled as an under-actuated system on the tangent bundle of the six-dimensional Lie group of rigid body motions, $\mathrm{SE}(3)$.

The proposed FFTS-ESO scheme is developed based on the HC-FFTSD reported in Chapter 2 to obtain fast finite-time stability with higher tunability of the settling time compared to the FTS schemes.

A tracking control scheme on $\mathrm{SE}(3)$, which utilizes the estimated disturbances from the designed ESO, is then incorporated to achieve FFTS tracking errors under constant disturbances. The Lyapunov stability analysis presented in this paper for both ESO and tracking control scheme proves the fast finite-time stability and robustness of the overall FFTS-ADRC on $\mathrm{SE}(3)$ using the proposed FFTS-ESO. We carry out the perturbation and measurement noise robustness analyses of the proposed FFTS-ESO based on the similar analyses for HC-FFTSD reported in Chapter 2.

The numerical results present the stable performance of the FFTS-ESO scheme in estimating external force and torque disturbances acting on the UAV in different scenarios. The behavior of the FFTS-ESO is compared with two state-of-the-art observers for disturbance estimation. Using a realistic set of data for several simulated flight scenarios of a rotorcraft UAV, numerical simulations show that the FFTS-ESO, unlike the LESO and FxTSDO, is always stable and its convergence is robust to measurement noise and pose singularities.

The proposed FFTS-ADRC scheme is numerically implemented by LGVI for a rotorcraft UAV model and the numerical simulations are carried out to validate the developed FFTS-ESO and FFTS-ADRC schemes. The numerical results also present the stable performance of the FFTS-ADRC when the motion of the UAV experiences the singularity point of its pose representation. The results of software-in-the-loop simulation and indoor flight experiments of the proposed FFTS-ADRC are reported in Chapters 6 and 8, respectively, to further validate the proposed FFTS-ESO and FFTS-ADRC scheme for the UAV.

Chapter 6

Rotorcraft Control Performance under Uncertain Incoming Flow: Software-In-The-Loop (SITL) Simulation Study

This chapter presents simulation results on the rotorcraft tracking control performance under uncertain incoming flow. The fast-finite time stable active disturbance rejection control (FFTS-ADRC) scheme proposed in Chapter 5 is implemented onto an open-source autopilot PX4 through its customization with measured feedback architecture. The Gazebo simulator provides a realistic simulation environment with simulated measurement noise, actuator dynamics, and uncertain incoming flows. With the FFTS-ADRC scheme implemented onto PX4, we conduct the software-in-the-loop (SITL) simulation in Gazebo to validate the flight control performance of the proposed FFTS-ADRC scheme. The simulation setup is detailed in Section 6.1. Section 6.2 covers the results. Finally, Section 6.3 provides concluding remarks of this chapter.

6.1 Simulation setup

Simulators allow PX4 flight code to control a computer modeled vehicle in a simulated "world". We can interact with the vehicle just as we might with a real vehicle, using QGroundControl, an offboard API, or a radio controller/gamepad. Gazebo is a powerful 3D simulation environment for autonomous robots that is particularly suitable for testing object-avoidance and computer vision. Gazebo can also be used with hardware-in-the-loop (HITL) and for multi-vehicle simulation. The detailed procedures to conduct an SITL simulation is available at (PX4-Dev, 2023a).

PX4 using the Simulator MAVLink API. This API defines a set of MAVLink messages that supply sensor data from the simulated world to PX4 and return motor and actuator values from the flight code that will be applied to the simulated vehicle. Figure 6.1 shows the message flow between the PX4 flight stack and the simulator.

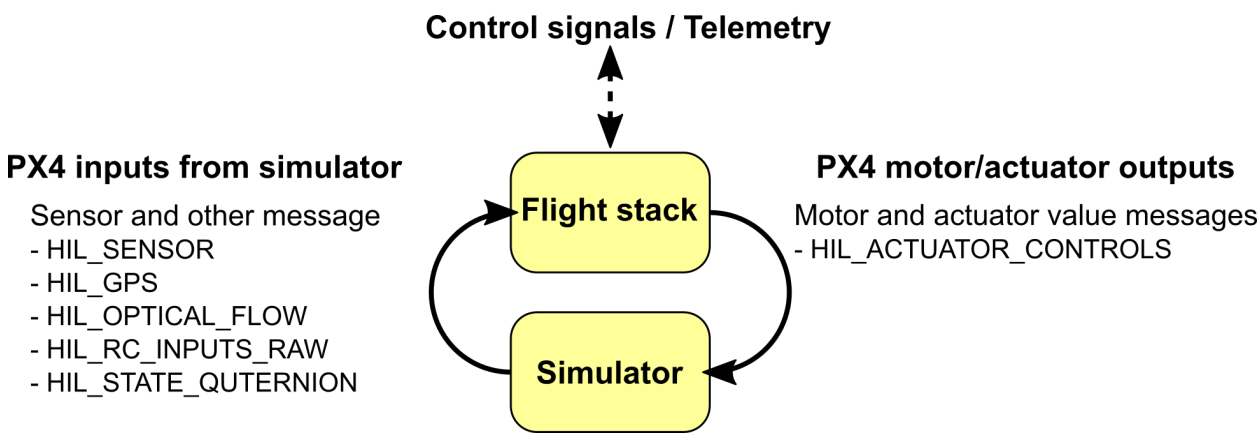

FIGURE 6.1: Data flow diagram for SITL simulation

The PX4 Gazebo plugin suite by (PX4-Dev, 2023b) is utilized to give detailed modeling of the sensors, rotors and environment. The Suite is developed based on the simulator by (Furrer et al., 2016). The propeller aerodynamic model of the Suite is based the article

by (Sydney, Smyth, and Paley, 2013). In the simulation, a simulated 3DR IRIS UAV is involved to carry out the flight mission.

The FFTS-ADRC is implemented by customizing the modules of PX4. The customization is based on PX4 stable version V1.13.2, which is published Fall 2022. The translational control scheme and the TESO are implemented onto the position control module (mc_pos_control) to replace the PID controller in the original software stack. The rotational control scheme and the RESO are implemented onto the angular rate control module (mc_rate_control) to replace the PID controller in the original software stack. The proportional control scheme in attitude control module (mc_att_control) is kept in the customized software stack to generate the desired angular velocity Ω^d.

With the simulated IRIS UAV in Gazebo with PX4, we conduct the SITL simulations for three control schemes in identical condition for comparison. The three control schemes are FFTS-ADRC, FFTS Tracking, which is the tracking control scheme reported in Chapter 5 without disturbance rejection, and the default PX4 without customization. The control implementation with measured-feadback architecture given by (5.46)-(5.48) is adopted in the SITL simulations. The FFTS Tracking and FFTS-ADRC scheme share the identical control parameters in their implementations. The only difference is the appearance of disturbance rejection.

The control parameters in the FFTS-ADRC are listed as follows:

$$k_{t1} = 12; k_{t2} = 6; k_{t3} = 2; \kappa_t = 0.5;$$

$$L_T = \text{diag}([1.0, 1.0, 2.0]); k_{TP} = 1.0; k_{TD} = 9.0; \kappa_T = 2.0,$$

$$k_{a1} = 16; k_{a2} = 6; k_{a3} = 1.2; \kappa_a = 0.8;$$

$$L_A = \text{diag}([1.0, 1.0, 2.0]); k_{AP} = 5; k_{AI} = 1; k_{AD} = 7; \kappa_A = 2; p = 1.2.$$

The inertia information of the simulated IRIS UAV is listed as follows:

$$J = \mathrm{diag}([0.0291, 0.0291, 0.0552])\ \mathrm{kg} \cdot \mathrm{m}^2, \quad m = 1.5\ \mathrm{kg}.$$

The customized PX4 with FFTS-ADRC is available at the following repository by (Wang, 2023).

During the simulation, the UAV is ordered to hover within the simulated wind field with fluctuating wind velocity u_i, which is defined by the sum of time-averaged component $\overline{U}_i$ and the fluctuating component u'. We obtain the following expression

$$u_i = U_i + u_i',$$

which will be re-stated in Chapter 7. The fluctuating component is defined by its variance during the simulation, such that $\overline{(u_i')^2}$. To clarify, this simulated wind field by Gazebo is not a serious result from computational fluid dynamics (CFD). The simulated wind field can only generate the wind field with uncertainty in the statistical form. We expose the UAV within such wind field to investigate the response of the entire UAV system experiencing the disturbance from the time-varying wind field with uncertainty. In the simulation covered in this section, $U_i = 7\ \mathrm{m/s}$, $\overline{u_i'^2} = 1\mathrm{m}^2/\mathrm{s}^2$

The time for hovering is 3 minutes. In the 3-minute simulation, we randomly extract the results from a 1-minute period in order to evaluate the control performance. The results are investigated in the following section.

6.2 Results

We present the SITL simulation results in this section. Figure 6.2 shows the simulation interface and environment.

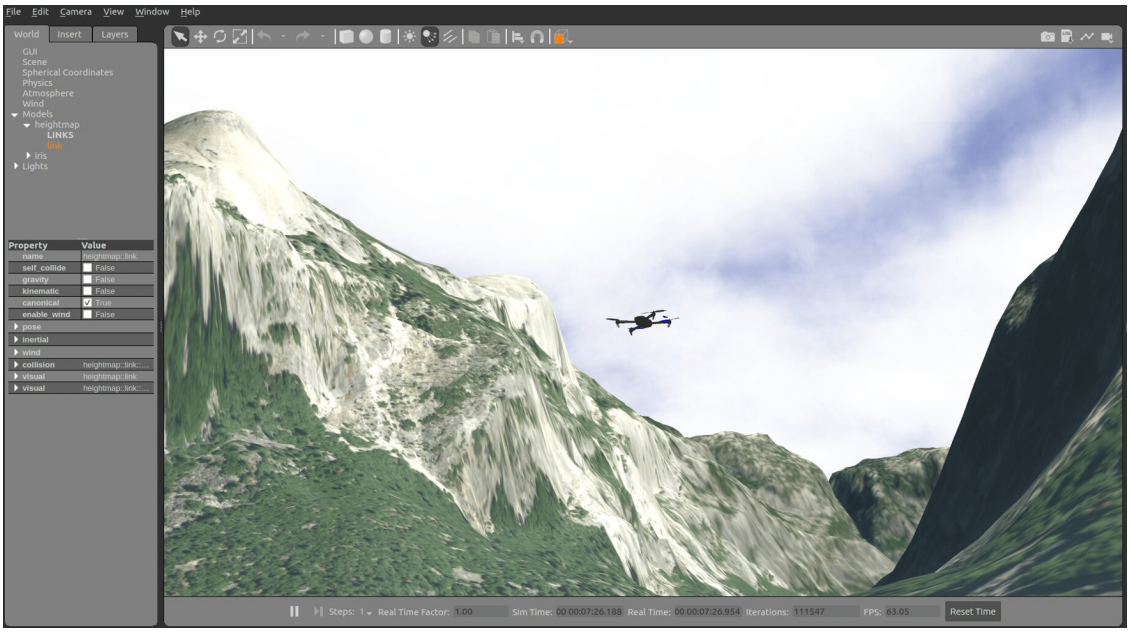

FIGURE 6.2: Simulated flight in Yosemite with Gazebo

Figures 6.3 and 6.4 show the time profiles for attitude and position tracking errors, respectively. The time profiles of the attitude tracking error for each tracking control scheme are plotted and compared in Figure 6.3. The attitude tracking error is parameterized by the principal rotation angle $\Phi = \operatorname{acos}\left(\frac{1}{2}(\operatorname{tr}(Q) - 1)\right)$. We calculate and itemize the time-averaged value of Φ as follows:

- Default PX4: 0.0371 rad,
- FFTS-Tracking: 0.0503 rad,
- FFTS-ADRC: 0.0862 rad.

Figure 6.4 presents the position tracking errors. We calculate and itemize the time-averaged value of $\|\tilde{b}\|$ as follows:

- Default PX4: 0.3370 m,
- FFTS-Tracking: 0.3053 m,
- FFTS-ADRC: 0.2134 m.

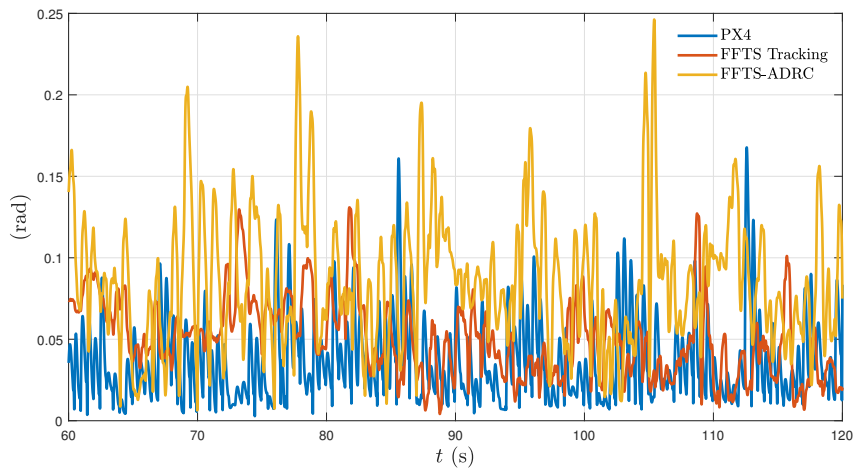

FIGURE 6.3: Comparison of the attitude tracking errors in SITL simulations

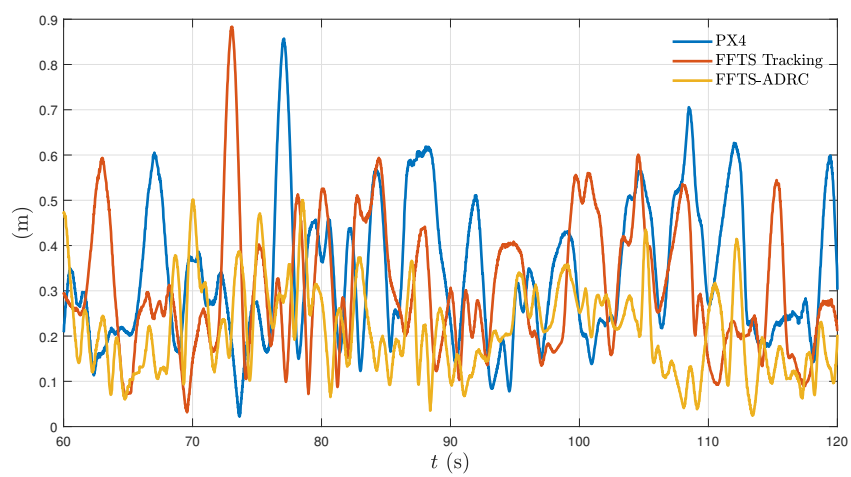

FIGURE 6.4: Comparison of the position tracking error in SITL simulations

In the result, FFTS-ADRC has the worst attitude tracking control performance but the best position tracking control performance. The results might contradict the common sense in the first glance. We provide an explanation here for reference. The FFTS-ADRC has the worst attitude tracking performance because the translational control module of the FFTS-ADRC excite the desired attitude and angular velocity more fiercely than the other two schemes. Thus, despite the worst attitude tracking performance under disturbance, FFTS-ADRC has the best position tracking control performance. We attach the hovering flight trajectories from the simulation results of the three control schemes in Figures 6.5-6.7.

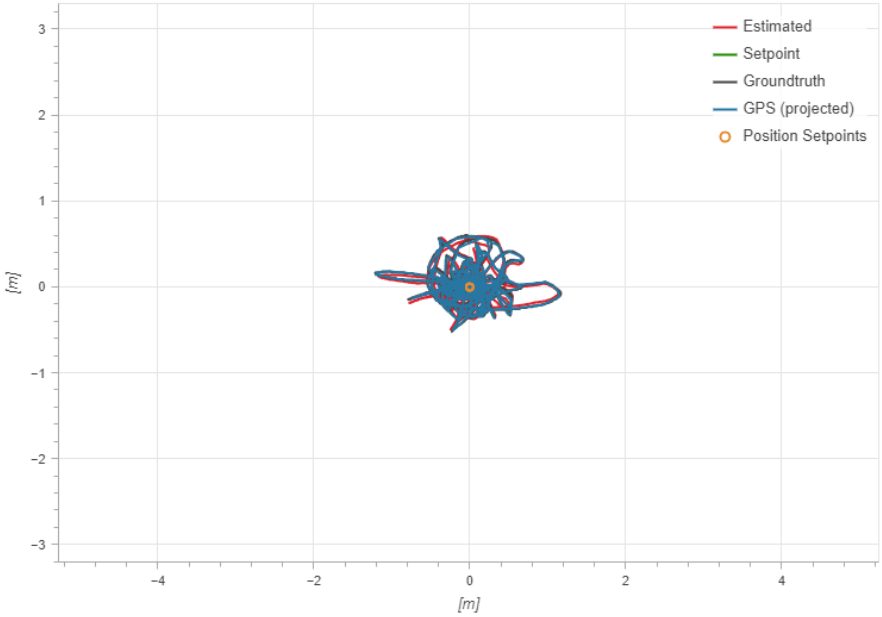

FIGURE 6.5: Flight trajectory of default PX4

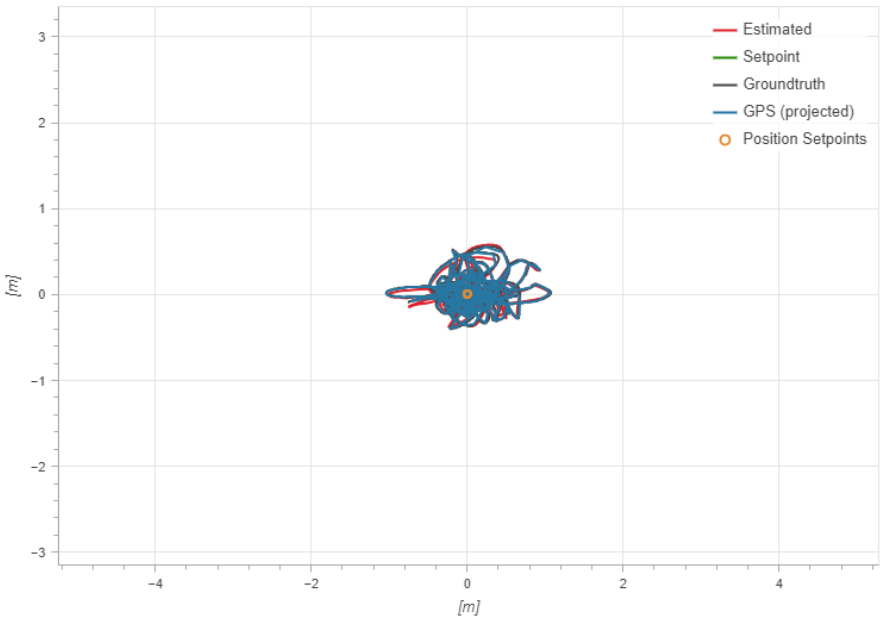

FIGURE 6.6: Flight trajectory of FFTS tracking

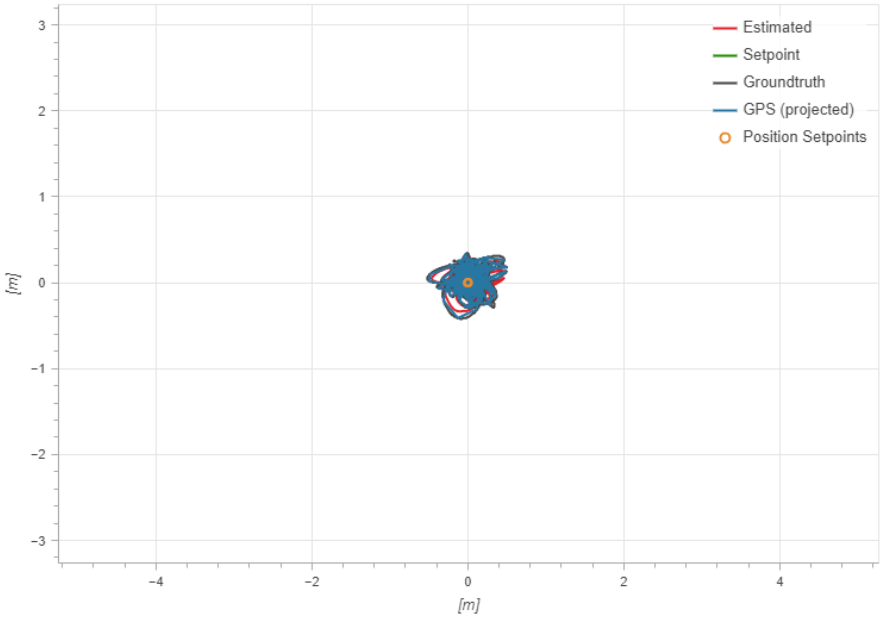

FIGURE 6.7: Flight trajectory of FFTS-ADRC

6.3 Summary

We present the result of the SITL simulation with the Gazebo simulator and open-source autopilot PX4. The autopilot PX4 is customized to implement the FFTS-ADRC scheme, presented in Chapter 5. The simulated UAV is ordered to hover within a dynamic wind field with uncertainty. We conduct the SITL simulations for three control schemes in identical conditions for comparison. The results validate the proposed FFTS-ADRC and show satisfying position tracking control performance.

Chapter 7

Experiment 1: Turbulence Characteristics of Fan Array Wind Tunnel (FAWT)

As is covered in Chapter 1, in this dissertation, we try to improve the flight control reliability of the rotorcraft UAV within the atmospheric turbulence using disturbance rejection control schemes. Technically, we have to fly the UAV in an outdoor environment to expose the UAV to the atmospheric turbulence. However, the characteristics of atmospheric turbulence are hardly accessible and highly unrepeatable if we fly the UAV outdoors.

To obtain the flight control performance within a controllable and measurable turbulent environment, (Bangura and Mahony, 2017; Bisheban and Lee, 2018, 2020; Jeon et al., 2020; Jia et al., 2022a,b; Moeini, Lynch, and Zhao, 2021a; Wang et al., 2019) conduct their flight experiments in indoor environments with box fans. As an improvement of the forementioned setups, the FAWT provides us with highly controllable, measurable, and, most importantly, repeatable turbulent incoming flows with a wide test section area in an indoor environment to imitate the outdoor atmospheric turbulence. In this dissertation, we utilize an FAWT to generate such turbulent incoming flows for flight tests.

This chapter presents the turbulence measurements from the FAWT in different working conditions. The flight control experiments covered in Chapter 8 are conducted within

the flows analyzed in this chapter. With the collected characteristics of the turbulent incoming flows, we are able to find the impact of turbulence on the flight control performance of a rotorcraft UAV within the imitated atmospheric turbulence.

The reminder of this chapter is organized as follows. Section 7.1 describes the FAWT setup and the experimental space briefly. Section 7.2 covers the measurement setup for pressure-tube and hot-wire measurements. Section 7.3 covers the analytical tools used in this chapter. The results of experiments are reported in Section 7.4 and 7.5. We conclude this chapter in Section 7.7.

7.1 Experimental setup: FAWT

The FAWT is a multi-source wind tunnel capable of generating a host of spatiotemporally-varying flow fields through software interfacing, offering a versatile, configurable alternative to traditional wind tunnel design and testing. By utilizing an array of DC-powered off-the-shelf fans (in place of one singular drive section), greater flow control capability and decreased mixing lengths are achieved. The open-loop design of FAWT provides a substantially large accessible test section area for the flight test (Dougherty, 2022).

We conduct the experiments in the Autonomous Unmanned Systems Lab (AUSL) in the Center of Excellence (CoE), Syracuse University. The FAWT is from the Switzerland-based company *WindShape. Corp.*.

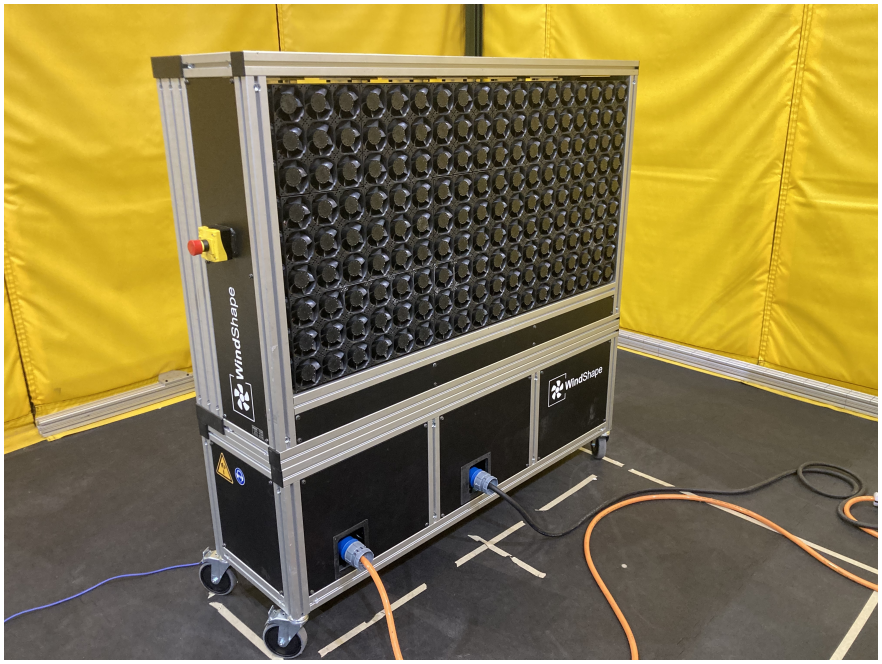

FIGURE 7.1: The FAWT in Center of Excellence (CoE), Syracuse University

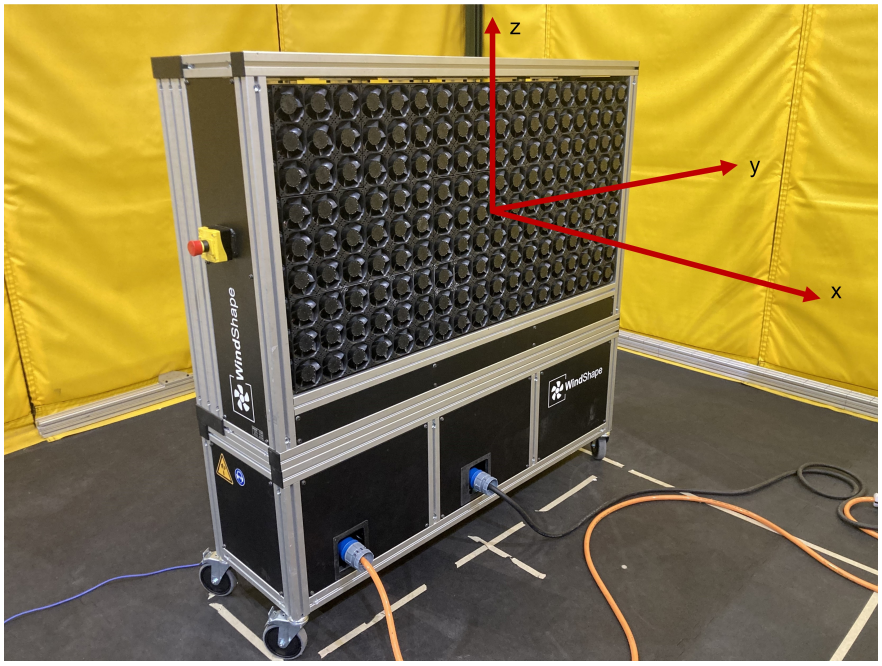

FIGURE 7.2: The coordinate system for measurement

The setup for coordinate system is identical to the one by (Dougherty, 2022). As is shown in Figure 7.2, we describe the coordinate system measurement space for the FAWT in CoE as follows.

- x direction, streamwise direction
- y direction, spanwise direction
- z direction, vertical up direction
- O, geometric center of fan-array matrix

The most basic building block of a fan array wind tunnel is the source fan unit, typically described by its outer dimension, d. The height of the fan-array is noted h. The width of the fan-array is noted as L. For the conducted experiment with the FAWT at CoE, $d = 0.08$ m, $L = 1.44$ m and $h = 0.72$ m.

7.2 Experimental setup: measurement system

7.2.1 Pressure measurement

The pressure measurement is conducted at the motion platform made of 8020 aluminum frames, which are presented in Figure 7.3. We use a set of pressure tubes to collect the dynamic pressure of the incoming flows. These pressure tubes are connected to the pressure scanner to collect the pressure data in real time. The type of pressure scanner is DSA 3217 by *Scanivalve LTD* . This type of pressure scanner has 16 piezoelectric pressure sensors, which can resolve frequency domain measurements. The pressure measurement is acquired at 625Hz from the pressure scanner. Each collection acquires 37500 points of

time-series data. The pressure data is output in engineering units via Ethernet cable using TCP/IP protocol. A desktop computer is connected with the scanner to collect the data.

To give the calibration for the space of flight to be utilized in Chapter 8, we set the measurement space of the dynamic pressure as $1\text{m} < x < 2\text{m}$, $0\text{m} < y < 0.7\text{m}$, $z = 0\text{m}$. The pressure tubes are moved around the measurement space on the motion platform to collect the data in different locations.

We acquire the local, real time atmospheric pressure through weather forecast online. Additionally, we acquire the indoor temperature and moisture through a thermometer placed within the lab. With the fore-mentioned information, we obtain the wet air density in the lab, and afterwards, obtain the wind velocities from the acquired dynamic pressures by Bernoulli equation. This pressure measurement system is also used in the hot-wire calibration which is covered in the following sub-section.

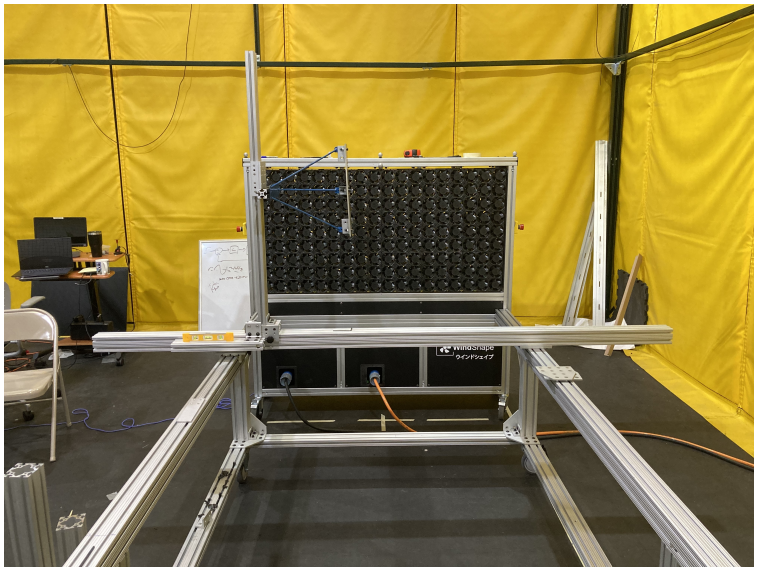

(A)

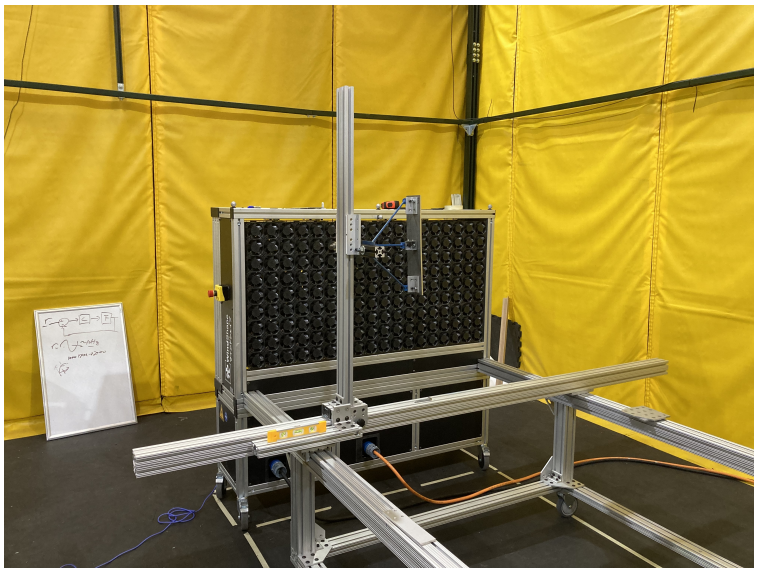

(B)

FIGURE 7.3: The spatial motion platform for pressure measurement

FIGURE 7.4: DSA3217 Pressure scanner system
Source:Scanivalve LTD.

7.2.2 Hot-wire measurement

With the capability to resolve the velocity change faster than 40kHz, hot-wire anemometer is widely used in various types of incompressible and compressible turbulent flow measurements. The hot-wire system used in this research is tungsten-wire type probe powered by constant temperature anemometer (CTA) of type AN 1003 from A.A Lab, shown in Figure 7.6. The wiring between the probe and the CTA is done carefully with insulation. The cut-off frequency for the low pass filter in CTA is set to be 3.3kHz. To collect the voltage from CTA, The CTA is connected to the data acquisition system of type NI 9234 from National Instrument, as shown in Figure 7.7. The data acquisition system collect the voltage data from CTA at 10 kHz and send the data to Labview program for

storage. The hot-wire probe is attached to the transverse system together with the pressure tube system, as shown in Figure 7.5. The hot-wire probe and the pressure tube are fixed at $x = 1.2$ m, $z = 0$ m, $y \approx 0$ m. The y coordinate difference between the hot-wire probe and pressure tube is smaller than 0.05 m. The pressure measurement is acquired at 625Hz from the pressure scanner described previously.

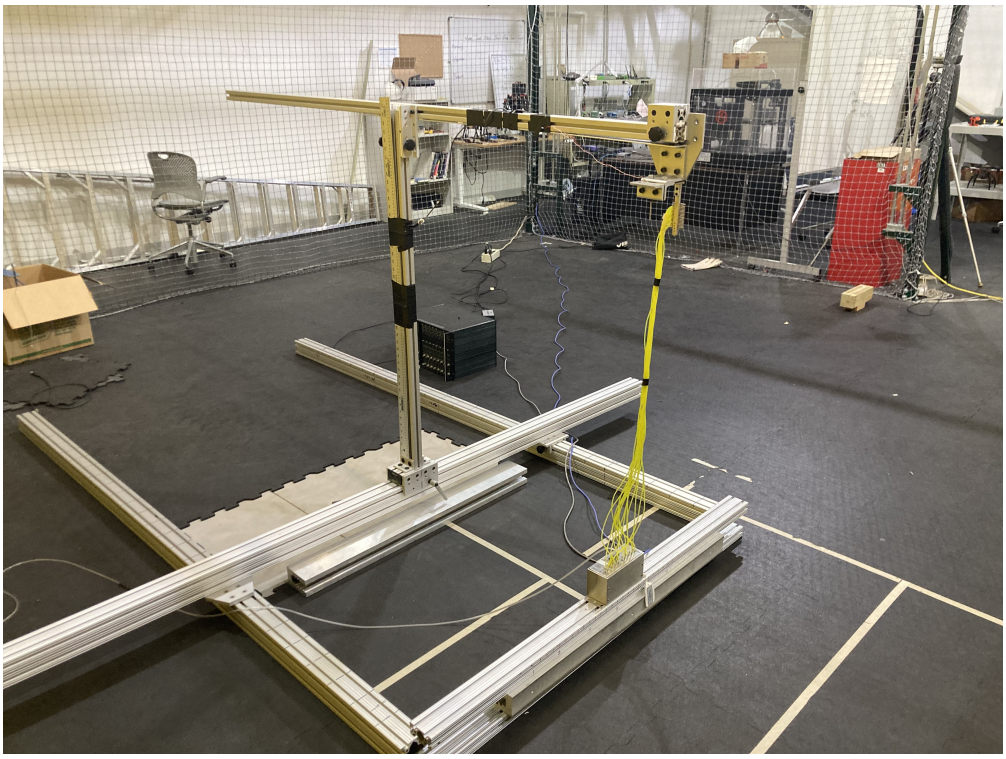

FIGURE 7.5: The spatial motion platform for Hot-wire measurement

With the measurement platform, we carry out the following calibration procedure for hot-wire measurement.

The FAWT is commanded to run in the uniform flow mode, such that every single fan of the FAWT runs at identical duty to create a uniform flow with minimum shear around the center-line ($z = 0$ m, $y = 0$ m) for calibration. This uniform flow ensures the almost identical flow velocities at the pressure tube and hot-wire probe placed in the front of

FAWT. The pressure and hot-wire voltage are acquired in eight working conditions of the FAWT, from 20 % to 90 %, with 10 % difference. The uniform flow generated in these eight working conditions covers the maximum and minimum wind velocities in the test-section during the experiment. The hot-wire voltage in the still air is also recorded for calibration. We take the data record for 10 s for both pressure measurement and hot-wire measurement simultaneously. The acquired pressure data is considered as the dynamic pressure of the incoming flow. Afterwards, by applying Bernoulli equation, we calculate the time-averaged wind velocity according to the acquired pressure data. With the time-averaged wind speed and the hot-wire voltage as a time-series, we apply the calibration procedure by (George, Woodward, and Hussein, 1989), who find that the wind velocity is a 4th order polynomial of the hot-wire voltage, such that,

$$u = C_0 + C_1 E + C_2 E^2 + C_3 E^3 + C_4 E^4, \tag{7.1}$$

where u is the wind velocity in m/s, $C_0 \sim C_4$ are coefficients for the polynomial, and E is the hot-wire voltage in V. With u and E at different working conditions, we apply orthogonal projection to obtain $C_0 \sim C_4$, which are the result of calibration. To ensure the measurement accuracy, this calibration procedure is conducted whenever we need to carry out turbulence measurement from hot-wire anemometer.

FIGURE 7.6: AN1003 hot-wire anemometer system
Source:AA Lab LTD.

FIGURE 7.7: NI9234 Data acquisition system
Source:National Instrument LTD.

7.3 Analysis techniques

To proceed the wind velocities obtained by hot-wire anemometer, we apply the following analysis techniques from the turbulence textbooks by (Pope, 2000; Tennekes and Lumley,

1972) and signal-processing textbooks by (Percival, Walden, et al., 1993; Stoica, Moses, et al., 2005).

Mean, Variance and Standard Deviation

The sample mean is defined and calculated as:

$$\overline{x} = \frac{1}{N}\sum_{i=1}^{N} x(i),$$

where N is the volume of samples and $x(i)$ is the ith sample in the series. The unbiased sample variance is defined and calculated as

$$s^2 = \frac{1}{N}\sum_{i=1}^{N}(x(i) - \overline{x})^2,$$

The unbiased standard deviation is defined and calculated as

$$s = \sqrt{\frac{1}{N}\sum_{i=1}^{N}(x(i) - \overline{x})^2},$$

Power Spectral Density (PSD)

We reference the definitions and statements by (Stoica, Moses, et al., 2005). Under some additional regularity conditions, the sequence $x(t)$ possesses a discrete–time Fourier transform (DTFT) defined as

$$X(\omega) = \sum_{t=-\infty}^{\infty} x(t)e^{-i\omega t}. \tag{7.2}$$

We define the energy spectral density of a signal as,

$$S(\omega) = \|X(\omega)\|^2. \tag{7.3}$$

Most of the signals encountered in applications are such that their variation in the future cannot be known exactly. It is only possible to make probabilistic statements about that variation. The mathematical device to describe such a signal is that of a random sequence which consists of an ensemble of possible realizations, each of which has some associated probability of occurrence. A random signal usually has finite average power and, therefore, can be characterized by an average power spectral density. For simplicity reasons, in what follows we will use the name power spectral density (PSD) for that quantity.

To numerically obtain the PSD, we employ the following definition on the PSD $E_{xx}(\omega)$, as

$$E_{xx}(\omega) = \lim_{N\to\infty} E\left\{\frac{1}{N}\|\sum_{t=1}^{N} x(t)e^{-i\omega t}\|^2\right\}, \tag{7.4}$$

which is from the following publications by (Pope, 2000; Stoica, Moses, et al., 2005; Tennekes and Lumley, 1972).

The Bartlett Power Spectral Estimation (BPSE)

We reference the definitions and statements by (Percival, Walden, et al., 1993). Bartlett's method is to reduce the variance of the PSD by averaging. We divide the N point series into K nonoverlapping data segments, where each segment has length M. This results the in the K data segments. We average the PSD for the K segments to obtain the Bartlett

power spectrum estimate, such that,

$$\overline{E}_{xx}(\omega) = \frac{1}{K}\sum_{i=1}^{K} E_{xx}^{i}(\omega), \tag{7.5}$$

Reynolds Stress

The velocity record of a turbulent flow includes both mean and fluctuating components. This holds true for other terms such as pressure and stress. The Reynolds decomposition of the velocities can be expressed as

$$u_i = U_i + u_i',$$

where capitol symbols denote the mean value and a prime is used for fluctuations. $\overline{u_i' u_i'}$ denotes the Reynolds stress. This term indicates the contribution of turbulent fluctuations to the mean stress tensor.

Turbulence Intensity

We define the turbulence intensity (TI) by:

$$\mathrm{TI} = \frac{\overline{u_i' u_i'}^{\frac{1}{2}}}{U_i}.$$

7.4 Results: pressure measurement

We carry out the pressure measurement with the setup pre-described in Section 7.2. We let the FAWT works at the uniform mode, which means every fan works at identical duty to create a homogeneous wind field within the test section. Figure 7.8 and 7.9 show the velocity map of the test section when every fan of the FAWT runs at 50% and 80%

duty, respectively. By comparing Figure 7.8 and Figure 7.9, it is obvious that when the

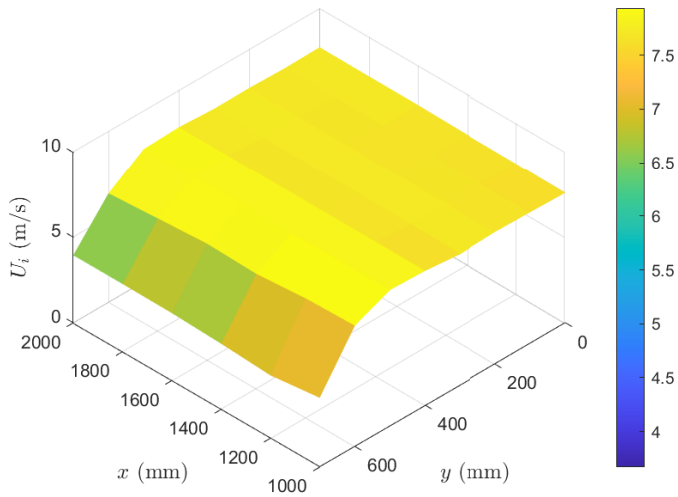

FIGURE 7.8: Velocity map of the test section when every fan work at 50%

FAWT works at uniform mode, higher duty means higher averaged velocity in the area. Moreover, higher duty implies higher spatial velocity gradients near the edge of the test section.

7.5 Results: hot-wire measurement

We carry out the hot-wire measurement with the setup described by Section 7.2, at $x = 1.2$ m, $y = 0$ m, and $z = 0$ m. This coordinate is at the upstream of the hovering position of the conducted flight experiment to be presented in Chapter 8. We carry out the anemometer measurement for several different kinds of flowfields. Among these flowfields, uniform flow is previously described in Section 7.2 when the calibration process is described. In the uniform flow mode, we command the fans to run at 30%-70% of the maximum output.

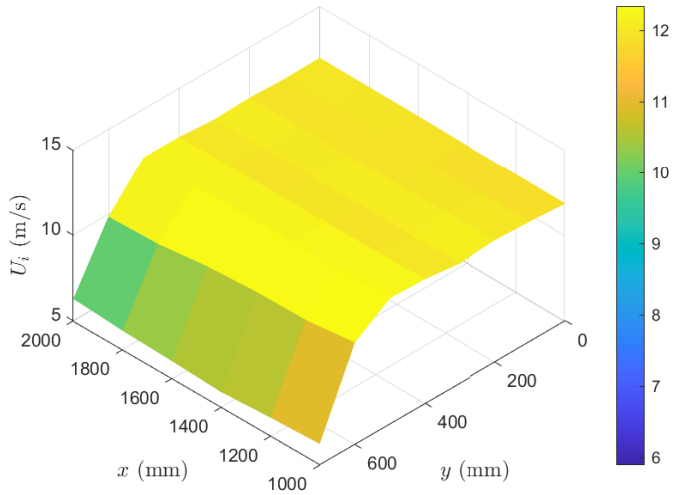

FIGURE 7.9: Velocity map of the test section when every fan work at 80%

To generate the flowfields with different turbulence characteristics, we drive a group of fans to some specific duty and keep the others at rest to initiate free-shear flow as the energy source of turbulent incoming flows with different length scales. Except for the uniform flow mode, We conduct the hot-wire measurement for six different modes of flowfields, including 'small wave' flows, 'large wave' flows, 'peak' flows, 'small block' flows, 'large block' flows, and 'huge block' flows.

To control each individual fans of the FAWT, We use the web application interface provided by *WindShape. Corp.* The inputs to generate the fore-mentioned flowfields are presented in Figures 7.10-7.15. To explain, in Figures 7.10-7.15, the dark blue block stand for the fans on-duty, while the light blue block stand for the fans at rest. For the fans on-duty, we command the fans to run at 40%-80% of the maximum output.

For each run, we turn on the FAWT for 2 minutes to stabilize the flow to a statistically steady state. Afterwards, we take 10 minutes to collect the time-series of voltage

with 6 million points, and transform them into the wind velocity using the fourth order polynomial given by (7.1). We apply the PSD and the BPSE methods given by (7.4) and (7.5), respectively, to obtain smooth PSD map for each collected velocity time-series. When using the BPSE, for each time-series of wind velocity with 6 million points, we divide them into 60 segments $(K = 60)$, where each segment length is a hundred thousand $(M = 100000)$. We list the statistical results of these flow fields in Tables 7.1-7.7 , including time-averaged velocities, Reynolds stresses, Taylor-scale Reynolds number, and TI. The spectral estimation results of these flowfields are presented in Figures B.1-B.7 attached in Appendix B.

Duty	U_i (m/s)	$\overline{u_i'u_i'}$ (m/s)^2	Re$_\lambda$	TI
30%	5.472	0.061	98	0.0451
40%	6.876	0.082	102	0.0417
50%	8.213	0.0116	100	0.0415
60%	9.590	0.0168	127	0.0427
70%	10.920	0.0237	148	0.0446

TABLE 7.1: Summary of the statistical characteristics of the uniform flows

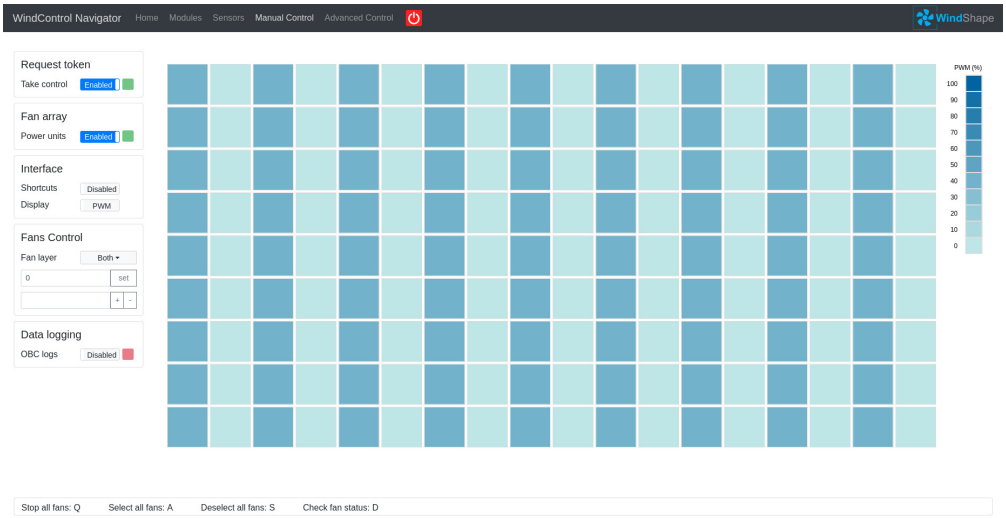

FIGURE 7.10: Input interface to generate 'small wave' flow

Duty	U_i (m/s)	$\overline{u_i' u_i'}$ (m/s)^2	Re_λ	TI
40%	5.573	0.197	179	0.0797
50%	6.680	0.249	184	0.0747
60%	7.700	0.319	191	0.0734
70%	8.722	0.424	207	0.0747
80%	9.730	0.554	235	0.0765

TABLE 7.2: Summary of the statistical characteristics of the 'small wave' flows

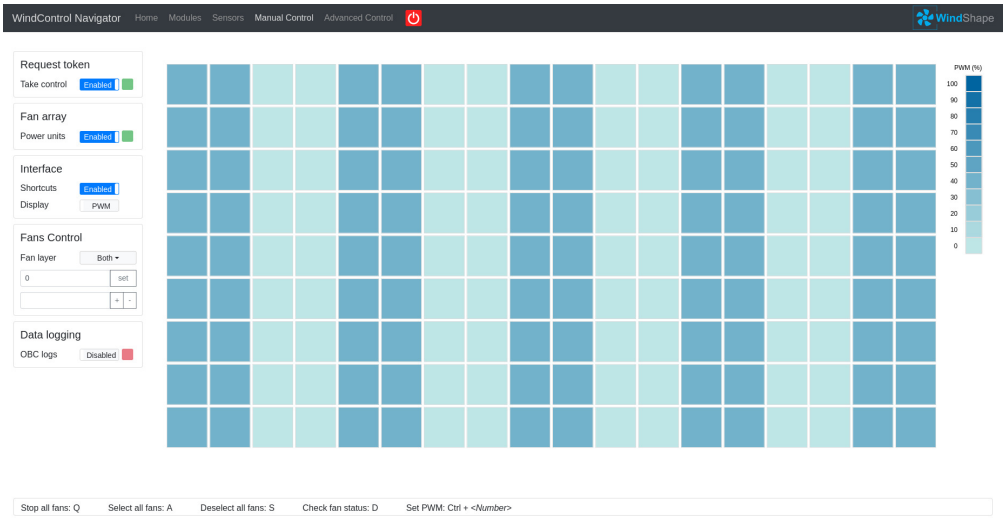

FIGURE 7.11: Input interface to generate 'large wave' flow

Duty	U_i (m/s)	$\overline{u_i' u_i'}$ $(\mathrm{m/s})^2$	Re_λ	TI
40%	5.073	0.551	293	0.1463
50%	6.317	0.807	326	0.1422
60%	7.619	1.180	390	0.1425
70%	8.783	1.549	440	0.1417
80%	9.913	1.974	502	0.1417

TABLE 7.3: Summary of the statistical characteristics of the 'small wave' flows

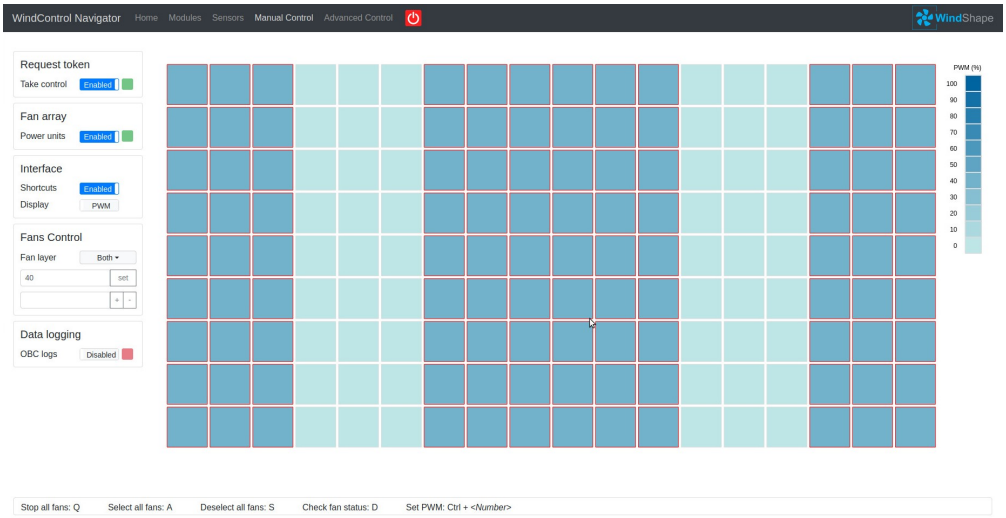

FIGURE 7.12: Input interface to generate 'peak' flow

Duty	U_i (m/s)	$\overline{u_i' u_i'}$ (m/s)^2	Re_λ	TI
40%	6.801	0.1141	116	0.0497
50%	8.244	0.1849	121	0.0522
60%	9.656	0.2900	174	0.0558
70%	11.230	0.4160	209	0.0574
80%	12.890	0.5690	248	0.0585

TABLE 7.4: Summary of the statistical characteristics of the 'peak' flows

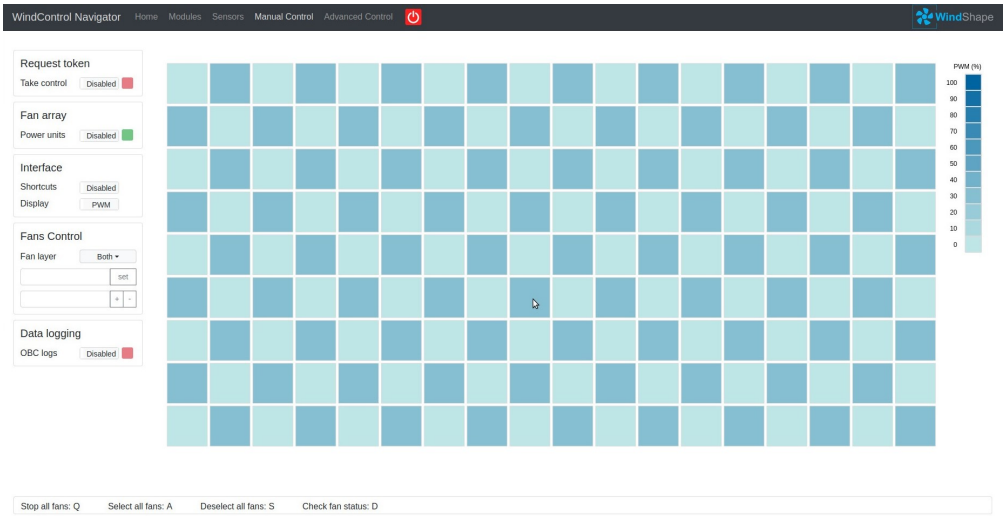

FIGURE 7.13: Input interface to generate 'small block' flow

Duty	U_i (m/s)	$\overline{u_i' u_i'}$ $(\mathrm{m/s})^2$	Re_λ	TI
40%	4.788	0.0726	92	0.0563
50%	5.930	0.1163	110	0.0575
60%	7.110	0.1700	127	0.0580
70%	8.274	0.2230	125	0.0571
80%	9.425	0.2804	157	0.0562

TABLE 7.5: Summary of the statistical characteristics of the 'small block' flows

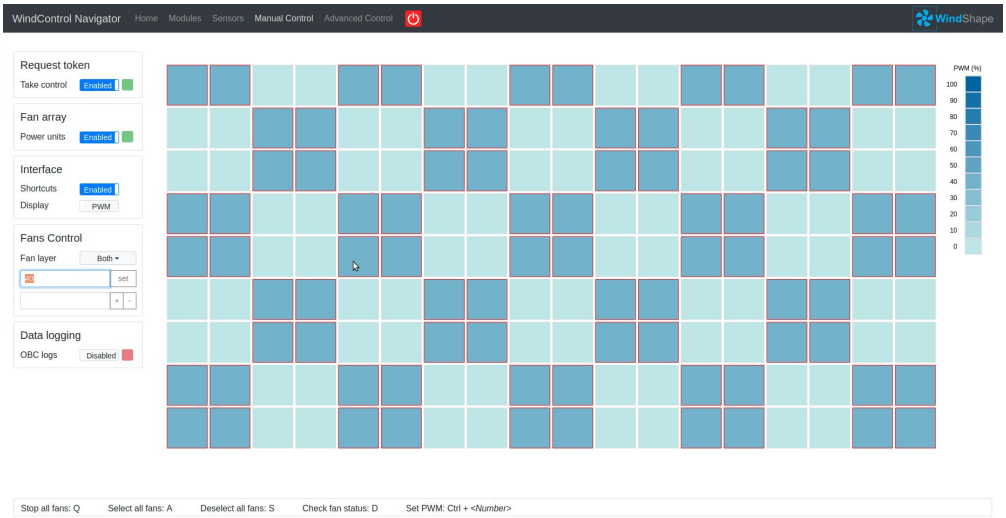

FIGURE 7.14: Input interface to generate 'large block' flow

Duty	U_i (m/s)	$\overline{u_i' u_i'}$ $(\mathrm{m/s})^2$	Re_λ	TI
40%	4.859	0.2179	158	0.0961
50%	5.998	0.3484	191	0.0984
60%	7.223	0.5110	225	0.0990
70%	8.479	0.6845	259	0.0976
80%	9.669	0.8668	297	0.0963

TABLE 7.6: Summary of the statistical characteristics of the 'large block' flows

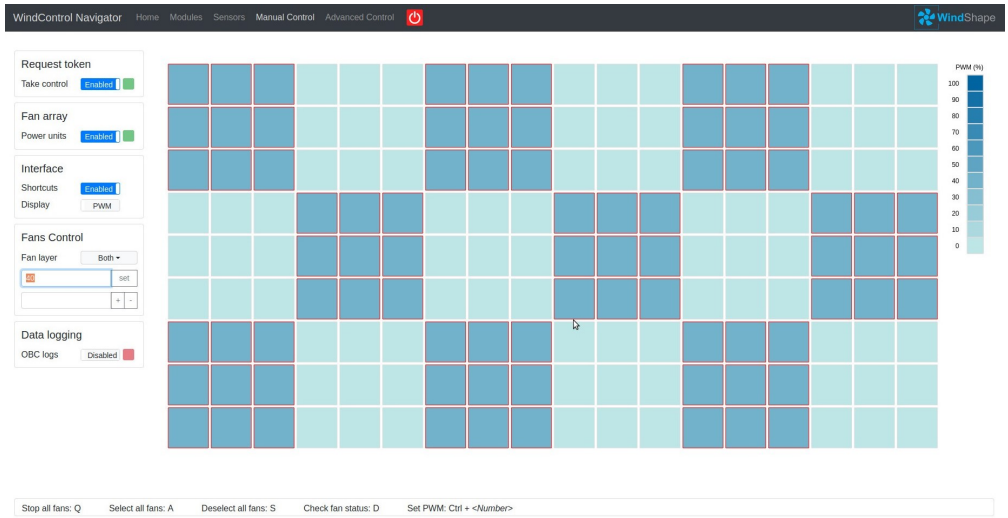

FIGURE 7.15: Input interface to generate 'huge block' flow

Duty	U_i (m/s)	$\overline{u_i' u_i'}$ (m/s)^2	Re_λ	TI
40%	5.079	0.2581	189	0.1000
50%	6.048	0.3956	215	0.1040
60%	7.095	0.5927	251	0.1085
70%	8.120	0.8202	284	0.1115
80%	9.171	1.1054	329	0.1146

TABLE 7.7: Summary of the statistical characteristics of the 'huge block' flows

7.6 Comparison and discussion

We reference the turbulence textbook by (Pope, 2000). With the Kolmogorov hypotheses we are interested in the energy-spectrum function is of the form as follows

$$E_{11}(f) = C\epsilon^{\frac{2}{3}} f^{-p}, \tag{7.6}$$

which is the famous Kolmogorov $-5/3$ spectrum. This behavior can be roughly observed in Figures B.1-B.7. We observe that for 'small wave' and 'large wave' flows, the low frequency components have higher amplitudes than uniform flows and 'peak' flows. We observe that the dominant frequency of uniform flows and 'peak' flows increase with the duties of fans. Since the measurement point is at the center-line of the downstream cross-section, 'peak' flows do not show similar behavior in their turbulence intensities when compared with 'small wave' and 'large wave' flows.

7.7 Summary

In this chapter, we conduct the measurement experiment for the FAWT using different methods. The spatial velocity maps are obtained through pressure measurement. The spectrum of the wind velocity is obtained in front of the FAWT. This chapter provides some characteristics of the turbulent incoming flows generated in the FAWT. In Chapter 8, the UAV flight experiments are conducted with the exposure of the turbulent flows investigated in this chapter.

Chapter 8

Experiment 2: Rotorcraft Flight Experiment with Turbulent Flows from Fan Array Wind Tunnel (FAWT)

In this chapter, the proposed fast finite-time stable extended state observer (FFTS-ESO) covered in Chapter 5 is validated through flight experiments. Its hardware and software are custom-designed and developed based on the open-source autopilot PX4 by (Meier, Honegger, and Pollefeys, 2015). To demonstrate the capability of estimating and rejecting the disturbances, flight experiments are conducted under wind disturbances generated by the FAWT which is described by Chapter 7 in details. We first describe the hardware and software configurations of the unmanned aerial vehicle (UAV) and the setup of the experiment. Afterwards, we present our experimental results including the characteristics of the wind disturbances and the control performance of the UAV when exposed to disturbances generated by the FAWT.

8.1 Experimental setup

The quad-rotor UAV developed at the Autonomous Unmanned Systems laboratory (AUSL) for experiment is shown in Figure 8.3. The UAV is equipped with a CUAV Nora autopilot shown in Figure 8.2. The CUAV Nora is an autopilot intended primarily for manufacturers of commercial systems. It is based on the Pixhawk-project FMUv7 and runs open-source autopilot software PX4 on the real-time operating system NuttX. We use the same motion capture system as in the experimental research by (Hamrah, 2022).

8.2 Software configuration

The flight control software is developed from the open-source autopilot software PX4 v1.13.2. According to (Meier, Honegger, and Pollefeys, 2015), the system architecture of PX4 is centered around a publish-subscribe object request broker on top of a POSIX application programming interface. This programming interface has different modules for data logging, communication, estimation, and control. The FFTS-ESO is implemented onto the module `mc_pos_control` and `mc_rate_control` for translational and rotational motions, respectively. The feedback of disturbance estimates from the ESO is applied to the control law as an additional term, so that the original control architecture is modified with this feedforward disturbance rejection term. We introduce Boolean parameters to switch the disturbance rejection conveniently.

In the experiment, the rest of the autopilot (PX4 v1.13.2) is kept unchanged, to have a fair comparison of the flight control performance between the original PX4 autopilot, and the one with disturbance rejection from FFTS-ESO. The flight control parameters of

the autopilot are as described in the multi-rotor frame S500 in the code repository of PX4-Autopilot. A Robot Operating System (ROS) interface program is developed for the companion computer that transmits commands and pose to the vehicle. The flight data are saved in the memory card inside the FCU in the form of .ulg file for post-processing. We use the MAVLINK telecommunication protocol for communication between the FCU, companion computer, and ground control station.

The FFTS-ESO parameters are selected as: $p = 1.2, k_{t1} = 6, k_{t2} = 3, k_{t3} = 1, \kappa_t = 0.6$, $k_{a1} = 8, k_{a2} = 4, k_{a3} = 2, \kappa_a = 0.6$. The empirically known mass and inertia of the vehicle as given to the FFTS-ESO are: $m = 1$ kg and $J = \text{diag}([0.03, 0.03, 0.06])$ kg $\cdot$ m^2. We link the source code of the customized PX4 with FFTS-ESO on Github.[1]

8.3 Experiment procedure

The flight experiment setup is shown in Figure 8.1. We define the FAWT coordinate frame as shown in Figure 7.1, with x as the stream-wise direction, y as the span-wise direction, and z as the vertically up direction. The origin is at the geometric center of the fan array.

[1]Github link: https://github.com/nswang1994/GeometricPX4/tree/Geometric-FFTS-ESO

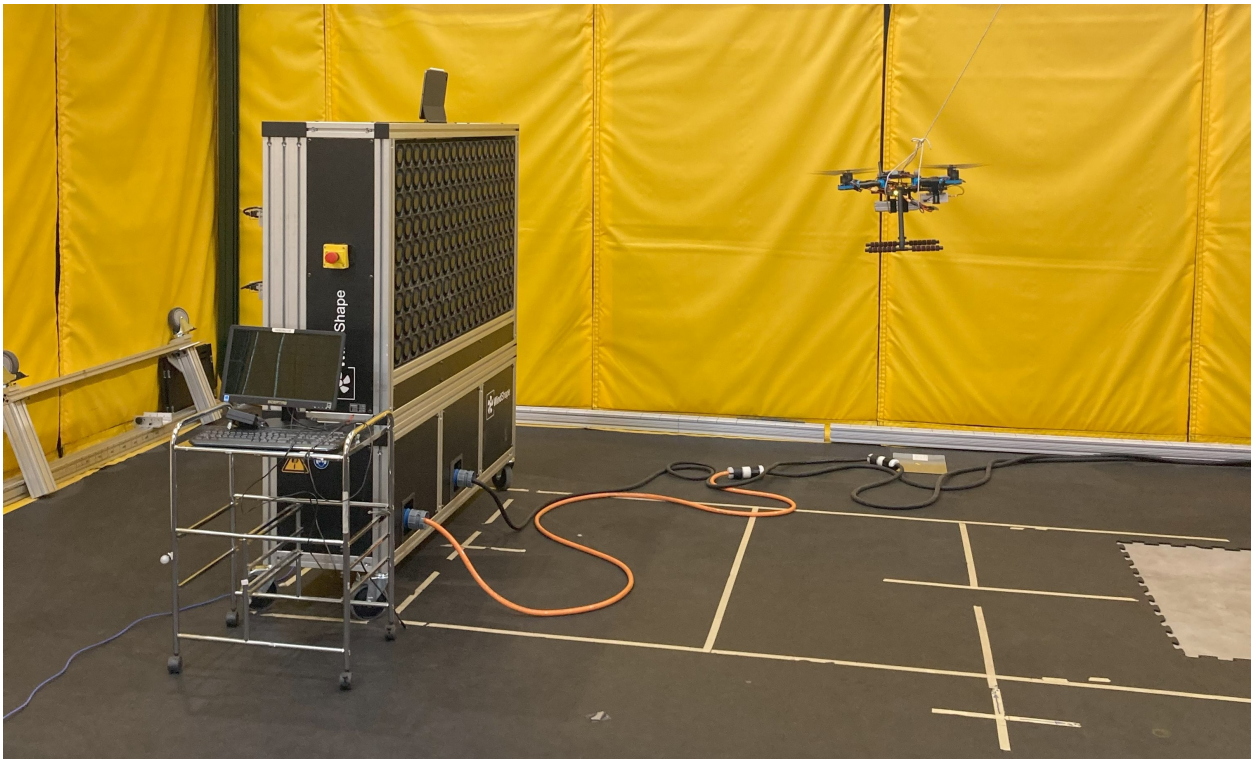

FIGURE 8.1: Multi-rotor UAV for flight test

As shown in Figure 8.1, the vehicle is commanded to hover in the front of the FAWT, at $x = 1.5\text{m}, y = 0\text{m}, z = 0\text{m}$ in the FAWT frame. This hovering position is at the center point of the test section, so that we can maximally avoid the boundary layer around the section border, where higher turbulence intensity and flow uncertainty occur. The time for hovering flight is set to 210 s. During this period, we turn on the FAWT for 150 s to disturb the vehicle with turbulent flows with statistically constant characteristics. The pose of the vehicle during flight is recorded in the log file for evaluation.

CUAV

FIGURE 8.2: Autopilot hardware: Nora, from *CUAV. LLC*

FIGURE 8.3: Multi-rotor UAV for flight test

8.4 Experimental results: PX4+FFTS-ESO

Figure 8.4 shows the experimental results of the hovering flight with uniform flows from the FAWT. Figure 8.4 shows that both position and attitude tracking errors have high transient at around 20s and 180s when the disturbances from FAWT kick in and fade off, respectively. For the attitude tracking error of the control scheme with disturbance rejection, we observe extra transient at around 0s-10s, when the disturbance rejection kick-in. we observe that when the FAWT operates at 40%-60% of its maximum duty, the position tracking error of the control scheme with disturbance rejection outperforms the one without rejection. When the FAWT operates at 30% of its maximum duty, the difference between the two control schemes is not evident. However, in terms of the time-averaged position tracking errors in Table 8.1, we can still observe that the scheme with disturbance rejection outperforms the one without rejection when the FAWT operates at 30%-60% of its maximum duty. When the FAWT operates at 70% of its maximum duty, the control scheme without disturbance rejection mechanism fails to hover constantly, while

the one with rejection succeeds.

We also conduct the flight experiments with different fan-array initiations to generate different turbulent flows to impact the hovering UAV. The experimental results are posed in Tables 8.2-8.4 and Figures C.1-C.3. We can observe that the scheme with disturbance rejection outperforms the one without rejection when they are exposed to the identical turbulent flows.

8.5 Summary

This chapter describes the flight experiment setup for validating the ADRC schemes. We present the results of the disturbance rejection control with different wind gusts from the FAWT. The experimental results show that the control scheme with a disturbance rejection mechanism from the feedback of the FFTS-ESO outperforms the original control scheme in almost any condition.

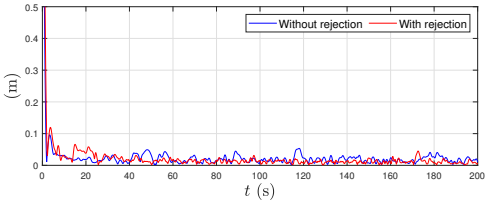

(A) 30%, $\|\widetilde{b}\|$

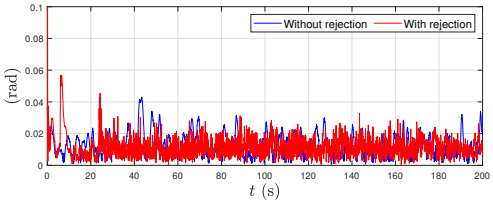

(B) 30%, $\operatorname{acos}\left(\frac{\operatorname{tr}(Q)-1}{2}\right)$

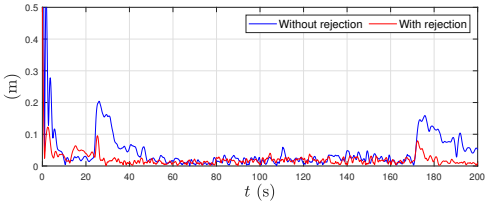

(C) 40%, $\|\widetilde{b}\|$

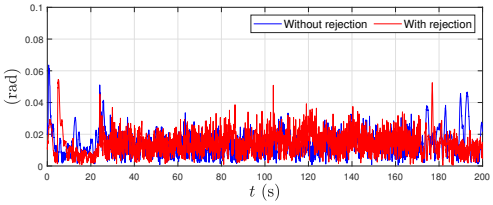

(D) 40%, $\operatorname{acos}\left(\frac{\operatorname{tr}(Q)-1}{2}\right)$

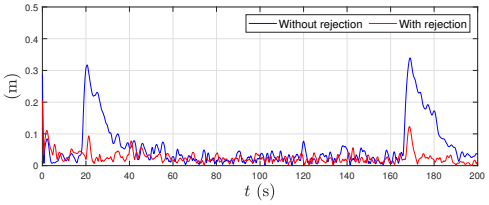

(E) 50%, $\|\widetilde{b}\|$

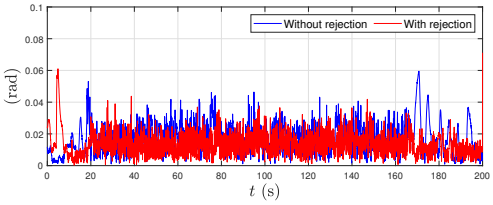

(F) 50%, $\operatorname{acos}\left(\frac{\operatorname{tr}(Q)-1}{2}\right)$

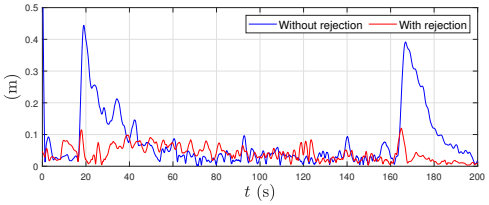

(G) 60%, $\|\widetilde{b}\|$

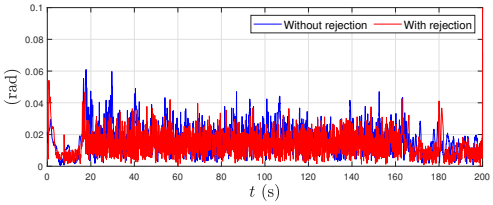

(H) 60%, $\operatorname{acos}\left(\frac{\operatorname{tr}(Q)-1}{2}\right)$

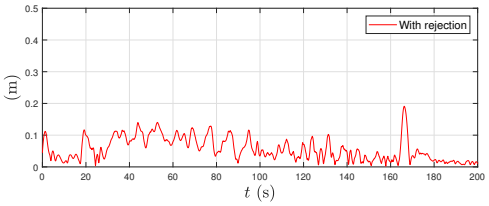

(I) 70%, $\|\widetilde{b}\|$

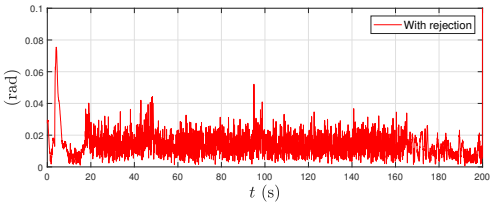

(J) 70%, $\operatorname{acos}\left(\frac{\operatorname{tr}(Q)-1}{2}\right)$

FIGURE 8.4: Uniform flow tracking error

	Position tracking error (m)		Attitude tracking error (rad)	
	PX4 Stack	PX4+FFTS-ESO	PX4 Stack	PX4+FFTS-ESO
30%	0.0251	0.0236	0.0125	0.0116
40%	0.0468	0.0211	0.0140	0.0141
50%	0.0589	0.0254	0.0166	0.0132
60%	0.0792	0.0400	0.0164	0.0134
70%	Failed!	0.0557	Failed!	0.0139

TABLE 8.1: Uniform flow time-averaged tracking error

	Position tracking error (m)		Attitude tracking error (rad)	
	PX4 Stack	PX4+FFTS-ESO	PX4 Stack	PX4+FFTS-ESO
30%	0.0351	0.0204	0.0163	0.0117
40%	0.0448	0.0234	0.0172	0.0123
50%	0.0602	0.0204	0.0187	0.0139
60%	NA	0.0270	NA	0.0159

TABLE 8.2: 'Small wave' flow time-averaged tracking error

	Position tracking error (m)		Attitude tracking error (rad)	
	PX4 Stack	PX4+FFTS-ESO	PX4 Stack	PX4+FFTS-ESO
30%	0.0347	0.0234	0.0177	0.0111
40%	0.0432	0.0244	0.0177	0.0140
50%	0.0648	0.0275	0.0228	0.0170
60%	NA	0.0303	NA	0.0198

TABLE 8.3: 'Large wave' flow time-averaged tracking error

	Position tracking error (m)		Attitude tracking error (rad)	
	PX4 Stack	PX4+FFTS-ESO	PX4 Stack	PX4+FFTS-ESO
30%	0.0378	0.0250	0.0211	0.0113
40%	0.0505	0.0257	0.0185	0.0135
50%	0.0758	0.0298	0.0267	0.0178
60%	NA	0.0303	NA	0.0198

TABLE 8.4: 'Huge wave' flow time-averaged tracking error

	Position tracking error (m)		Attitude tracking error (rad)	
	PX4 Stack	PX4+FFTS-ESO	PX4 Stack	PX4+FFTS-ESO
30%	0.0371	0.0276	0.0136	0.0102
40%	0.0542	0.0242	0.0175	0.0123
50%	0.0824	0.0352	0.0231	0.0177
60%	NA	0.0329	NA	0.0171

TABLE 8.5: 'Peak' flow time-averaged tracking error

Chapter 9

Conclusion and Future Work

We conclude this dissertation by providing a summary of each chapters here, followed by a discussion on related future work.

9.1 Conclusion

This dissertation discusses the tracking control problem of rotorcraft UAVs under complex atmospheric environments.

Chapter 2 details the Hölder-continuous differentiator. The FFTS-ESO presented in Chapter 5 are based on the proposed HCD. We present two HCD designs with FTS and FFTS, as HC-FTSD and HC-FFTSD, respectively. The stability analysis of HCDs are inspired by the strict Lyapunov function for the super-twisting algorithm by (Moreno and Osorio, 2012; Vidal, Nunes, and Hsu, 2016). In the robustness analysis, we present the Lyapunov analysis of HC-FFTSD under perturbation and measurement noise respectively. We show that the properly tuned HC-FFTSD is still PFTS.

Chapter 3 formulates the tracking control problem, the ESO problem on $\mathrm{SE}(3)$. The corresponding mathematical preliminaries are also covered in this Chapter.

Chapter 4 presents the AS-ADRC scheme, with the ES-ESO for disturbance estimation and AS tracking control, which is based on the research article by (Sanyal, Nordkvist, and Chyba, 2010). Numerical simulation confirms the stable performance of the overall AS-ADRC scheme.

Chapter 5 presents the FFTS-ADRC scheme. The FFTS-ADRC scheme is with the FFTS-ESO for disturbances estimation and FFTS tracking control scheme, which is based on the research article by (Viswanathan, Sanyal, and Samiei, 2018). The FFTS-ESO is based on the HC-FFTSD described in Chapter 2. Based on the robustness analyses conducted in Chapter 2, we conduct the robustness analysis for the FFTS-ESO under time-varying disturbances and measurement noise. In the numerical simulation section, the proposed FFTS-ESO is compared with the FxTSDO by (Liu et al., 2022) and LESO by (Shao et al., 2018b) on their disturbance estimation performance. The FFTS-ESO shows advantages in its disturbance estimation performance over the other two in the simulated environment, especially when the UAV experiences measurement noise and high maneuvers. The numerical simulation section also validates the stable tracking performance of the proposed geometric ADRC schemes under external disturbances.

Chapter 6 presents the simulated flight control performance of the proposed ADRC schemes from Software-In-The-Loop (SITL) simulation with a physics engine and open-source autopilot. The physics engine provides a simulation environment with a simulated wind field with uncertainty and measurement noise so that the proposed ADRC schemes are validated in a simulated environment with high fidelity. The proposed FFTS-ADRC shows satisfying position tracking control performance in the simulation result.

Chapter 7 and Chapter 8 describe the experimental results. Chapter 7 presents the turbulence measurement from the FAWT in different working conditions. Hot-wire and

pressure measurements are included in Chapter 7. Chapter 8 describes the multi-rotor flight experiment under the turbulence generated by the FAWT described in Chapter 7. The results reported in Chapter 7 and Chapter 8 validate the proposed ADRC schemes experimentally.

9.2 Ideas for future work

The following are ideas to extend the research presented in this dissertation:

- Compared with rotorcraft UAVs, fixed-wing UAVs are easier to be disturbed by atmospheric turbulence like wind shear and micro-burst during take-off and landing. An ADRC scheme for a fixed wing aircraft improves its flight safety and reliability.

- According to (Verling et al., 2016), in a direct comparison between rotorcraft UAV and fixed-wing (considering similar sizes), the main advantage of rotorcraft against fixed–wing systems are their superior maneuverability and especially their ability to take off and land vertically, which eliminates the need for a runway or flat grounds and allows full operational autonomy. On the other hand, fixed–wing systems are more power–efficient and have much longer endurance and higher operational range. Tail-sitter vertical take-off and landing (VTOL) UAV synthesizes the positive aspects of both fixed-wing and rotorcraft UAVs. However, this kind of UAV experiences the singularity point in pose representation every time it take-off and land. Thus, an ADRC scheme on $\mathrm{SE}(3)$ improves flight safety and reliability for tail-sitter VTOL UAVs during take-off and landing.

- According to (Moreno et al., 2021; Teng et al., 2022), the uncertainty in the control input matrix affects the control performance in both model-based control and

model-free control schemes. ESO and ADRC scheme with adaptive mechanisms to tackle these uncertainties are valuable research directions.

- In a realistic implementation of ESO and ADRC scheme for a rigid body, especially for aerospace implementation, the center of mass is not always coincident with the geometric center. Thus, ESO and ADRC scheme on $\mathrm{SE}(3)$ with spatial offset of the center of mass are necessary for aerospace implementation.

- According to the prior research by (Zhang, Xue, and Fang, 2021; Zhang et al., 2020), ESO is not only just a tool for the ADRC scheme but also a powerful tool for sensor-bias estimation , which is another valuable research direction.

- Due to the disturbances, the linear model is fragile for fluid flow in the transition stage when the Reynolds number approaches the critical value. To this end, the ESO and ADRC schemes with fast convergence performance for a large-dimension system are valuable research directions for the transition control problem in a fluid flow system.

Appendix A

Proof of Lemma 2.1.5

A.1 Proof 1

Proof. We represent x as linear combination of μ and ν,

$$x = c_1\mu + c_2\nu, \tag{A.1}$$

where ν is a vector perpendicular to μ, such that $\mu^{\mathrm{T}}\nu = 0$. We define two non-zero scalars, c_1, c_2. With (A.1), we express Y in Lemma 2.1.5 in coordinates (c_1, c_2):

$$Y = \frac{c_1\mu + c_2\nu}{\left(c_1^2\|\mu\|^2 + c_2^2\|\nu\|^2\right)^{\alpha}} - \frac{(1+c_1)\mu + c_2\nu}{\left[(1+c_1)^2\|\mu\|^2 + c_2^2\|\nu\|^2\right]^{\alpha}}. \tag{A.2}$$

Afterward, we obtain its partial derivatives with respect to these coordinates:

$$
\begin{aligned}
\frac{\partial Y}{\partial c_1} &= \frac{\mu}{\left(c_1^2\|\mu\|^2 + c_2^2\|\nu\|^2\right)^{\alpha}} - \frac{2\alpha c_1\|\mu\|^2(c_1\mu + c_2\nu)}{\left(c_1^2\|\mu\|^2 + c_2^2\|\nu\|^2\right)^{\alpha+1}} \\
&\quad - \frac{\mu}{\left[(1+c_1)^2\|\mu\|^2 + c_2^2\|\nu\|^2\right]^{\alpha}} + \frac{2\alpha(1+c_1)\|\mu\|^2\left[(1+c_1)\mu + c_2\nu\right]}{\left[(1+c_1)^2\|\mu\|^2 + c_2^2\|\nu\|^2\right]^{\alpha+1}}, \\
\frac{\partial Y}{\partial c_2} &= \frac{\nu}{\left(c_1^2\|\mu\|^2 + c_2^2\|\nu\|^2\right)^{\alpha}} - \frac{2\alpha c_2\|\nu\|^2(c_1\mu + c_2\nu)}{\left(c_1^2\|\mu\|^2 + c_2^2\|\nu\|^2\right)^{\alpha+1}} \\
&\quad - \frac{\nu}{\left[(1+c_1)^2\|\mu\|^2 + c_2^2\|\nu\|^2\right]^{\alpha}} + \frac{2\alpha c_2\|\nu\|^2\left[(1+c_1)\mu + c_2\nu\right]}{\left[(1+c_1)^2\|\mu\|^2 + c_2^2\|\nu\|^2\right]^{\alpha+1}}.
\end{aligned}
\tag{A.3}
$$

Thereafter, with the fact that the local maxima of $Y^{\mathrm{T}}Y$ fulfills, we obtain

$$
\frac{\partial}{\partial c_1}(Y^{\mathrm{T}}Y) = \frac{\partial}{\partial c_2}(Y^{\mathrm{T}}Y) = 0,
$$

which is equivalent to the following statement:

$$
\mu^{\mathrm{T}}\frac{\partial Y}{\partial c_1} = \nu^{\mathrm{T}}\frac{\partial Y}{\partial c_2} = 0, \tag{A.4}
$$

$$
\nu^{\mathrm{T}}\frac{\partial Y}{\partial c_1} = 0, \tag{A.5}
$$

$$
\mu^{\mathrm{T}}\frac{\partial Y}{\partial c_2} = 0. \tag{A.6}
$$

Substituting (A.3) into (A.4), we obtain,

$$
\begin{aligned}
&\nu^{\mathrm{T}}\frac{\partial Y}{\partial c_1} = \mu^{\mathrm{T}}\frac{\partial Y}{\partial c_2} = 0, \\
&-\frac{2\alpha c_1 c_2 \|\mu\|^2\|\nu\|^2}{\left(c_1^2\|\mu\|^2 + c_2^2\|\nu\|^2\right)^{\alpha+1}} + \frac{2\alpha(1+c_1)c_2\|\mu\|^2\|\nu\|^2}{\left[(1+c_1)^2\|\mu\|^2 + c_2^2\|\nu\|^2\right]^{\alpha+1}} = 0 \\
\longrightarrow\ & c_1\left[(1+c_1)^2\|\mu\|^2 + c_2^2\|\nu\|^2\right]^{\alpha+1} = (1+c_1)\left[c_1^2\|\mu\|^2 + c_2^2\|\nu\|^2\right]^{\alpha+1} \qquad \text{(A.7)} \\
&\text{or } c_2 = 0. \qquad \text{(A.8)}
\end{aligned}
$$

Substituting (A.3) into (A.5), we obtain,

$$
\begin{aligned}
&\mu^{\mathrm{T}}\frac{\partial Y}{\partial c_1} = 0, \\
\longrightarrow\ & \frac{(1-2\alpha\|\mu\|^2 c_1^2)\|\mu\|^2}{\left(c_1^2\|\mu\|^2 + c_2^2\|\nu\|^2\right)^{\alpha+1}} + \frac{\left[1-2\alpha(1+c_1)^2\|\mu\|^2\right]\|\mu\|^2}{\left[(1+c_1)^2\|\mu\|^2 + c_2^2\|\nu\|^2\right]^{\alpha+1}} = 0 \qquad \text{(A.9)} \\
\longleftrightarrow\ & (1+c_1)^2 = c_1^2 \\
\longleftrightarrow\ & c_1 = -\frac{1}{2}.
\end{aligned}
$$

Substituting (A.3) into (A.6), we obtain,

$$
\begin{aligned}
&\nu^{\mathrm{T}}\frac{\partial Y}{\partial c_2} = 0, \\
\longrightarrow\ & \frac{(1-2\alpha\|\nu\|^2 c_2^2)\|\nu\|^2}{\left(c_1^2\|\mu\|^2 + c_2^2\|\nu\|^2\right)^{\alpha+1}} + \frac{(1-2\alpha\|\nu\|^2 c_2^2)\|\nu\|^2}{\left[(1+c_1)^2\|\mu\|^2 + c_2^2\|\nu\|^2\right]^{\alpha+1}} = 0 \qquad \text{(A.10)} \\
\longleftrightarrow\ & (1+c_1)^2 = c_1^2 \\
\longleftrightarrow\ & c_1 = -\frac{1}{2}.
\end{aligned}
$$

We see that (A.7) does not give a real solution for $\alpha \in]0, 1/2[$. Thus, we conclude that the only solution to (A.4), (A.5), (A.6) is given by $c_1 = -1/2, c_2 = 0$. Thus, the only critical

value of $Y^{\mathrm{T}}Y$ is obtained when $x = -\mu/2$. Finally, we conclude that the global maximum of $Y^{\mathrm{T}}Y$ is at $x = -\mu/2$. We omit the analysis on the Hessian matrix of $Y^{\mathrm{T}}Y$ as a function of (c_1, c_2). $\square$

A.2 Proof 2

A.2.1 Preliminaries

Lemma A.2.1 (Weyl's Theorem)**.** (Horn and Johnson, 2012) $M, R, N \in \mathbb{H}^{n\times n}$, $M = R + N$. *Their eigenvalues are as,*

$$\lambda_1\{M\} \geq \lambda_2\{M\} \geq ... \geq \lambda_n\{M\}$$
$$\lambda_1\{R\} \geq \lambda_2\{R\} \geq ... \geq \lambda_n\{R\}$$
$$\lambda_1\{N\} \geq \lambda_2\{N\} \geq ... \geq \lambda_n\{N\}$$

The following inequality holds

$$\lambda_1\{R\} + \lambda_i\{N\} \geq \lambda_i\{M\} \geq \lambda_1\{R\} + \lambda_n\{N\},\ i = 1, 2, ...n$$

similarly,

$$\lambda_1\{N\} + \lambda_i\{R\} \geq \lambda_i\{M\} \geq \lambda_1\{N\} + \lambda_n\{R\}.\ i = 1, 2, ...n.$$

Lemma A.2.2. *Assume $x \in \mathbb{R}^n$ and $y \in \mathbb{R}^n$, where x and y are orthogonal, such that $x^T y = 0$. The dyadic matrix xy^T and yx^T are nilpotent matrices. Moreover, $xy^T + yx^T$ is nilpotent and symmetric.*

Lemma A.2.3. *Assume $x \in \mathbb{R}^n$ and $y \in \mathbb{R}^n$, where x and y are orthogonal, such that $x^T y = 0$. For an arbitrary symmetric real matrix $A \in \mathbb{R}^{n \times n}$, its eigenvalues are same as the eigenvalues of $A + c(xy^T + yx^T), c \in \mathbb{R}$.*

Lemma A.2.4. *Assume $x \in \mathbb{R}^n$. The eigenvalues of xx^T is ranked as $\lambda_n \leq \lambda_{n-1} \leq ..\lambda_1$, where $\lambda_i = 0,\ 0 \leq i \leq n-1$ and $\lambda_1 = x^T x$.*

Lemma A.2.5. *Assume $x \in \mathbb{R}^n$ and $y \in \mathbb{R}^n$, $n > 2$ where x and y are orthonormal, such that $x^T y = 0$ and $\|x\| = 1, \|y\| = 1$. $\forall a, b \in \mathbb{R}$, on the eigenvalues of the matrix $axx^T + byy^T$, there exist one eigenvalue a and one eigenvalue b. Moreover, if $ab \leq 0$, the eigenvalues other than a and b are all 0.*

Lemma A.2.6. *Define $\mu \in \mathbb{R}^n \setminus \{0\}$, $x \in \mathbb{R}^n \setminus \{0, -\mu\}$, $\alpha \in]0, 1/2[$ and $A \in \mathbb{R}^{n \times n}$, given by:*

$$A = \left[\|x\|^{-2\alpha} H(x, \alpha) - \|x + \mu\|^{-2\alpha} H(x + \mu, \alpha) \right], x \in \mathbb{R}^n \setminus \{0, -\mu\}. \tag{A.11}$$

A is a full-rank matrix except for $x = -\mu/2$.

Proof. We define the following symmetric matrices, $h, h_\mu, \in \mathbb{R}^{n \times n}$, which are given by:

$$h = 2\alpha \|x\|^{-2\alpha-2} xx^T,$$
$$h_\mu = 2\alpha \|x + \mu\|^{-2\alpha-2} (x + \mu)(x + \mu)^T,$$

so that we re-write A in the following expression:

$$A = (\|x\|^{-2\alpha} - \|x + \mu\|^{-2\alpha}) I - (h - h_\mu) \tag{A.12}$$

On the eigenvalues of h and $-h_\mu$, we obtain

$$\lambda_1\{h\} = 2\alpha\|x\|^{-2\alpha}, \lambda_2\{h\} = 0, \dots \lambda_n\{h\} = 0$$
$$\lambda_1\{-h_\mu\} = 0, \lambda_2\{-h_\mu\} = 0, \dots \lambda_n\{-h_\mu\} = -2\alpha\|x+\mu\|^{-2\alpha}.$$

Afterwards, we discuss the eigenvalues of $h - h_\mu$. On the eigenvalues of $h + (-h_\mu)$. We employ Lemma A.2.1 and obtain following inequality,

$$\lambda_n\{h\} + \lambda_i\{-h_\mu\} \leq \lambda_i\{h - h_\mu\} \leq \lambda_i\{-h_\mu\} + \lambda_1\{h\},\ 1 \leq i \leq n-1.$$
$$\longrightarrow 0 \leq \lambda_i\{h - h_\mu\} \leq 2\alpha\|x\|^{-2\alpha},\ 1 \leq i \leq n-1.$$
$$\lambda_n\{-h_\mu\} + \lambda_i\{h\} \leq \lambda_i\{h - h_\mu\} \leq \lambda_i\{h\} + \lambda_1\{-h_\mu\},\ 2 \leq i \leq n.$$
$$\longrightarrow -2\alpha\|x+\mu\|^{-2\alpha} \leq \lambda_i\{h - h_\mu\} \leq 0,\ 2 \leq i \leq n,$$

which means $\lambda_i\{h - h_\mu\} = 0,\ 2 \leq i \leq n-1,\ \lambda_1\{h - h_\mu\} > 0$ and $\lambda_n\{h - h_\mu\} < 0$. Considering the expression of A in (A.12), there are three possible situations for A to be singular matrix and we itemize them as follows:

- $(\|x\|^{-2\alpha} - \|x+\mu\|^{-2\alpha}) - 0 = 0,$
- $(\|x\|^{-2\alpha} - \|x+\mu\|^{-2\alpha}) - \lambda_1\{h - h_\mu\} = 0,$
- $(\|x\|^{-2\alpha} - \|x+\mu\|^{-2\alpha}) - \lambda_n\{h - h_\mu\} = 0.$

When $\|x\|^{-2\alpha} - \|x+\mu\|^{-2\alpha} = 0$ holds, $x = -\mu/2$ is the only solution to the equation and it makes A a singular matrix. When $\|x\|^{-2\alpha} - \|x+\mu\|^{-2\alpha} \neq 0$, A is a singular matrix if and only if $\|x\|^{-2\alpha} - \|x+\mu\|^{-2\alpha} - \lambda_{\min}\{h - h_\mu\} = 0$ or $\|x\|^{-2\alpha} - \|x+\mu\|^{-2\alpha} - \lambda_{\max}\{h - h_\mu\} = 0$. We investigate into these two situations in the following part of the proof. We

rewrite x in the following expression:

$$x = c_1\hat{\mu} + c_2\mu^{\perp}, \tag{A.13}$$

where $c_1, c_2 \in \mathbb{R}$, $\hat{\mu}$ and $\mu^{\perp}$ are unit vectors along and perpendicular to μ, respectively. Thus, we rewrite $x + \mu$ in the following expression:

$$x + \mu = (c_1 + \|\mu\|)\hat{\mu} + c_2\mu^{\perp}. \tag{A.14}$$

We substitute (A.13) and (A.14) into the expression of $h - h_\mu$ and obtain,

$$\begin{aligned} h - h_\mu = & \frac{2\alpha c_1^2 \hat{\mu}(\hat{\mu})^T}{(c_1^2 + c_2^2)^{\alpha+1}} + \frac{2\alpha c_2^2 \mu^{\perp}(\mu^{\perp})^T}{(c_1^2 + c_2^2)^{\alpha+1}} + \frac{2\alpha c_1 c_2 \hat{\mu}(\mu^{\perp})^T}{(c_1^2 + c_2^2)^{\alpha+1}} + \frac{2\alpha c_1 c_2 \mu^{\perp}(\hat{\mu})^T}{(c_1^2 + c_2^2)^{\alpha+1}} \\ & - \frac{2\alpha(c_1 + \|\mu\|)^2 \hat{\mu}(\hat{\mu})^T}{\left[(c_1 + \|\mu\|)^2 + c_2^2\right]^{\alpha+1}} - \frac{2\alpha c_2^2 \mu^{\perp}(\mu^{\perp})^T}{\left[(c_1 + \|\mu\|)^2 + c_2^2\right]^{\alpha+1}} \\ & - \frac{2\alpha(c_1 + \|\mu\|) c_2 \hat{\mu}(\mu^{\perp})^T}{\left[(c_1 + \|\mu\|)^2 + c_2^2\right]^{\alpha+1}} - \frac{2\alpha(c_1 + \|\mu\|) c_2 \mu^{\perp}(\hat{\mu})^T}{\left[(c_1 + \|\mu\|)^2 + c_2^2\right]^{\alpha+1}}. \end{aligned} \tag{A.15}$$

We employ Lemma A.2.3 and introduce $h^* \in \mathbb{R}^{n \times n}$, which has the same eigenvalues with $h - h_\mu$. We define h^* as follows:

$$\begin{aligned} h^* = & \frac{2\alpha c_1^2 \hat{\mu}(\hat{\mu})^T}{(c_1^2 + c_2^2)^{\alpha+1}} - \frac{2\alpha(c_1 + \|\mu\|)^2 \hat{\mu}(\hat{\mu})^T}{\left[(c_1 + \|\mu\|)^2 + c_2^2\right]^{\alpha+1}} \\ & + \frac{2\alpha c_2^2 \mu^{\perp}(\mu^{\perp})^T}{(c_1^2 + c_2^2)^{\alpha+1}} - \frac{2\alpha c_2^2 \mu^{\perp}(\mu^{\perp})^T}{\left[(c_1 + \|\mu\|)^2 + c_2^2\right]^{\alpha+1}}. \end{aligned} \tag{A.16}$$

From the expression of h^* in (A.16), we employ Lemma A.2.5 and obtain the non-zero eigenvalues of $h - h_\mu$ as λ_{h1} and λ_{h2} , such that,

$$\begin{aligned}\lambda_{h1} &= \frac{2\alpha c_1^2}{(c_1^2+c_2^2)^{\alpha+1}} - \frac{2\alpha(c_1+\|\mu\|)^2}{\left[(c_1+\|\mu\|)^2+c_2^2\right]^{\alpha+1}},\\ \lambda_{h2} &= \frac{2\alpha c_2^2}{(c_1^2+c_2^2)^{\alpha+1}} - \frac{2\alpha c_2^2}{\left[(c_1+\|\mu\|)^2+c_2^2\right]^{\alpha+1}}.\end{aligned} \tag{A.17}$$

Firstly, we assume $\|x\|^{-\alpha} - \|x+\mu\|^{-2\alpha} - \lambda_{h1} = 0$ has solution and try to find the solution. To this end, we rewrite the equation,

$$(c_1^2+c_2^2)^{-\alpha} - \frac{2\alpha c_1^2}{(c_1^2+c_2^2)^{\alpha+1}} = \left[(c_1+\|\mu\|)^2+c_2^2\right]^{-\alpha} - \frac{2\alpha(c_1+\|\mu\|)^2}{\left[(c_1+\|\mu\|)^2+c_2^2\right]^{\alpha+1}}. \tag{A.18}$$

With (A.18), we introduce the function $f : \mathbb{R}^+ \to \mathbb{R}$, given by:

$$f(e) = \left[(c_1+e)^2+c_2^2\right]^{-\alpha} - \frac{2\alpha(c_1+e)^2}{\left[(c_1+e)^2+c_2^2\right]^{\alpha+1}}.$$

Afterwards, with $f(\|\mu\|)$, we write (A.18) into the form of algebraic equation as, $f(0) = f(\|\mu\|)$. According to Rolle's theorem, if $f(0) = f(\|\mu\|)$ has a real solution, there exists the combination of e, c_1 and c_2, which make $f'(e) = 0$, where $0 < e < \|\mu\|$. We obtain $f'(e)$

$$f'(e) = -6\alpha(c_1+e)\left[(c_1e)^2+c_2^2\right]^{-\alpha-1} - 4\alpha(c_1+e)^3(-\alpha-1)\left[(c_1+e)^2+c_2^2\right]^{-\alpha-2}. \tag{A.19}$$

We fix $f'(e) = 0$, such that,

$$0 = (1 - 2\alpha)(c_1 + e)^2 + 3c_2^2. \tag{A.20}$$

From (A.20), we identify that only when $c_2 = 0$, (A.18) has real solution. We substitute $c_2 = 0$ into (A.18) and fix $\|\mu\|$ in (A.18). Afterwards, we find $c_1 = -\|\mu\|/2, c_2 = 0$ is the only solution to (A.18), indicating $x = -\mu/2$ is the only solution to the equation $\|x\|^{-\alpha} - \|x + \mu\|^{-2\alpha} - \lambda_{h1} = 0$, which makes (A.11) a singular matrix. Secondly, we assume $\|x\|^{-2\alpha} - \|x + \mu\|^{-2\alpha} - \lambda_{h2} = 0$ and try to find its solution. We firstly identify the following statement,

$$\begin{aligned}
&\|x\|^{-2\alpha} - \|x + \mu\|^{-2\alpha} > 0 \\
\rightarrow &(c_1^2 + c_2^2)^{-\alpha} - \left[(c_1 + \|\mu\|)^2 + c_2^2\right]^{-\alpha} > 0 \leftrightarrow c_1^2 < (c_1 + \|\mu\|)^2.
\end{aligned}$$

Similarly, there is

$$\begin{aligned}
&\|x\|^{-2\alpha} - \|x + \mu\|^{-2\alpha} < 0 \\
\rightarrow &(c_1^2 + c_2^2)^{-\alpha} - \left[(c_1 + \|\mu\|)^2 + c_2^2\right]^{-\alpha} < 0 \leftrightarrow c_1^2 > (c_1 + \|\mu\|)^2.
\end{aligned}$$

With the above two statements, we rewrite $\|x\|^{-2\alpha} - \|x + \mu\|^{-2\alpha} - \lambda_{h2} = 0$ as,

$$\begin{aligned}
&(c_1^2 + c_2^2)^{-\alpha} - \left[(c_1 + \|\mu\|)^2 + c_2^2\right]^{-\alpha} - \frac{2\alpha c_2^2}{c_1^2 + c_2^2}(c_1^2 + c_2^2)^{-\alpha} \\
&+ \frac{2\alpha c_2^2}{(c_1 + \|\mu\|)^2 + c_2^2}\left[(c_1 + \|\mu\|)^2 + c_2^2\right]^{-\alpha} = 0.
\end{aligned} \tag{A.21}$$

On (A.21), when $\|x\|^{-2\alpha} - \|x+\mu\|^{-2\alpha} > 0$, which means $c_1^2 < (c_1 + \|\mu\|)^2$, we obtain,

$$1 > \frac{2\alpha c_2^2}{c_1^2 + c_2^2} > \frac{2\alpha c_2^2}{(c_1 + \|\mu\|)^2 + c_2^2} > 0.$$

Similarly, when $\|x\|^{-2\alpha} - \|x+\mu\|^{-2\alpha} < 0$, which means $c_1^2 > (c_1 + \|\mu\|)^2$, we obtain,

$$1 > \frac{2\alpha c_2^2}{(c_1 + \|\mu\|)^2 + c_2^2} > \frac{2\alpha c_2^2}{c_1^2 + c_2^2} > 0.$$

Thus, (A.21) holds if and only if $\|x\|^{-\alpha} - \|x+\mu\|^{-2\alpha} = 0$, which means $x = -\mu/2$. To conclude, if and only if when $x = -\mu/2$, A in (A.11) is a singular matrix. □

A.2.2 Proof of Lemma 2.1.5

Finally, we present the proof of Lemma 2.1.5.

Proof (Lemma 2.1.5)**.** We obtain the Jacobian of $\phi(x)$ and set it to zero, which gives us the critical point of $\phi(x)$. We obtain the Jacobian of $\phi(x)$ as

$$\frac{\mathrm{d}\phi}{\mathrm{d}x} = 2\Big[\|x\|^{-2\alpha}x - \|x+\mu\|^{-2\alpha}(x+\mu)\Big]^{\mathrm{T}}\Big[\|x\|^{-2\alpha}H(x,\alpha) - \|x+\mu\|^{-2\alpha}H(x+\mu,\alpha)\Big]. \tag{A.22}$$

We define $A \in \mathbb{R}^{n\times n}$, such that,

$$A(x) = \Big[\|x\|^{-2\alpha}H(x,\alpha) - \|x+\mu\|^{-2\alpha}H(x+\mu,\alpha)\Big]. \tag{A.23}$$

Thereafter, we have the following equation

$$\left(\frac{\mathrm{d}\phi}{\mathrm{d}x}\right)^{\mathrm{T}} = 2A(x)Y(x) = 0. \tag{A.24}$$

We find that $x = -\mu/2$ is a solution to (A.24). Now we prove $x = -\mu/2$ is the unique solution to (A.24) so that $x = -\mu/2$ is not only local extrema but also global extrema for $\phi(x)$. We first assume there exists a solution other than $x = -\mu/2$ for (A.24). With $\alpha \in]0, 1/2[$, $\forall x \in \mathcal{D} \setminus \{-\mu/2\}$, we find that $A(x)$ is a full-rank matrix. Therefore, $\forall x \in \mathcal{D} \setminus \{-\mu/2\}$, the only solution to $A(x)Y(x) = 0$, is $Y(x) = 0$. If such x exists, it fulfills the following equation,

$$\frac{x}{\|x\|^{2\alpha}} = \frac{x+\mu}{\|x+\mu\|^{2\alpha}}. \tag{A.25}$$

This means that x and $x + \mu$ are linearly dependent, i.e.

$$\exists c \in \mathbb{R} \setminus \{0\}, x + \mu = cx. \rightarrow x = \frac{\mu}{c-1}. \tag{A.26}$$

Substituting (A.26) into (A.25), we obtain

$$\frac{x}{\|x\|^{2\alpha}} = \frac{cx}{c^{2\alpha}\|x\|^{2\alpha}} \leftrightarrow c^{1-2\alpha} = 1 \tag{A.27}$$

For the solution of (A.27), we got two solutions. If $\alpha = 1/2$, $\forall c \in \mathbb{R}$, (A.27) holds. If $\alpha \neq 1/2$, $c = 1 \rightarrow \mu = 0$. With $\alpha \in]0, 1/2[$ and $\mu \in \mathbb{R}^n \setminus \{0\}$ assumed in Lemma 2.1.5, we comes to the contradiction. Thus $Y(x)$ is a non-zero vector. Thus, $x = -\mu/2$ makes $\phi(x)$

for global maximum, which is

$$\max\{\phi(x)\} = \phi\Big(-\frac{\mu}{2}\Big) = \Big(2^{2\alpha}\|\mu\|^{1-2\alpha}\Big)^2.$$

We omit the analysis on the Hessian of ϕ for brevity. $\square$

Appendix B

Results on Turbulence Spectral Estimation

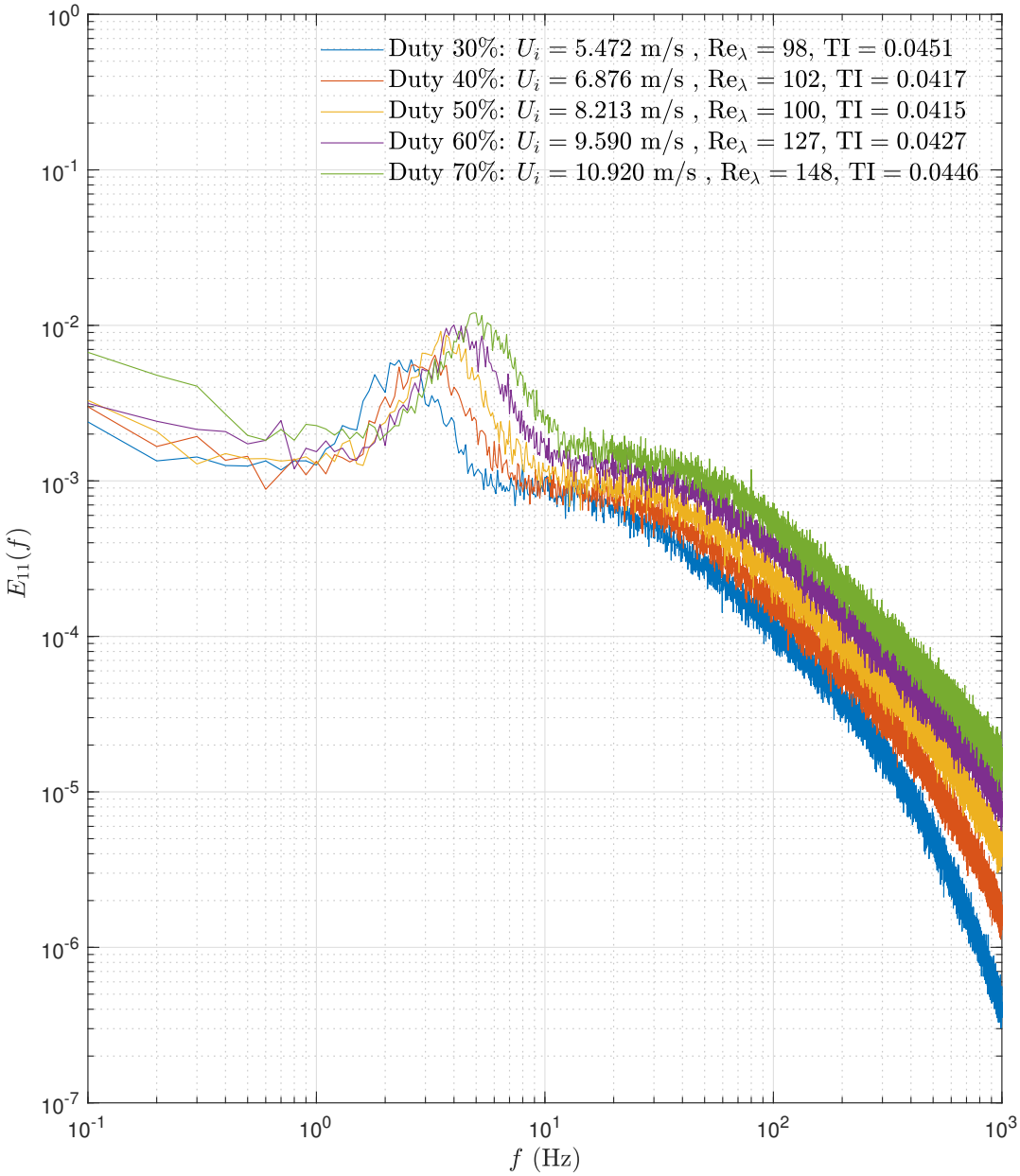

FIGURE B.1: Summary of PSD estimation for uniform flow

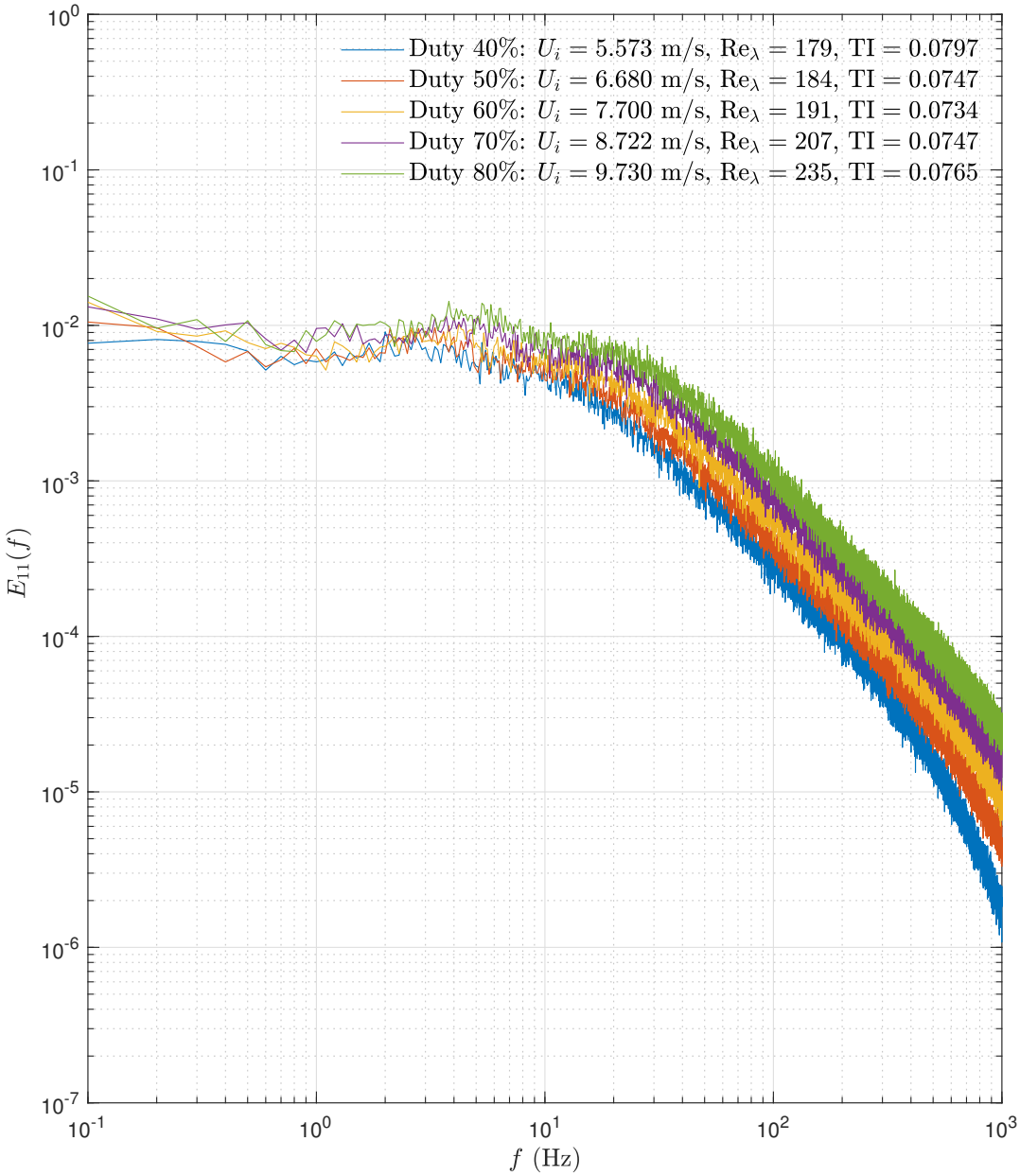

FIGURE B.2: Summary of PSD estimation for 'small wave' flows

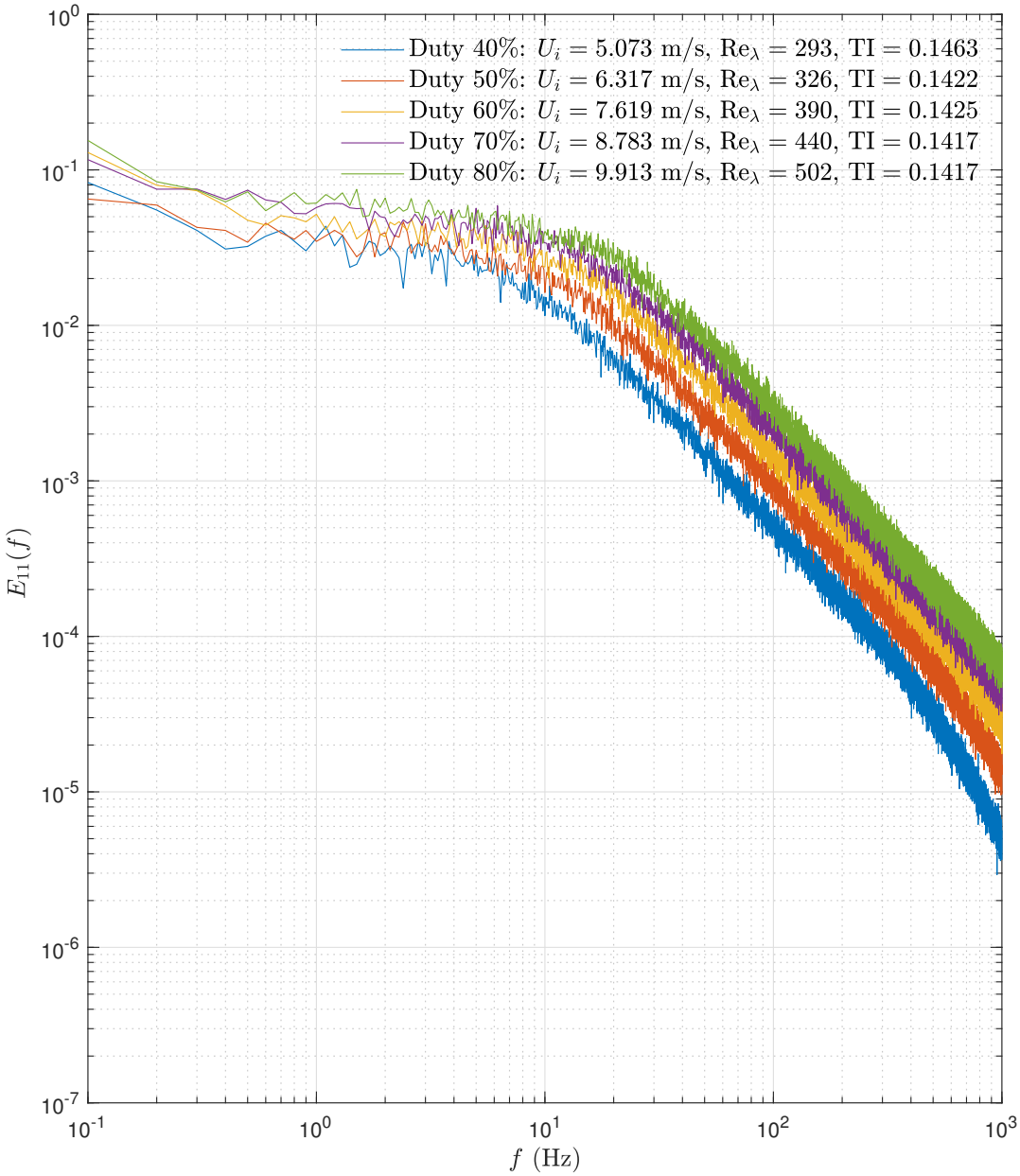

FIGURE B.3: Summary of PSD estimation for 'large wave' flows

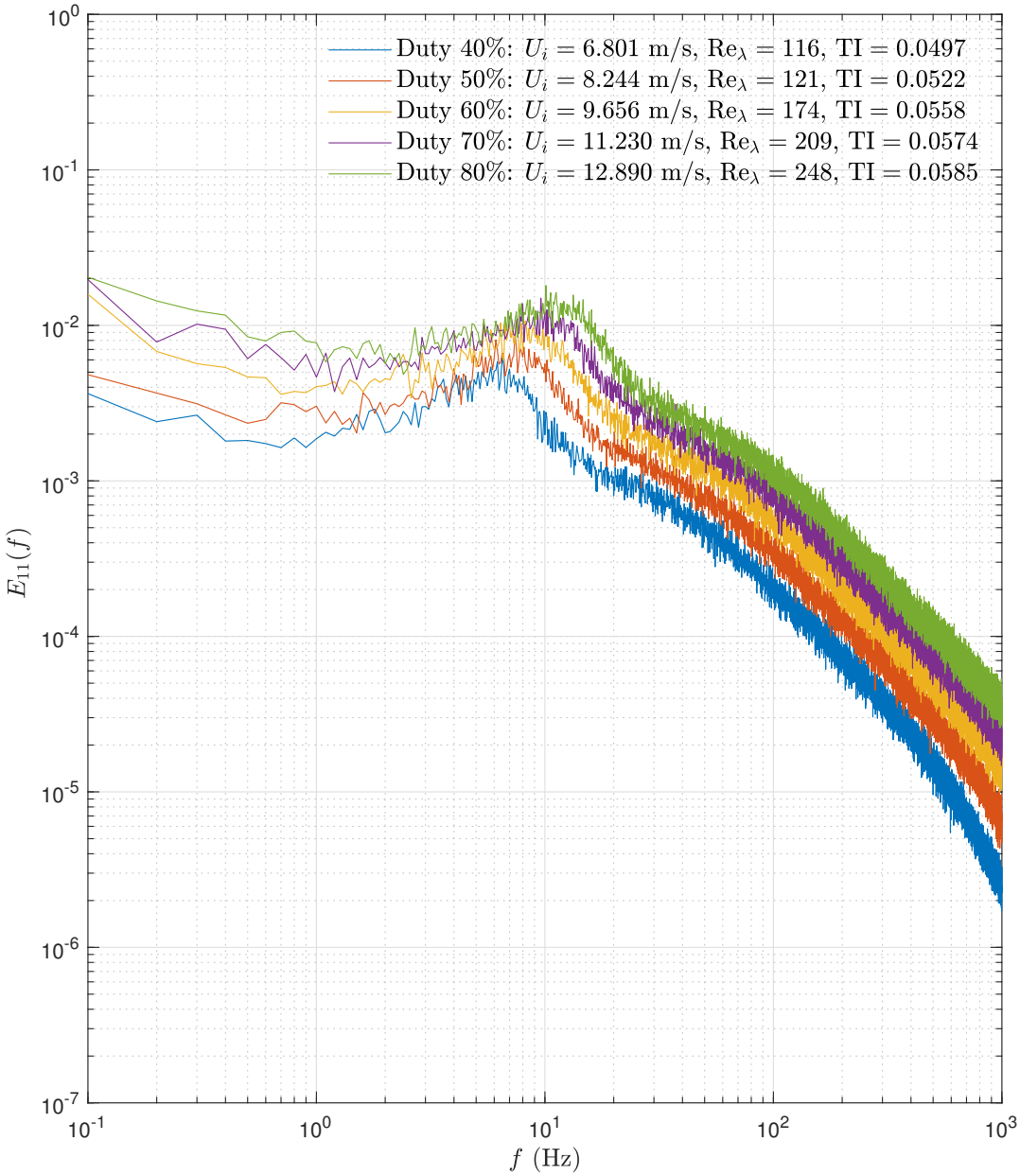

FIGURE B.4: Summary of PSD estimation for 'peak' flows

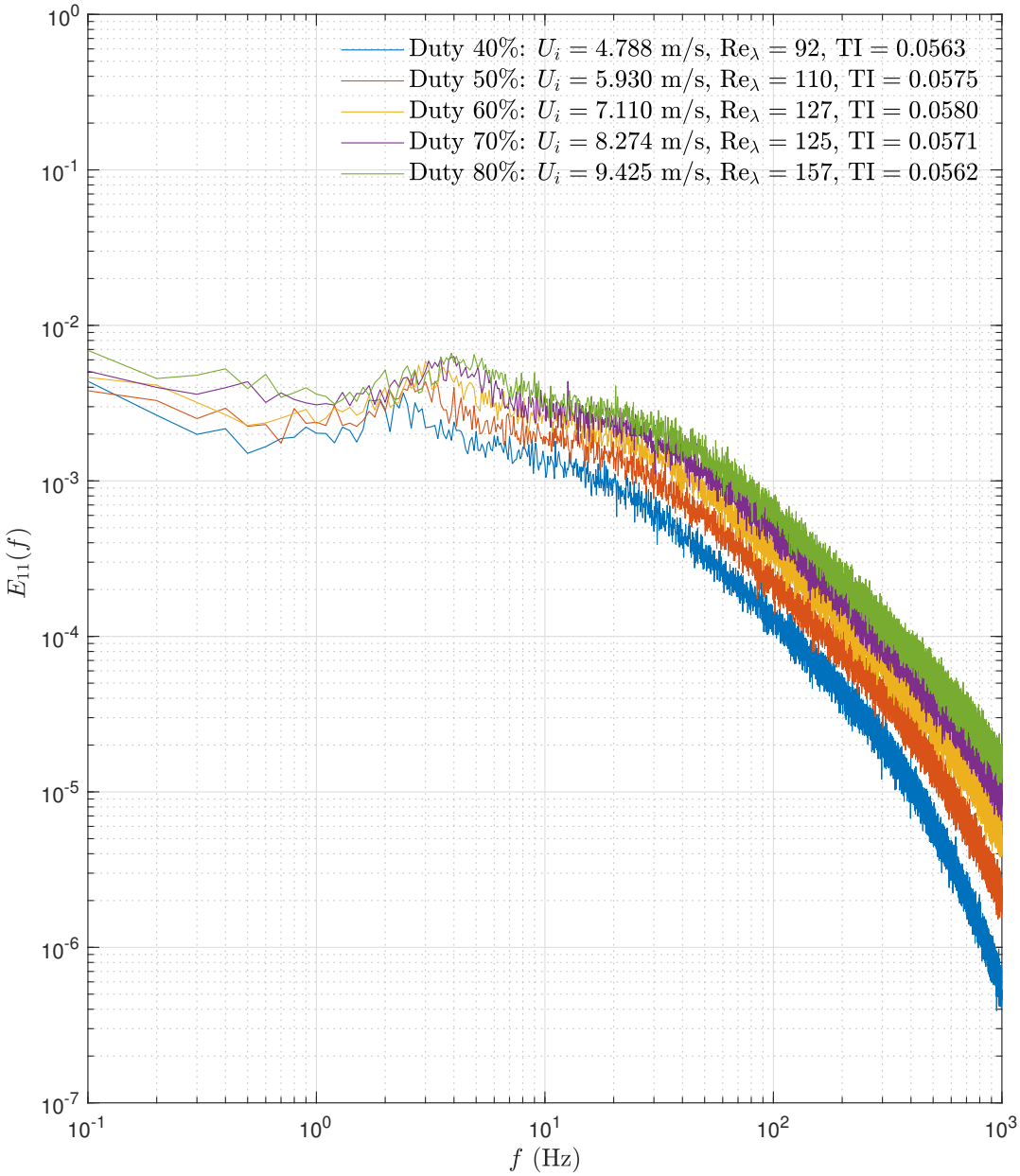

FIGURE B.5: Summary of PSD estimation for 'small block' flows

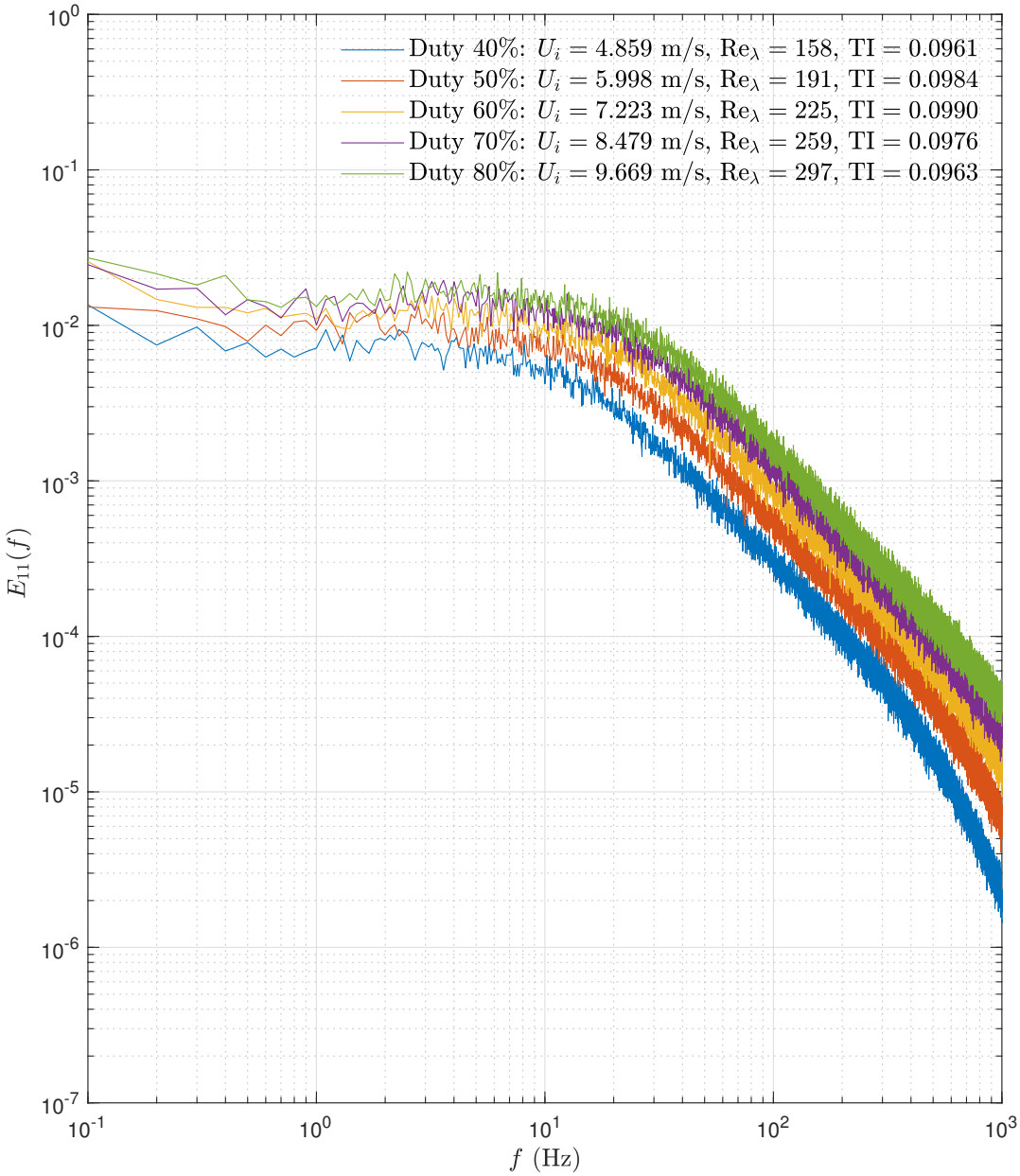

FIGURE B.6: Summary of PSD estimation for 'large block' flows

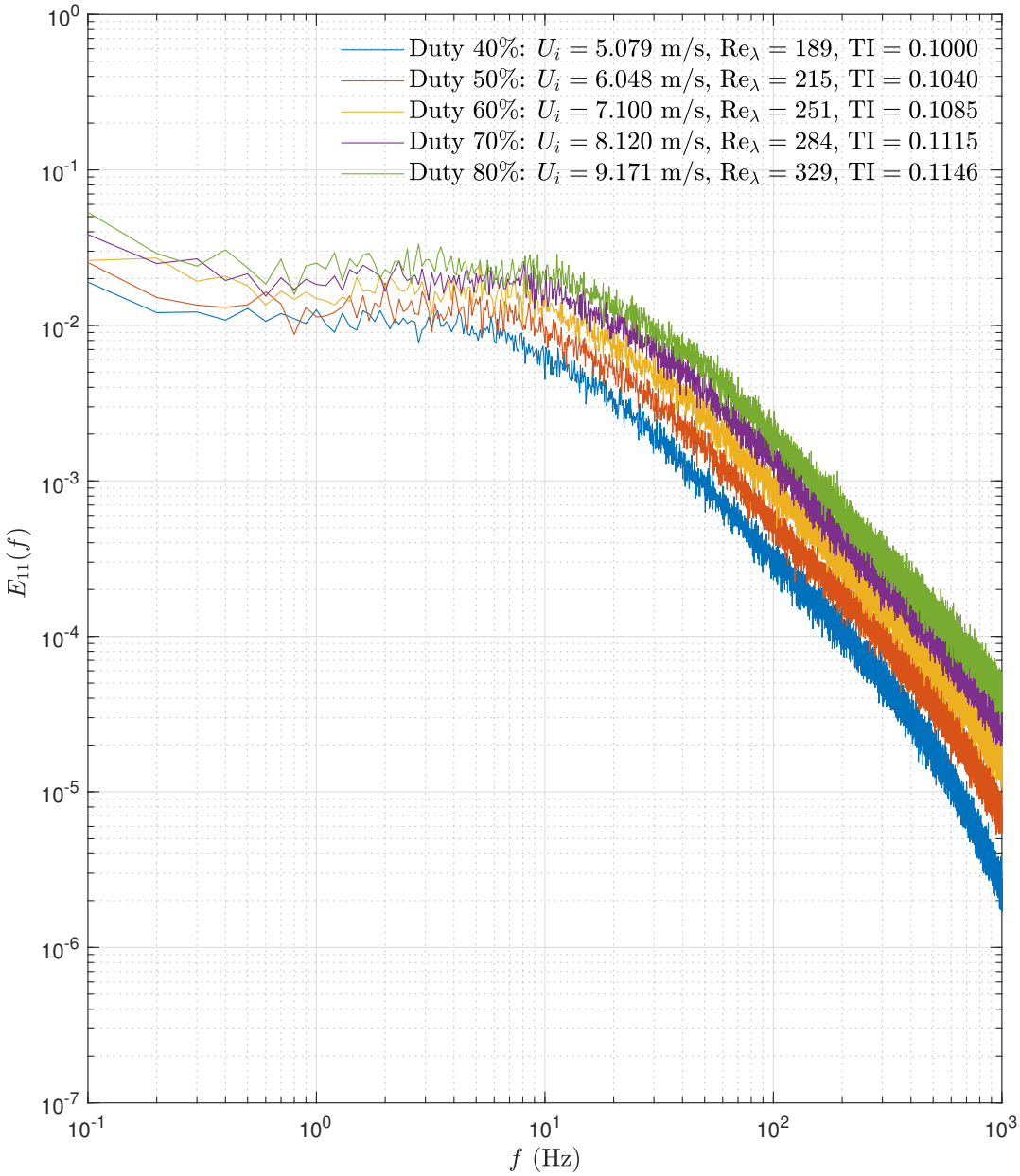

FIGURE B.7: Summary of PSD estimation for 'huge block' flows

Appendix C

Results on Flight Experiments with Fan-Array Wind Tunnel (FAWT)

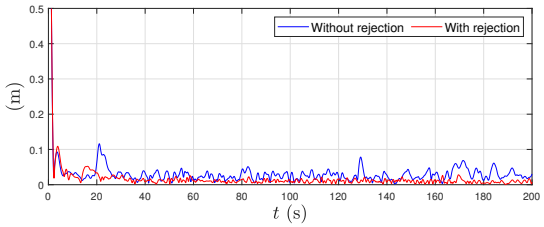

(A) 30%, $\|\widetilde{b}\|$

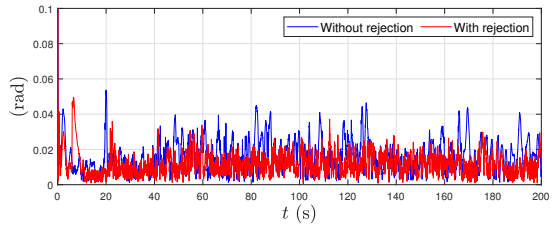

(B) 30%, acos $\left(\frac{\mathrm{tr}(Q)-1}{2}\right)$

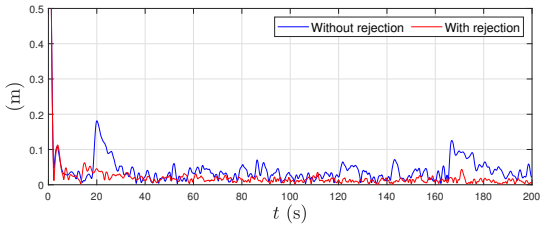

(C) 40%, $\|\widetilde{b}\|$

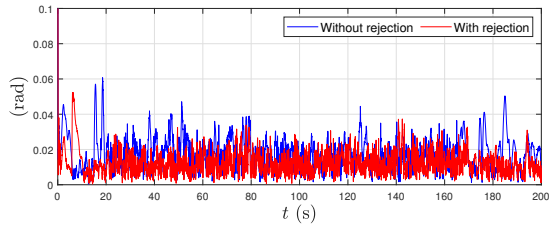

(D) 40%, acos $\left(\frac{\mathrm{tr}(Q)-1}{2}\right)$

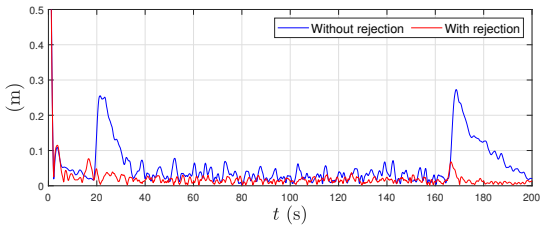

(E) 50%, $\|\widetilde{b}\|$

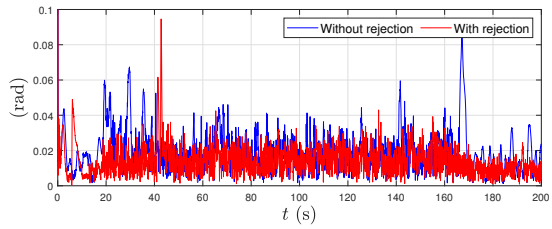

(F) 50%, acos $\left(\frac{\mathrm{tr}(Q)-1}{2}\right)$

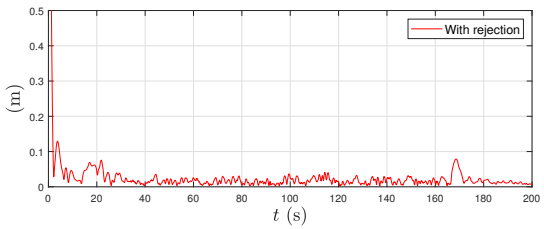

(G) 60%, $\|\widetilde{b}\|$

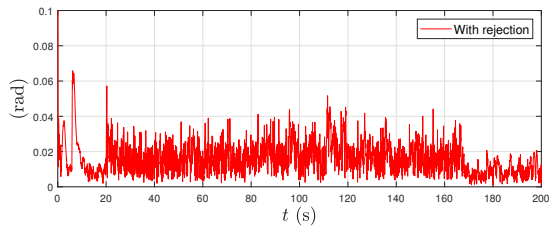

(H) 60%, acos $\left(\frac{\mathrm{tr}(Q)-1}{2}\right)$

FIGURE C.1: 'Small wave' flow tracking error

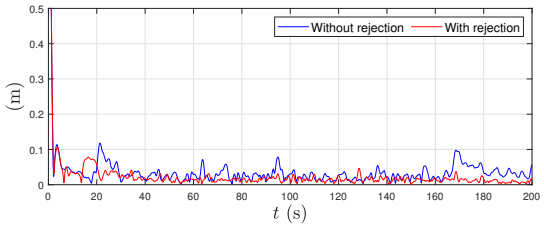

(A) 30%, $\|\widetilde{b}\|$

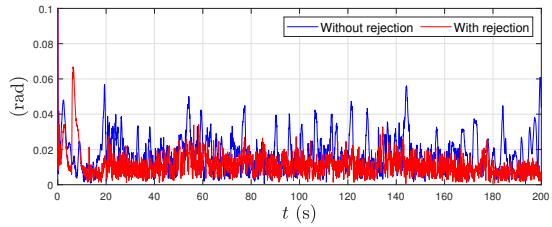

(B) 30%, $\operatorname{acos}\left(\frac{\operatorname{tr}(Q)-1}{2}\right)$

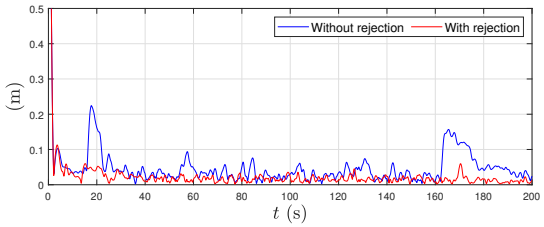

(C) 40%, $\|\widetilde{b}\|$

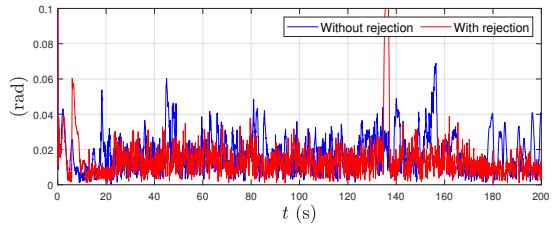

(D) 40%, $\operatorname{acos}\left(\frac{\operatorname{tr}(Q)-1}{2}\right)$

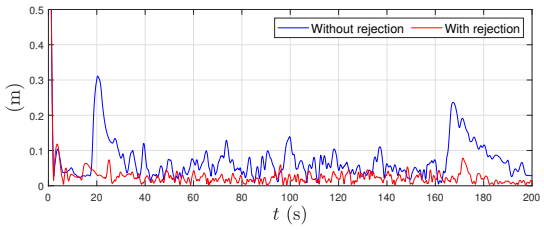

(E) 50%, $\|\widetilde{b}\|$

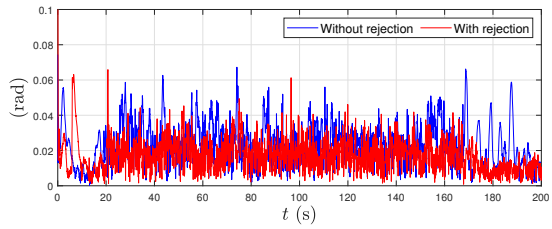

(F) 50%, $\operatorname{acos}\left(\frac{\operatorname{tr}(Q)-1}{2}\right)$

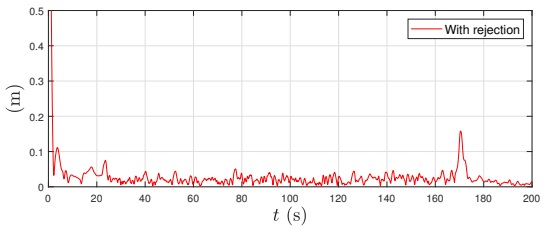

(G) 60%, $\|\widetilde{b}\|$

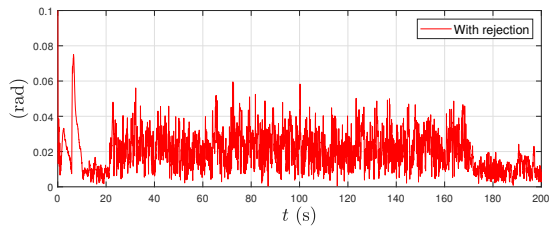

(H) 60%, $\operatorname{acos}\left(\frac{\operatorname{tr}(Q)-1}{2}\right)$

FIGURE C.2: 'Large wave' flow tracking error

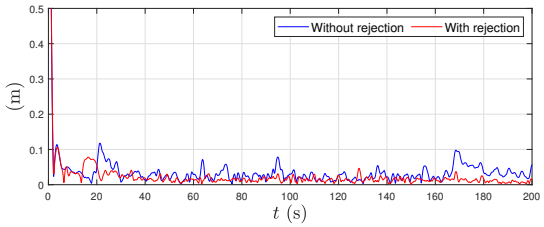

(A) 30%, $\|\widetilde{b}\|$

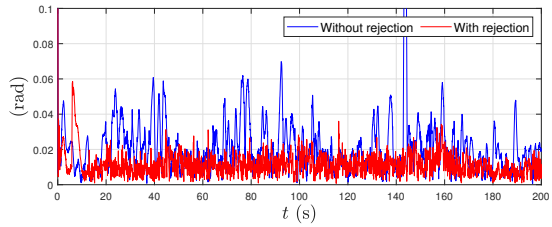

(B) 30%, $\operatorname{acos}\left(\frac{1}{2}(\operatorname{tr}(Q)-1)\right)$

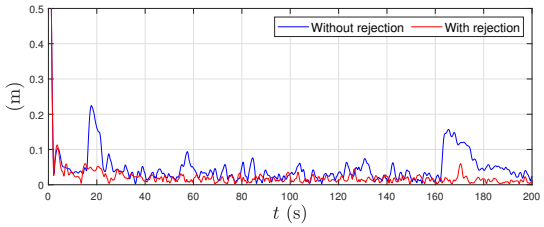

(C) 40%, $\|\widetilde{b}\|$

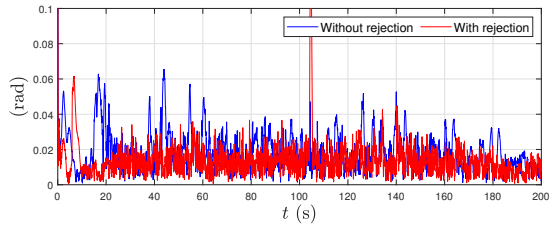

(D) 40%, $\operatorname{acos}\left(\frac{1}{2}(\operatorname{tr}(Q)-1)\right)$

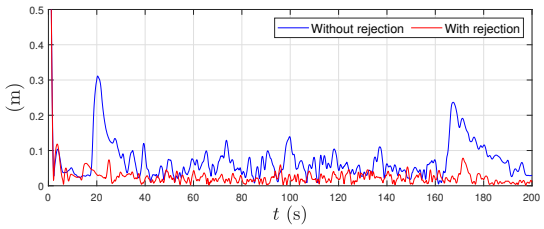

(E) 50%, $\|\widetilde{b}\|$

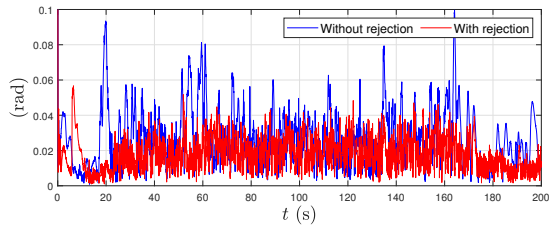

(F) 50%, $\operatorname{acos}\left(\frac{1}{2}(\operatorname{tr}(Q)-1)\right)$

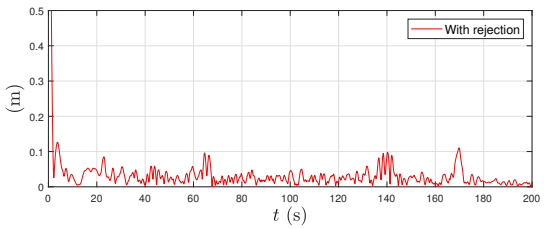

(G) 60%, $\|\widetilde{b}\|$

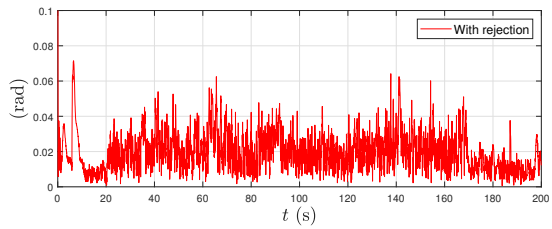

(H) 60%, $\operatorname{acos}\left(\frac{1}{2}(\operatorname{tr}(Q)-1)\right)$

FIGURE C.3: 'Huge wave' flow tracking error

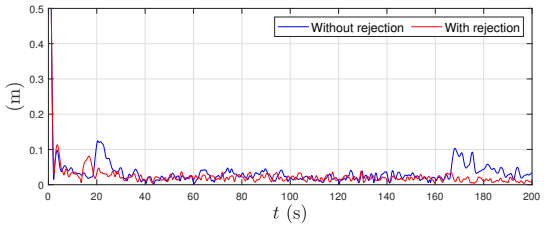

(A) 30%, $\|\widetilde{b}\|$

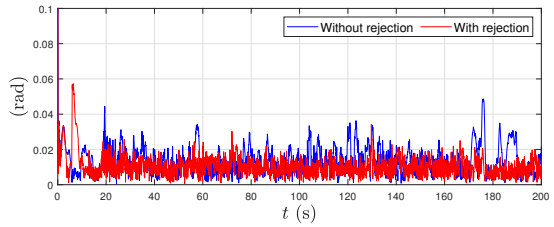

(B) 30%, $\operatorname{acos}\left(\frac{1}{2}(\operatorname{tr}(Q)-1)\right)$

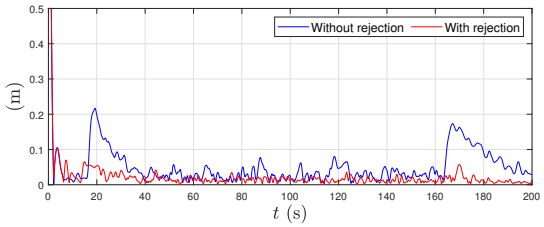

(C) 40%, $\|\widetilde{b}\|$

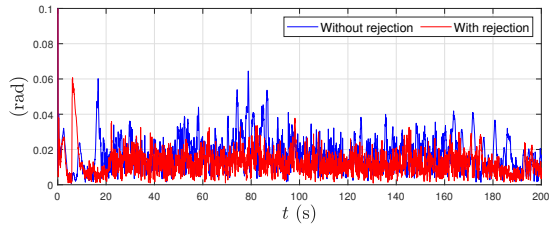

(D) 40%, $\operatorname{acos}\left(\frac{1}{2}(\operatorname{tr}(Q)-1)\right)$

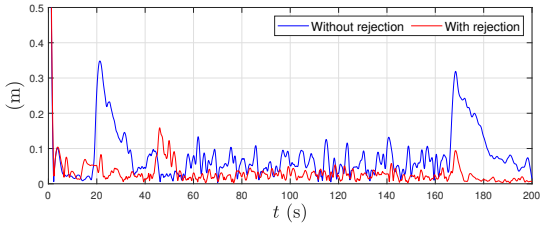

(E) 50%, $\|\widetilde{b}\|$

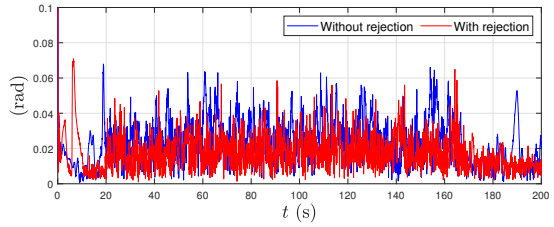

(F) 50%, $\operatorname{acos}\left(\frac{1}{2}(\operatorname{tr}(Q)-1)\right)$

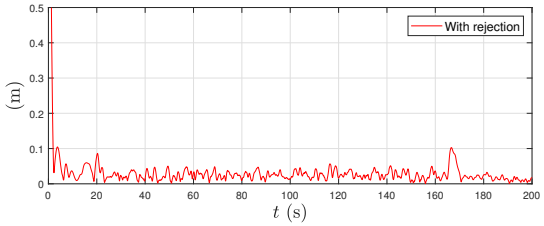

(G) 60%, $\|\widetilde{b}\|$

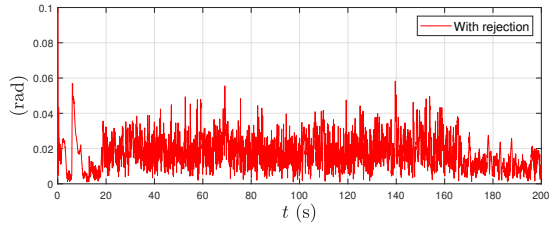

(H) 60%, $\operatorname{acos}\left(\frac{1}{2}(\operatorname{tr}(Q)-1)\right)$

FIGURE C.4: 'Peak' flow tracking error

Bibliography

Bangura, Moses and Robert Mahony (2017). "Thrust control for multirotor aerial vehicles". In: *IEEE Transactions on Robotics* 33.2, pp. 390–405.

Bangura, Moses et al. (2017). "Aerodynamics and control of quadrotors". In.

Basile, Giuseppe and Giovanni Marro (1969). "On the observability of linear, time-invariant systems with unknown inputs". In: *Journal of Optimization theory and applications* 3, pp. 410–415.

Bhale, Pradhyumn, Mrinal Kumar, and Amit K Sanyal (2022). "Finite-time stable disturbance observer for unmanned aerial vehicles". In: *2022 American Control Conference (ACC)*. IEEE, pp. 5010–5015.

Bhat, Sanjay P and Dennis S Bernstein (2000a). "A topological obstruction to continuous global stabilization of rotational motion and the unwinding phenomenon". In: *Systems & control letters* 39.1, pp. 63–70.

— (2000b). "Finite-time stability of continuous autonomous systems". In: *SIAM Journal on Control and optimization* 38.3, pp. 751–766.

Bisheban, Mahdis and Taeyoung Lee (2018). "Geometric Adaptive Control for a Quadrotor UAV with Wind Disturbance Rejection". In: *2018 IEEE Conference on Decision and Control (CDC)*. IEEE, pp. 2816–2821.

— (2020). "Geometric adaptive control with neural networks for a quadrotor in wind fields". In: *IEEE Transactions on Control Systems Technology* 29.4, pp. 1533–1548.

Bohn, Jan and Amit K Sanyal (2016). "Almost global finite-time stabilization of rigid body attitude dynamics using rotation matrices". In: *International Journal of Robust and Nonlinear Control* 26.9, pp. 2008–2022.

Bullo, Francesco and Andrew D Lewis (2019). *Geometric control of mechanical systems: modeling, analysis, and design for simple mechanical control systems*. Vol. 49. Springer.

Chaturvedi, Nalin A, Amit K Sanyal, and N Harris McClamroch (2011). "Rigid-body attitude control". In: *IEEE control systems magazine* 31.3, pp. 30–51.

Chen, Chi-Tsong (1984). *Linear system theory and design*. Saunders college publishing.

Chen, Wen-Hua (2003). "Nonlinear disturbance observer-enhanced dynamic inversion control of missiles". In: *Journal of Guidance, Control, and Dynamics* 26.1, pp. 161–166.

Craig, William, Derrick Yeo, and Derek A Paley (2020). "Geometric Attitude and Position Control of a Quadrotor in Wind". In: *Journal of Guidance, Control, and Dynamics*, pp. 1–14.

Cui, Lei et al. (2021). "Adaptive super-twisting trajectory tracking control for an unmanned aerial vehicle under gust winds". In: *Aerospace Science and Technology* 115, p. 106833.

Dougherty, Christopher J (2022). "On the Experimental Simulation of Atmospheric-Like Disturbances Near the Surface". PhD thesis. California Institute of Technology.

Faessler, Matthias, Antonio Franchi, and Davide Scaramuzza (2017). "Differential flatness of quadrotor dynamics subject to rotor drag for accurate tracking of high-speed trajectories". In: *IEEE Robotics and Automation Letters* 3.2, pp. 620–626.

Furrer, Fadri et al. (2016). "Robot Operating System (ROS): The Complete Reference (Volume 1)". In: ed. by Anis Koubaa. Cham: Springer International Publishing. Chap. RotorS—A Modular Gazebo MAV Simulator Framework, pp. 595–625. ISBN: 978-3-319-26054-9.

DOI: 10.1007/978-3-319-26054-9_23. URL: http://dx.doi.org/10.1007/978-3-319-26054-9_23.

George, William K, Scott H Woodward, and Hussein H Hussein (1989). "An evaluation of the effect of a fluctuating convection velocity on the validity of Taylor's hypothesis". In: *10th Australasian Fluid Mechanics Conference, Volume 2*. Vol. 2, pp. 11–5.

Guo, Bao-Zhu and Zhi-liang Zhao (2011). "On the convergence of an extended state observer for nonlinear systems with uncertainty". In: *Systems & Control Letters* 60.6, pp. 420–430.

Hamrah, Reza (2022). "Discrete-Time Stable Geometric Controller and Observer Designs for Unmanned Vehicles". PhD thesis.

Hamrah, Reza and Amit K Sanyal (2022). "Finite-time stable tracking control for an underactuated system in SE (3) in discrete time". In: *International Journal of Control* 95.4, pp. 1106–1121.

Hanover, Drew et al. (2021). "Performance, precision, and payloads: Adaptive nonlinear mpc for quadrotors". In: *IEEE Robotics and Automation Letters* 7.2, pp. 690–697.

Hardy, Godfrey Harold et al. (1952). *Inequalities*. Cambridge university press.

Hartlieb, Robert Joseph (1956). "The cancellation of random disturbances in automatic control systems". In: *PhDT*.

Horn, Roger A and Charles R Johnson (2012). *Matrix analysis*. Cambridge university press.

Huang, Yi et al. (2001). "Flight control design using extended state observer and non-smooth feedback". In: *Proceedings of the 40th IEEE Conference on Decision and Control (Cat. No. 01CH37228)*. Vol. 1. IEEE, pp. 223–228.

Jeon, Heegyun et al. (2020). "Modeling quadrotor dynamics in a wind field". In: *IEEE/ASME Transactions on Mechatronics* 26.3, pp. 1401–1411.

Jia, Jindou et al. (2022a). "Accurate high-maneuvering trajectory tracking for quadrotors: A drag utilization method". In: *IEEE Robotics and Automation Letters* 7.3, pp. 6966–6973.

Jia, Jindou et al. (2022b). "Agile flight control under multiple disturbances for quadrotor: Algorithms and evaluation". In: *IEEE Transactions on Aerospace and Electronic Systems* 58.4, pp. 3049–3062.

Khalil, Hassan K (2002). *Nonlinear systems third edition*. Vol. 115.

Lee, Taeyoung, Melvin Leok, and N Harris McClamroch (2010). "Geometric tracking control of a quadrotor UAV on SE (3)". In: *49th IEEE conference on decision and control (CDC)*. IEEE, pp. 5420–5425.

Lee, Taeyoung, N Harris McClamroch, and Melvin Leok (2005). "A Lie group variational integrator for the attitude dynamics of a rigid body with applications to the 3D pendulum". In: *Proceedings of 2005 IEEE Conference on Control Applications, 2005. CCA 2005.* IEEE, pp. 962–967.

Levant, Arie (2003). "Higher-order sliding modes, differentiation and output-feedback control". In: *International journal of Control* 76.9-10, pp. 924–941.

Liu, Kang et al. (2022). "Fixed-time disturbance observer-based robust fault-tolerant tracking control for uncertain quadrotor UAV subject to input delay". In: *Nonlinear Dynamics* 107.3, pp. 2363–2390.

Mechali, Omar et al. (2021). "Observer-based fixed-time continuous nonsingular terminal sliding mode control of quadrotor aircraft under uncertainties and disturbances for robust trajectory tracking: Theory and experiment". In: *Control Engineering Practice* 111, p. 104806.

Meier, Lorenz, Dominik Honegger, and Marc Pollefeys (2015). "PX4: A node-based multithreaded open source robotics framework for deeply embedded platforms". In: *2015 IEEE international conference on robotics and automation (ICRA)*. IEEE, pp. 6235–6240.

Moeini, Amir, Alan F Lynch, and Qing Zhao (2021a). "A backstepping disturbance observer control for multirotor UAVs: theory and experiment". In: *International Journal of Control*, pp. 1–15.

— (2021b). "Exponentially Stable Motion Control for Multirotor UAVs with Rotor Drag and Disturbance Compensation". In: *Journal of Intelligent & Robotic Systems* 103.1, pp. 1–17.

Moreno, Jaime A and Marisol Osorio (2012). "Strict Lyapunov functions for the super-twisting algorithm". In: *IEEE transactions on automatic control* 57.4, pp. 1035–1040.

Moreno, Jaime A et al. (2021). "Multivariable super-twisting algorithm for systems with uncertain input matrix and perturbations". In: *IEEE Transactions on Automatic Control* 67.12, pp. 6716–6722.

Nordkvist, Nikolaj and Amit K Sanyal (2010). "A Lie group variational integrator for rigid body motion in SE (3) with applications to underwater vehicle dynamics". In: *49th IEEE conference on decision and control (CDC)*. IEEE, pp. 5414–5419.

Olejnik, Diana A et al. (2022a). "An experimental study of wind resistance and power consumption in mavs with a low-speed multi-fan wind system". In: *2022 International Conference on Robotics and Automation (ICRA)*. IEEE, pp. 2989–2994.

Olejnik, Diana A et al. (2022b). "Flying into the wind: Insects and bio-inspired micro-air-vehicles with a wing-stroke dihedral steer passively into wind-gusts". In: *Frontiers in Robotics and AI* 9, p. 820363.

O'Connell, Michael et al. (2022). "Neural-fly enables rapid learning for agile flight in strong winds". In: *Science Robotics* 7.66, eabm6597.

Percival, Donald B, Andrew T Walden, et al. (1993). *Spectral analysis for physical applications*. cambridge university press.

Pope, Stephen B (2000). *Turbulent flows*. Cambridge university press.

Pounds, Paul, Robert Mahony, and Peter Corke (2010). "Modelling and control of a large quadrotor robot". In: *Control Engineering Practice* 18.7, pp. 691–699.

PX4-Dev, Team (2023a). *Open Source for Drones-PX4 Pro Open Source Autopilot*. URL: https://px4.io/.

— (2023b). *PX4 Gazebo Plugin Suite for MAVLink SITL and HITL*. URL: https://github.com/PX4/PX4-SITL_gazebo-classic.

Rosier, Lionel (1992). "Homogeneous Lyapunov function for homogeneous continuous vector field". In: *Systems & Control Letters* 19.6, pp. 467–473.

Sanyal, AK (2022). "Discrete-time data-driven control with Hölder-continuous real-time learning". In: *International Journal of Control* 95.8, pp. 2175–2187.

Sanyal, Amit and Nalin Chaturvedi (2008). "Almost global robust attitude tracking control of spacecraft in gravity". In: *AIAA guidance, navigation and control conference and exhibit*, p. 6979.

Sanyal, Amit, Nikolaj Nordkvist, and Monique Chyba (2010). "An almost global tracking control scheme for maneuverable autonomous vehicles and its discretization". In: *IEEE Transactions on Automatic control* 56.2, pp. 457–462.

Sanyal, Amit K and Jan Bohn (2015). "Finite-time stabilisation of simple mechanical systems using continuous feedback". In: *International Journal of Control* 88.4, pp. 783–791.

Shao, Xingling et al. (2018a). "Model-assisted extended state observer and dynamic surface control–based trajectory tracking for quadrotors via output-feedback mechanism". In: *International Journal of Robust and Nonlinear Control* 28.6, pp. 2404–2423.

Shao, Xingling et al. (2018b). "Robust dynamic surface trajectory tracking control for a quadrotor UAV via extended state observer". In: *International Journal of Robust and Nonlinear Control* 28.7, pp. 2700–2719.

Stoica, Petre, Randolph L Moses, et al. (2005). *Spectral analysis of signals*. Vol. 452. Pearson Prentice Hall Upper Saddle River, NJ.

Sydney, Nitin, Brendan Smyth, and Derek A Paley (2013). "Dynamic control of autonomous quadrotor flight in an estimated wind field". In: *52nd IEEE Conference on Decision and Control*. IEEE, pp. 3609–3616.

Teng, Sangli et al. (2022). "Input Influence Matrix Design for MIMO Discrete-Time Ultra-Local Model". In: *2022 American Control Conference (ACC)*. IEEE, pp. 2730–2735.

Tennekes, Hendrik and John Leask Lumley (1972). *A first course in turbulence*. MIT press.

Torrente, Guillem et al. (2021). "Data-driven MPC for quadrotors". In: *IEEE Robotics and Automation Letters* 6.2, pp. 3769–3776.

Veismann, Marcel et al. (2021). "Low-density multi-fan wind tunnel design and testing for the Ingenuity Mars Helicopter". In: *Experiments in Fluids* 62.9, p. 193.

Verling, Sebastian et al. (2016). "Full attitude control of a VTOL tailsitter UAV". In: *2016 IEEE international conference on robotics and automation (ICRA)*. IEEE, pp. 3006–3012.

Vidal, Paulo VNM, Eduardo VL Nunes, and Liu Hsu (2016). "Output-feedback multivariable global variable gain super-twisting algorithm". In: *IEEE Transactions on Automatic Control* 62.6, pp. 2999–3005.

Viswanathan, Sasi Prabhakaran, Amit K Sanyal, and Ehsan Samiei (2018). "Integrated guidance and feedback control of underactuated robotics system in SE (3)". In: *Journal of Intelligent & Robotic Systems* 89.1, pp. 251–263.

Wang, Ningshan (2023). *GeometricPX4*. URL: https://github.com/nswang1994/GeometricPX4.

Wang, Sunyi et al. (2022). "Battle the wind: Improving flight stability of a flapping wing micro air vehicle under wind disturbance with onboard thermistor-based airflow sensing". In: *IEEE Robotics and Automation Letters* 7.4, pp. 9605–9612.

Wang, Xuerui et al. (2019). "Quadrotor fault tolerant incremental sliding mode control driven by sliding mode disturbance observers". In: *Aerospace Science and Technology* 87, pp. 417–430.

Watterson, Michael and Vijay Kumar (2019). "Control of quadrotors using the hopf fibration on so (3)". In: *Robotics Research: The 18th International Symposium ISRR*. Springer, pp. 199–215.

Xia, Yuanqing et al. (2010). "Attitude tracking of rigid spacecraft with bounded disturbances". In: *IEEE Transactions on Industrial Electronics* 58.2, pp. 647–659.

Yu, Jinpeng, Peng Shi, and Lin Zhao (2018). "Finite-time command filtered backstepping control for a class of nonlinear systems". In: *Automatica* 92, pp. 173–180.

Yu, Shuanghe et al. (2005). "Continuous finite-time control for robotic manipulators with terminal sliding mode". In: *Automatica* 41.11, pp. 1957–1964.

Zhang, Xiaocheng, Wenchao Xue, and Hai-Tao Fang (2021). "On extended state based Kalman filter for nonlinear time-varying uncertain systems with measurement bias". In: *Control Theory and Technology* 19, pp. 142–152.

Zhang, Xiaocheng et al. (2020). "Extended state based Kalman filter for uncertain systems with bias". In: *IFAC-PapersOnLine* 53.2, pp. 2299–2304.

Zhu, Zheng, Yuanqing Xia, and Mengyin Fu (2011). "Attitude stabilization of rigid spacecraft with finite-time convergence". In: *International Journal of Robust and Nonlinear Control* 21.6, pp. 686–702.

VITA

Ningshan Wang is a doctor of philosophy candidate in the Department of Mechanical and Aerospace Engineering at Syracuse University. He received his bachelor of science degree in thermal and power engineering from Shanghai Jiao Tong University, and got his master of science in mechanical and aerospace engineering from Syracuse University in 2019. His research focuses on developing theories on robust geometric controllers and observers for autonomous unmanned systems. During PhD, he has been conducting research on robust control and estimation problems for unmanned aerial vehicle within challenging environment.